A SEARCH FOR EXOTIC PARTICLES

IN THE HIRES DATA SET

by

Samuel Adam Blake

A dissertation submitted to the faculty of
The University of Utah
in partial fulfillment of the requirements for the degree of

Doctor of Philosophy

Department of Physics

The University of Utah

December 2009

THE UNIVERSITY OF UTAH GRADUATE SCHOOL

SUPERVISORY COMMITTEE APPROVAL

of a dissertation submitted by

Samuel Adam Blake

This dissertation has been read by each member of the following supervisory committee and by majority vote has been found to be satisfactory.

_____	_____
	Chair: Charles Jui
_____	_____
	Carleton DeTar
_____	_____
	Cynthia Furse
_____	_____
	Stephan LeBohec
_____	_____
	Brian Saam
_____	_____
	Wayne Springer

THE UNIVERSITY OF UTAH GRADUATE SCHOOL

FINAL READING APPROVAL

To the Graduate Council of the University of Utah:

I have read the dissertation of Samuel Adam Blake in its final form and have found that (1) its format, citations, and bibliographic style are consistent and acceptable; (2) its illustrative materials including figures, tables, and charts are in place; and (3) the final manuscript is satisfactory to the supervisory committee and is ready for submission to The Graduate School.

_____ _____

Date

Charles Jui
Chair: Supervisory Committee

Approved for the Major Department

_____

David Kieda
Chair/Dean

Approved for the Graduate Council

_____

Charles A. Wight
Dean of The Graduate School

THE UNIVERSITY OF UTAH GRADUATE SCHOOL

ABSTRACT

The HiRes detector performed stereoscopic observations of Ultra High Energy Cosmic Rays (UHECRs) from 1999 to 2006, recording a data set with stereo aperture of UHECRs with energies down to ~10^{18} eV. The coincident observation from two sites allows for geometrical reconstruction without the use of any timing information. This feature permits the direct measurement of shower propagation speed. Using this measurement of shower speed, the HiRes data were examined for events whose speed either exceeded the speed of light or were significantly lower than the speed of light. No candidate anomalous events were found. Upper limits for the flux of such events were estimated based on this result.

TABLE OF CONTENTS

LIST OF TABLES

ACKNOWLEDGEMENTS

The author would like to give special thanks to Dr. Charles Jui, Doug Rodriguez, John Matthews, and the other members of the HiRes collaboration. This work would not have been possible without their aid. The author would also like to thank his wife, Jennifer Blake, whose support was invaluable during the years spent gathering and analyzing the data for this work.

This work is supported by US NSF grants PHY-9321949, PHY-9322298, PHY-9904048, PHY-9974537,PHY-0098826, PHY-0140688, PHY-0245428, PHY-0305516, PHY-0307098, and by the DOE grant FG0392ER40732. We gratefully acknowledge the contributions from the technical staffs of our home institutions. The cooperation of Colonels E. Fisher, G. Harter, and G. Olsen, the US Army, and the Dugway Proving Ground staff is greatly appreciated.

CHAPTER I

ULTRA HIGH ENERGY COSMIC RAYS

Cosmic rays are energetic particles that strike the Earth from outside its atmosphere. Cosmic rays were first observed in 1912 by Victor Hess, who was conducting balloon experiments measuring radiation in the atmosphere. At this time, it was thought that this radiation was the result of radioactive components decaying in the Earth's crust. If that were the case, the radiation levels should have decreased as the balloons moved higher in the atmosphere. Hess was able to show that the specific type of radiation he was measuring increased with altitude. The increasing radiation levels indicated that the balloons were getting closer to the source. This meant that surprisingly, the source was outside of the Earth's atmosphere.

Due to its extraterrestrial origin, the radiation Hess measured was called cosmic rays. It was later discovered that the radiation was the result of energetic particles interacting with the atmosphere, and not actually rays of radiation as initially thought. However, by this time, the name "cosmic rays" was well established and these particles continue to carry this name. Cosmic rays range in type from electrons to heavy nuclei. Since Vector Hess's discovery, various experiments have sought to analyze the source, energy spectrum, and composition of cosmic rays.

Importance to Physics

Several interesting questions were raised by the discovery of particles from outside the Earth's atmosphere. Three of the primary questions are where are the particles coming from, what are they made of, and what are the underlying physics governing their behavior? Attempts to answer these questions have led to numerous discoveries, especially in the field of particle physics.

In the early years of studying cosmic rays, the particles measured had energies orders of magnitude higher than could be produced in available accelerators. When energetic particle collisions occur, the energy released allows for the production of particles not normally stable enough to be observed in nature. Given the high energy of cosmic rays, cosmic rays were the perfect subjects for new particle searches.

A large number of more exotic hadrons and mesons were discovered this way. In 1932, the positron was discovered in a cloud chamber by Carl Anderson [1]. In 1937, the muon was seen in cloud chambers [2].

A flurry of discoveries from cosmic rays in the 1940s and 1950s helped further the understanding of particle physics. Among those particles discovered were the Σ, the Kaon, and the pion. The Kaon was particularly important, as it played a role in demonstrating CP violation. Other particles were seen in studies, including the Ξ, and the Ω^- [3]. Most of these particles were observed using direct measurement in cloud chambers. At around the same time, ground based accelerators were built that could reach energies high enough to do much of the same research. The controlled environments provided by accelerators allowed for much more detailed studies of particle interactions. Ground based accelerators thus became the primary experiments for studying particle interactions and cosmic ray and particle physics research diverged.

Work done on cosmic rays by Pierre Auger had already demonstrated that particles with energies upwards of 10^{15} eV could exist [4]. Cosmic ray physics refocused on measurements of the energy spectrum and attempts to determine the composition of very high energy cosmic rays. The measurement of the Cosmic Microwave Background in the early 1960s led to a theoretical prediction of an end to the cosmic ray spectrum called the Greisen Zatsepin Kuzmin (GZK) cutoff in honor of the authors of the original theoretical work that predicted it [5, 6]. The measurement of the break in the spectrum became the goal of multiple experiments.

In the early 1990s, the Fly's Eye experiment at the University of Utah reported seeing a cosmic ray with energy of $3x10^{20}$ eV [7]. This particle and others reported by the AGASA collaboration caused a great deal of excitement in the physics community. The energy of these particles was well above the expected cutoff for cosmic rays. This indicated there may be some unknown physical process at work at very high energies.

However, the extremely low statistics available at higher energies made it impossible to confirm or exclude an excess above the GZK limit. One of the principle reasons the HiRes experiment was built was to probe the energy region around the GZK limit and provide evidence for or against the GZK cutoff.

Measurement Techniques

Cosmic rays can be measured in various ways. Early experiments relied on measuring the radiation cosmic rays produce as they moved through the atmosphere. Subsequent experiments have developed into two main categories. The first category is direct detection. Experiments using direct detection are designed to detect and measure the particle itself examples of which include ground-based experiments like cloud

chambers, satellite-born experiments like Advanced Thin Ionization Calorimeter (ATIC), and balloon-born experiments like the Alpha Magnetic Spectrometer (AMS).

The cloud chamber is an excellent example of the basic method direct detection experiments employ. A cloud chamber is a closed environment containing water or alcohol vapor. The chamber is cooled, allowing for the vapor to become supersaturated. Cosmic rays interact with the cloud, forming ions. The ions cause the vapor around them to condense, making the path of the cosmic ray through the chamber visible. These tracks are then photographed and analyzed.

While methods of direct detection have become more advanced, the basic principle remains the same. The particle itself strikes the detector where it can be measured and can interact in a manner that causes it to fragment. Various sensors at different lengths from the point of impact measure the path and energy of secondary particles. This data can then be analyzed to provide information about the original particle.

As energy increases, the flux of particles decreases. In order to capture a sufficient number of particles for statistical analysis, the size of the detector must increase. Standard methods of direct detection become impractical to construct for the ultra-high energy regime.

The conventional technique at energies above ~10^{15} eV has been to observe extensive air showers (EAS) created by primary cosmic ray particles (primaries) colliding with nuclei in the upper atmosphere. This phenomenon was first observed by Pierre Auger in 1939 when he noticed coincidence in the arrival time of cosmic ray particles at ground level over large ("extensive") areas [4]. This technique essentially uses the

atmosphere itself as an interaction medium of a sampling calorimeter and allows for the construction of relatively inexpensive detectors that may cover hundreds of square kilometers.

In an EAS, the primary particle strikes a nucleus in the upper atmosphere and interacts, forming smaller particles. Both the projectile cosmic ray and the target nucleus break up and produce ~100 secondary hadrons. About two thirds of the secondary hadrons are pions, which are the lightest meson. Due to isospin invariance, exactly 1/3 of the pions are neutral π^0. The charged π^- and π^+ can only decay weakly, and thus have long lifetimes that lead most of them to collide with additional nuclei before decaying, as do most of the other remaining secondary hadrons. The neutral pions, on the other hand, decay electromagnetically, primarily into two gamma rays, as shown in Equation 1.

$$\pi^0 \rightarrow \gamma + \gamma \tag{1}$$

The gammas in turn produce an e^+e^- pair when colliding with an atom (or Compton scattering an electron). The e^- or e^+ in turn can create additional photons through Bremsstrahlung radiation (or in the case of the e^+annihilate with the e^-).

The extensive air shower that develops from the subsequent interactions represents the overlap of a hadronic shower with that of an electromagnetic shower where the hadronic interactions continue to transfer energy into the electromagnetic shower. By the time the shower enters the troposphere, it is primarily an electromagnetic shower consisting of electrons, positrons, and photons. This process divides the energy of the primary cosmic ray particle into more and more shower particles. The shower continues

to grow until the average energy of each particle is no longer sufficient to produce additional particles and they begin to range out. The energy at which this transition occurs is known as the critical energy. Correspondingly, the shower reaches a maximum size and begins to decay beyond this point. This point is called the shower maximum.

The traditional technique for detecting air showers pioneered by Auger is to lay out a grid of particle detectors (e.g., scintillation counters or water Cerenkov detectors) that sample the particle density laterally. The trigger for detectors is the coincident arrival of particles over a group of contiguous detectors. The shower particles arrive approximately in a spherical front, and the relative timing between hit counters can be used to determine arrival direction of the primary to an accuracy of several degrees. The energy of the primary particle can be inferred from the sampled densities.

A measure of the mass number A of the primary nucleus is also possible by the inclusion of muon counters (either underground scintillators or discrimination between e and μ built into a water Cerenkov tank). Primary nuclei of a higher A tend to begin showing higher in the atmosphere than a lighter ones because of their larger size and tend to higher multiplicities of pions. Having more pions higher in the atmosphere increases the likelihood that a π^- or π^+ will decay, primarily into a $\mu + \nu_\mu$ pair. The resulting hard muons tend to survive to the ground. Thus, heavier primaries tend to give higher muon numbers. However, both the muon content and the particle energy scale for ground arrays are heavily dependent on our understanding and modeling of the hadronic process.

An alternative method for measuring air showers was pioneered by Ken Greisen of Cornell University in the late 1960s and was successfully implemented for studying cosmic rays by a group at the University of Utah in the late 1970s. The “fluorescence”

technique images the UV scintillation light produced by the charged particles (essentially just the electromagnetic shower) passing through the atmosphere. The arrival direction and trajectory of the core of the shower can be determined from either the shower images from two detectors separated in space, or from the image and the arrival time of the light signal at a single detector. The energy measurement is derived from the total amount of light produced, which is inferred without any reliance on hadronic interaction models. The mass A of the primaries can be measured from the direct measurements of the depth of the shower maximum, which has less hadronic model dependence than the muon density.

The HiRes experiment consisted of a pair of fluorescence detectors separated by 12.6 km and will be discussed in greater detail in Chapter II. In the following subsections, we will survey the major physics topics related to the ultra high energy cosmic rays (UHECR). UHECRs refer to cosmic rays with energies greater than $\sim 10^{18}$ eV. The major physics topics include spectrum, composition, and anisotropy.

Energy Spectrum

The differential flux (number of particles / unit area / unit solid angle / unit time / energy interval) of cosmic rays as a function of their energy is called the energy spectrum. The spectrum provides important clues as to the origin and physical processes behind the acceleration or production of cosmic rays. Measuring the spectrum has been one of the main goals of UHECR experiments. Figure 1 shows a compilation of

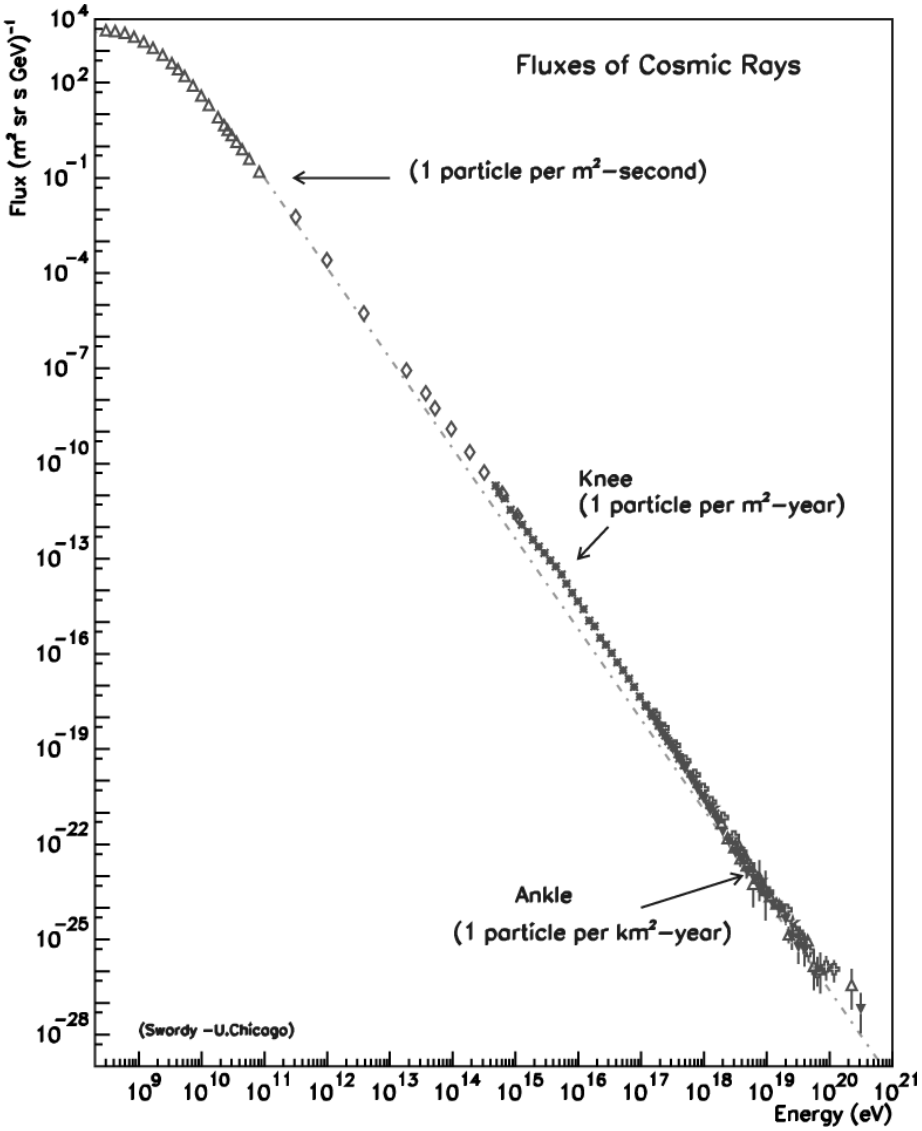

Figure 1: Cosmic Ray Spectrum from 10^8 eV to 10^{21} eV

measurements of the energy spectrum from 10^8 eV to 10^{21} eV in units of $(m^2\ sr\ s\ GeV)^{-1}$ [8]. Rather amazingly, over its entire 11 decade range, the spectrum closely follows a power law $E^{-\alpha}$ where α is approximately 3. When observed in greater detail, however, the spectral index α changes at several energies. The first among these changes is the "knee" at approximately 10^{15} eV where α increases from ~2.8 to 3.0. The next is the "ankle" at ~$5x10^{17}$ eV where α increases further to approximately 3.3. Such changes are notable as they may indicate a change in the source and composition of cosmic rays.

The source of these cosmic rays still remains a mystery. Several source models have been proposed, and can generally be classified in two categories: "Bottom Up" and "Top Down."

"Bottom Up" models start with lower energy primaries that are accelerated through physical interactions to reach their final measured energy. Examples of possible sources for "Bottom Up" cosmic ray accelerators include AGN, super novae, and pulsars. The exact physical processes needed to accelerate cosmic rays to high energies while still producing a power law spectrum are still unknown. There are, however, some promising models. One such model is Fermi Acceleration.

In the original model proposed by Fermi in 1949, particles were accelerated by colliding with interstellar clouds. The particles are "reflected" from theoretical "magnetic mirrors" in the clouds to gain energy. A condensed example following the derivation by Longair follows. A much more detailed explanation can be found in his book [9]. The basic calculation for the energy gained by a charged particle in one interaction can be repeated by considering a particle incident to one of these magnetic

mirrors at a given angle. This situation is visualized in Figure 2. In Figure 2(a), a particle of mass m is reflected from a surface of mass M.

Given that M >> m so that the cloud can be considered infinitely massive and the cloud is moving at velocity $\vec{V}$, the energy of the particle in the center of the momentum frame can be given by Equation 2.

$$E' = \left(1 - \frac{\left|\vec{V}\right|^2}{c^2}\right)^{-1/2} \left(E + \left|\vec{V}\right| p\cos\theta\right) = \gamma_v \left(E + \left|\vec{V}\right| p\cos\theta\right) \tag{2}$$

In the collision in this frame, the particles total energy must be conserved, but the momentum in the x direction is reversed. This allows for the energy of the particle in the observer's frame to be written as shown in Equation 3.

$$E'' = \gamma_v (E' + \left|\vec{V}\right| p_x') = \gamma_v (E' + \left|\vec{V}\right| \gamma_v \left(p\cos\theta + \frac{VE}{c^2}\right)) \tag{3}$$

Combining Equations 2 and 3 and using $p_x / E = v\cos\theta / c^2$ results in Equation 4.

$$E'' = \gamma_v{}^2 E \left[1 + \frac{2Vv\cos\theta}{c^2} + \left(\frac{V}{c}\right)^2\right] \tag{4}$$

This equation can be solved for $E'' - E$ by expanding to second order in terms of V/c. This gives Equation 5.

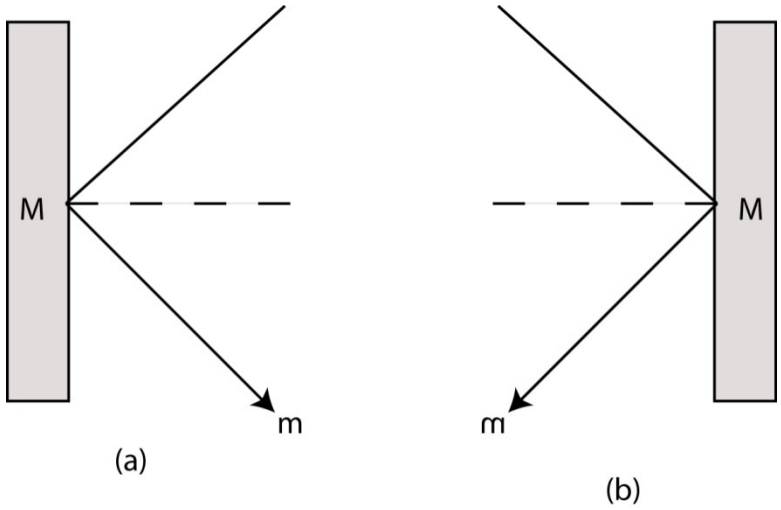

Figure 2: Illustration for second order Fermi Acceleration. Represents the collision of a particle of mass m with a cloud of mass M. (a) head-on collision. (b) a following collision

$$E'' - E = \Delta E = \frac{2Vv\cos\theta}{c^2} + 2\left(\frac{V}{c}\right)^2 \tag{5}$$

This expression gives the change in energy for the particle before and after the collision in the observer's frame. To find the average change in energy for a number of particles, the next step is to average over all allowed angles. This derivation is best left for other more detailed texts [9], but recognizing that head on collisions (Figure 2(a)) are slightly more probable than following collisions (Figure 2(b)), the average energy gain per collision can be calculated as shown in Equation 6.

$$\left\langle \frac{\Delta E}{E} \right\rangle = \frac{8}{3}\left(\frac{V}{c}\right)^2 \tag{6}$$

This result shows that the increase in energy is second order in V/c. Accordingly, this type of Fermi acceleration is referred to as second order Fermi acceleration. Using the diffusion loss equation, a result for the spectrum produced can be found. As the same fractional increase is gained with every collision, this will result in a power law spectrum.

This method is not without problems. For instance, random velocities of interstellar clouds tend to be small. The effect of energy loss is not considered, and there is no physics in the theory to say why the resulting energy spectrum should have an exponent of ~3.

Work done on this subject led to a simpler version of Fermi acceleration. If the average energy after one collision is given by $E = \beta E_0$ (note – first order in V/c) and the probability the particle stays in the cloud is given by P, then the fractional number of

particles left in the cloud is given by Equation 7.

$$\frac{N}{N_0} = \left(\frac{E}{E_0} \right)^{\ln P / \ln \beta} \tag{7}$$

Taking the derivative of Equation 7 with respect to E also results in a power law for the spectrum. A good deal of work has been done with this first order Fermi acceleration. In particular, Bell showed that assuming certain physical constraints resulted in a power law spectrum with an index of 2 [10]. While this spectral index does not match that observed experimentally, the ability to produce a power law spectrum from basic physical principles makes first order Fermi acceleration a promising candidate.

In "Top Down" models, particles are created at large energies via exotic physical phenomena. Examples of possible classes for "Top Down" cosmic rays include strangelets, quantum strings, topological defects, superstring decay, and relic monopoles. The theoretical background for decay or interaction of these particles is largely speculative. Chapter III discusses some aspects of the theoretical background on strangelets and their possible contribution to cosmic rays.

GZK Effect

In 1966, Greisen, Zatsepin, and Kuzmin calculated that the spectrum should end in a sharp cutoff due to the interaction of cosmic ray primaries with the cosmic microwave background discovered in the previous year [5, 6]. This reaction is shown in Equation 8.

$$p + \gamma_{cmb} \rightarrow \Delta \rightarrow n(p) + \pi^{+}(\pi^{0}) \quad (8)$$

Here, the photon comes from the cosmic microwave background. Above the Δ threshold (known as the GZK threshold in honor of the authors) of about $E_p \sim 6 \times 10^{19}$eV, the ranges of cosmic protons become limited to about 30-50 Mpc from the Earth. This constitutes less than 1% of the visible Universe and thus ~ 100 fold suppression in the cosmic ray flux is expected above the GZK threshold.

Figure 3 shows the results of the HiRes spectrum analysis [11]. HiRes observed a break consistent with the GZK cutoff at an energy of $(5.6 \pm 0.5 \pm 0.9) \times 10^{19}$ eV. The significance of the spectral break was calculated at 5 standard deviations.

Composition

Any particle or nucleon that strikes the Earth from outside our atmosphere is classified as a cosmic ray (extra-terrestrial gammas are by convention usually not included in this category). Because of this broad definition, much effort has been put into determining the actual composition of incoming particles. Knowledge of the composition of cosmic rays can help with understanding both the physical environments in which they were created, the physical processes of their creation, and the environments they interacted with while propagating through interstellar space.

Different measurement techniques can be used to determine composition with varying degrees of accuracy. At lower energies where direct measurement is possible, the composition of cosmic rays can be determined accurately through direct observation of the particle's physical attributes. At low energies, cosmic rays come primarily from within the galaxy and shed light on the contents of the galaxy itself. At sufficiently low

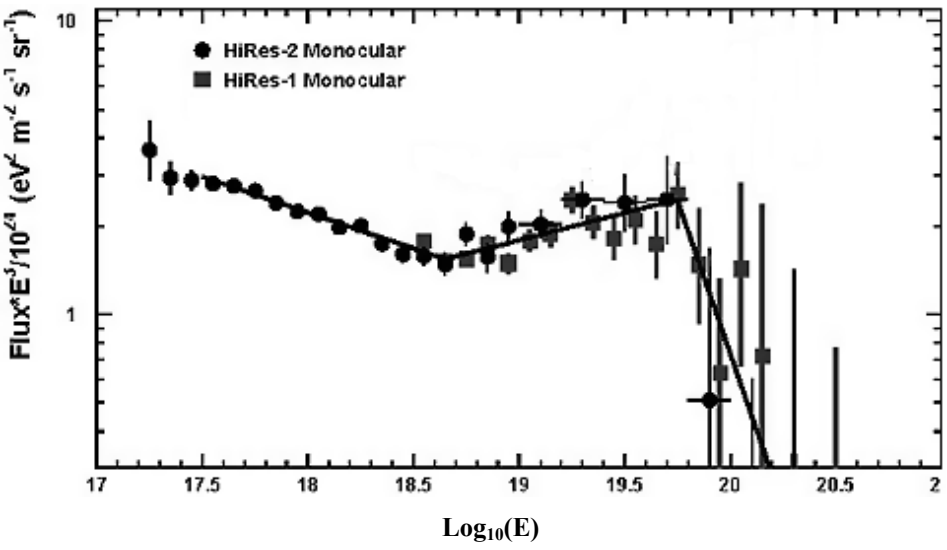

Figure 3: HiRes spectrum measurement.

energies, charged cosmic rays are bent enough by the galactic magnetic field that they cannot escape, so measurements of the composition at low energies mirrors galactic composition. Measurements done in low energy ranges have determined that around 89% of all galactic cosmic ray primaries are protons. Around 10% are helium, and 1% of galactic cosmic rays are heavier elements.

As discussed earlier, at high energies individual particles are not measured directly. Therefore, composition must be inferred from shower properties. These properties are based on hadronic models of how the shower develops in the atmosphere. This means that exact composition can only be as accurate as the hadronic interaction models used to describe particle behavior in showers.

For fluorescence detectors where both the size and longitudinal profile of the EAS can be measured directly, the depth of the shower maximum (X_{max}) can be determined directly without the use of hadronic interaction models. X_{max} is expected to be deeper (larger in value) for lighter nuclei than for heavier ones. However, for any given mass A, X_{max} also increases logarithmically with energy. Simulations have shown that while the absolute values of X_{max} for a given species in an energy range can be somewhat model-dependant, the shape of the logarithmic increase known as the elongation rate (shown in Equation 9) appears to be independent of the composition.

$$ER = \frac{d(X_{max})}{d(\log E)} \tag{9}$$

Furthermore, the separation between the X_{max} of protons and that of iron (the most abundant of cosmic ray nuclei at larger values of A and lower energies) appears to be about 75 g/cm^2. This also appears only weakly model-dependant.

Figure 4 shows the result of the compilation of $< X_{max} >$ vs. $\log E$ data from the HiRes-Mia hybrid observations and those of the HiRes Stereo experiments [12] along with model predictions. The HiRes results at E>10^{18} eV shows an elongation rate consistent with a fixed composition and values that suggest mostly lighter nuclei (i.e., protons). The data between 10^{17} eV and $10^{18.5}$ eV shows an elongation rate larger than that expected for fixed composition and is consistent with a transition from a primarily heavy (iron) composition at 10^{17} eV to that of a light composition at 10^{18} eV. For reference, Figure 4 includes the stereo Fly's Eye composition measurements.

It should be noted that these results draw somewhat different conclusions than those of the stereo Fly's Eye experiment, where the heavy-light transition was seen to occur over the 10^{18}-10^{19} eV range. However, it should also be noted that the HiRes/Mia have significantly better pixel resolution: one degree vs. 5 degree pixels. Consequently, the HiRes/Mia results have an X_{max} resolution of ~25g/cm^2 vs. the ~55g/cm^2 of the stereo Fly's Eye results. HiRes and HiRes/Mia also had significantly better control over systematics than did Fly's Eye.

Anisotropy

Anisotropy refers to the nonuniformity in the arrival direction of cosmic rays. One of the principal goals of Cosmic Ray research has been to determine the source of ultra high energy cosmic rays. At first glance, the most straightforward approach would be to measure the arrival direction and scan the sky for possible sources in that direction.

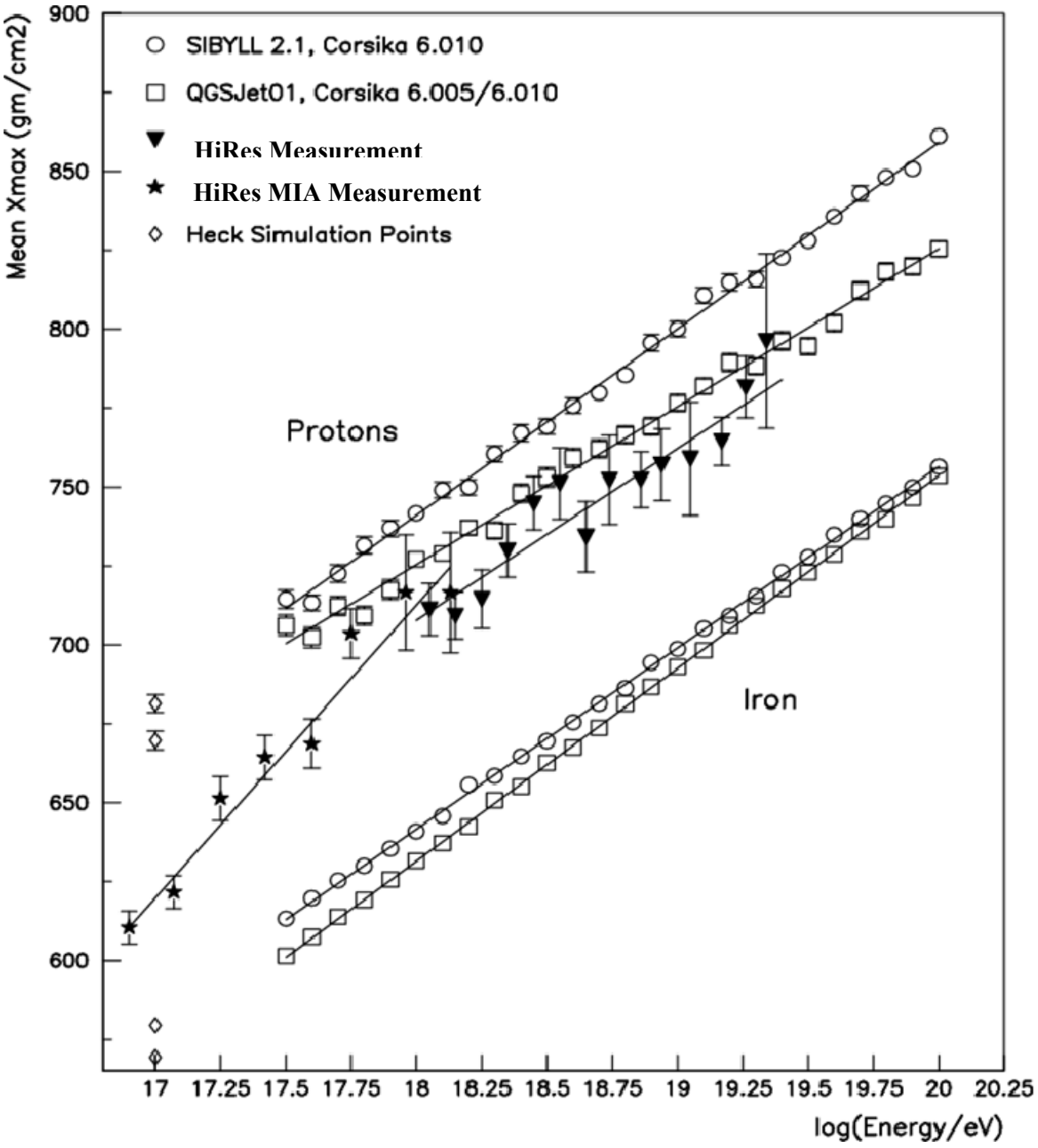

Figure 4: HiRes composition

However, cosmic rays are primarily charged particles and are subject to deflection by magnetic fields.

In the presence of a uniform magnetic field, cosmic rays are deflected in circular paths. The formula to calculate this deflection, known as the Larmor radius, is given in Equation 10.

$$\boldsymbol{r = \frac{mv_{\perp}}{qB}} \tag{10}$$

The exact magnetic field present in the Galaxy is not well known. However, recent studies have estimated the magnetic field at strengths at around 1-2 μG [13]. Using fields of these strengths, the calculated Larmor radius is such that particles with energies less than ~10^{15} eV are unable to escape the galaxy. These particles scatter until they eventually encounter an object like the Earth. This means that the arrival direction of the particle will not generally correspond with the direction to the source.

As energies increase, the Larmor radius gets larger. At the highest energies, the radius is large enough that it may be possible to see sources by tracing the path of particles backwards through the magnetic fields they encounter. As small scale effects of galactic and extra galactic magnetic fields are not well known, a more general approach is to search for clustering among high energy events.

This type of search has been carried out with the HiRes data. The exact details or these searches are not included here. However, no point sources have been detected in the HiRes data set.

CHAPTER II

DETECTORS

The HiRes detector consisted of two sites located at Dugway Proving Grounds in Tooele County, Utah. These sites were referred to as HiRes 1 and HiRes 2. During the early part of its operational life, HiRes was the only fluorescence detector in the world and collected the largest data set to date of UHECRs at energies greater than $10^{17.5}$ eV. The two sites differed in both read-out and sky coverage so will be discussed separately.

HiRes 1

HiRes 1 started construction in 1993 on Little Granite Mountain. Fourteen prototype telescopes were constructed and operated between 1994 and 1997. In 1997, four telescopes were added and the prototype telescopes were reconfigured into a working detector. Four additional telescopes were first operated at the HiRes 2 site, and then moved to HiRes 1 as HiRes 2 neared completion. This brought the total number of telescopes at the HiRes 1 site to 22. The HiRes 1 detector operated from 1997 to 2006.

Each telescope consisted of a spherical mirror that focused UV light generated by air showers onto a planar cluster of phototubes. Each cluster was controlled by electronics linked to a central timing rack and a central computer. The central timing rack housed a GPS clock and necessary electronics to record events that spanned several

telescopes. The central computer took care of operation and data storage for the telescopes.

The telescope mirrors themselves were constructed using 4 spherical segments. Each mirror had an unobstructed viewing area of 3.72 m^2. They were aligned to focus light on a plane 232.41 cm from the center of the mirrors where the camera for each mirror is located.

The camera for each mirror consisted of 256 photomultiplier tubes (PMTs) housed in a protective box. A UV band-pass filter covered all of the PMTs to reduce background noise. This filter allowed light ranging from 300nm to 400nm through to the PMTs. The PMTs were arranged in a 16x16 hexagonally close packed grid. Each phototube viewed a one degree cone of sky. As a result of the hexagonal close packing, the cluster as a whole viewed approximately 14 degrees in elevation and 16 degrees in azimuth. At HiRes 1, the telescopes looked at the sky from approximately 3 to 17 degrees in elevation. The individual telescopes were arranged to give almost a full 360 degree azimuthal coverage.

Figure 5 shows an event recorded by the HiRes 1 site. The small gap in azimuthal coverage can be seen between mirrors 2 and 17. In Figure 5, each phototube is represented as a hexagonal box. The phototubes are arranged as they would view the sky, with the center of the sky (directly overhead) located in the center of the figure. The mirror number is listed next to each mirror, showing how they were arranged to view the sky. North is located at the top of the figure. An event is represented by colored phototubes. Each phototube is colored according to the magnitude of signal it reports. In

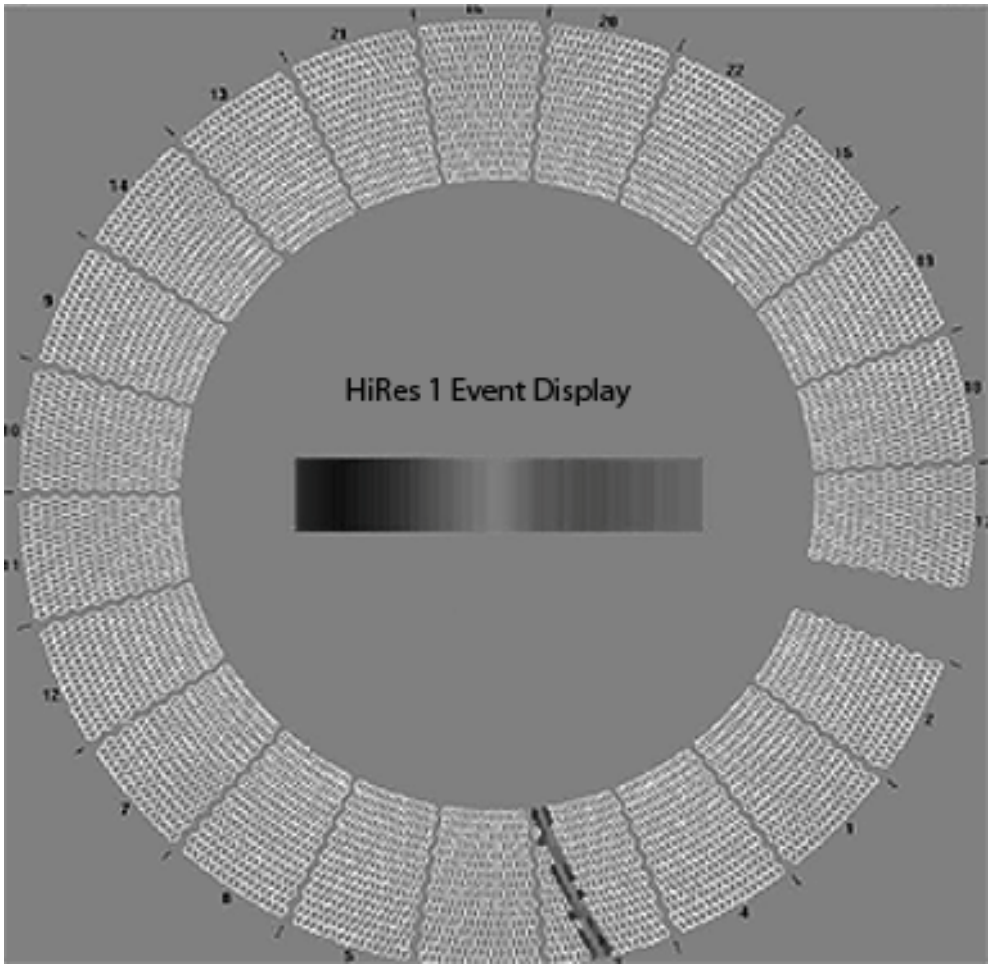

Figure 5: Camera arrangement for HiRes 1. The center corresponds to the Zenith angle. The outer perimeter is 3° above the horizon and the inner perimeter is 17° above the horizon. Up is North, and Right is East.

this case, the event is shown in telescope 3 moving from the top to the bottom of the telescope.

The HiRes 1 site used a "sample and hold" read-out. Electronics watched for candidate events using a set of "triggers." For HiRes 1, the 256 PMTs for each mirror were divided into 16 subclusters each containing 16 PMTs. A trigger for an individual subcluster was defined as a signal in 3 PMTs with at least 2 of them being adjacent. A trigger for a mirror was defined as 2 adjacent subclusters triggering unless a neighboring mirror had triggered – in which case only 1 subcluster was required.

When a candidate event triggered the detector, the total integrated signal over a period of 4.5 μs from each of the hit PMTs was digitized. This information along with variables describing the state of the electronics at the time of the trigger was then sent to the central computer to be stored. A time stamp was stored with each tube corresponding to the time of the trigger. This set of information made up the "raw" data from the detector. The raw data were then transferred via network to the University of Utah for further processing.

The telescopes were arranged in a series of buildings around the top of Little Granite Mountain. Two telescopes were located in each building. A coordinate system was defined with the center being a known point near the central facility on Little Granite Mountain. From here, the exact location of each mirror was measured. The exact pointing direction of each tube in the sky was also measured. These measurements defined the geometry of the HiRes 1 site.

HiRes 2

HiRes 2 was located 12.6 km southwest of the HiRes 1 site on Camel's Back Ridge. The development and construction of the HiRes 2 electronics took place between 1995 and 1999. The site itself became fully operational in 1999. The site consisted of 42 telescopes arranged in two rings. The first ring viewed the sky from approximately 3-17 degrees. The second ring viewed the sky from approximately 17-31 degrees. The HiRes 2 detector operated from 1999 to 2006.

The optical components of HiRes 2 were essentially identical to those described above for HiRes 1. Once again, each had 16 degrees azimuthal coverage and 14 degrees elevational coverage. Figure 6 shows an event as recorded by HiRes 2. A small gap in coverage can be seen between mirrors 24 and 26 of the first ring. The same gap exists between mirrors 28 and 23 of the second ring. This gap in coverage was intentionally located such that it pointed directly at the two peaks of Camel's Back Mountain. These peaks would have obstructed viewing for any mirrors placed in the gap.

Each mirror in HiRes 2 was connected to its nearest neighbors via two fiber optic cables to transmit information. This resulted in a dual "ring" configuration for network information sent and received from each mirror. One of the two rings was used to transfer data back to the central facility, and the ring structure naturally merged the data streams from the individual telescopes.

The second ring was used to transmit commands to the telescopes and to relay "nearest" neighbor trigger information, which reduced the trigger requirement in the case a neighboring (in terms of sky coverage) telescope satisfied the full trigger condition.

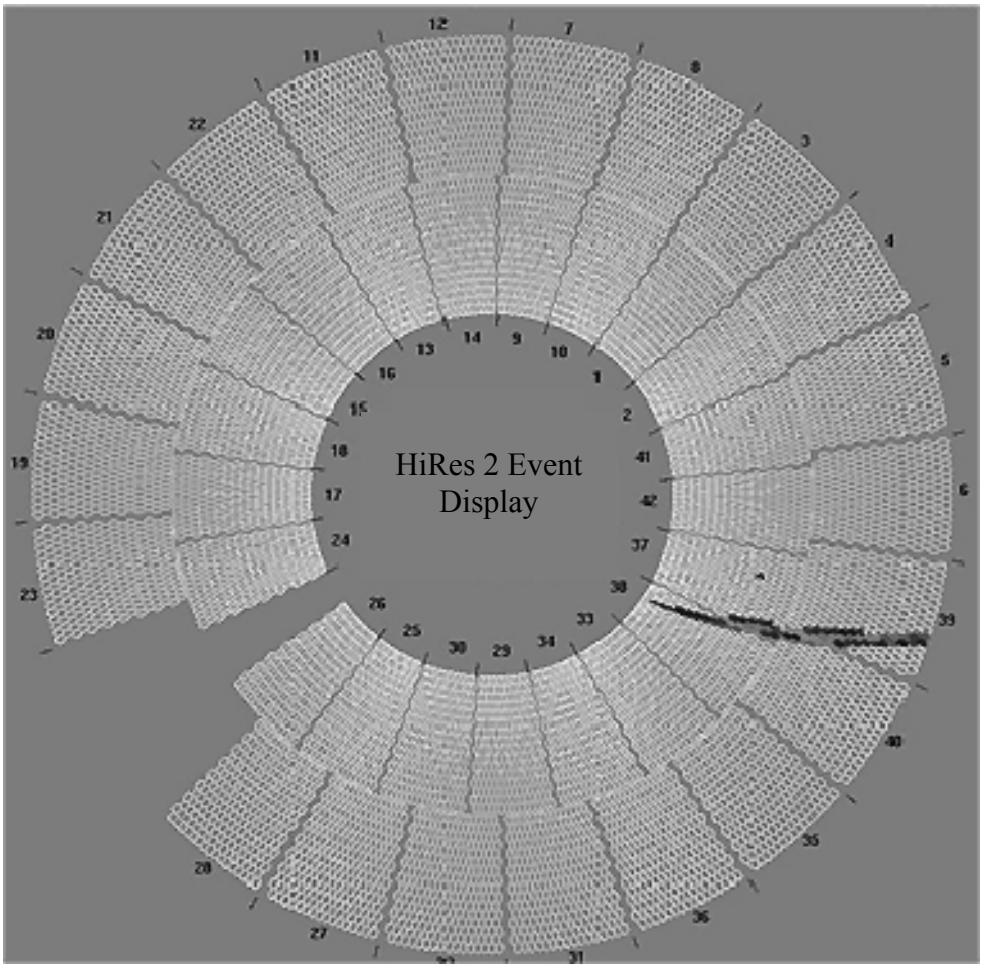

Figure 6: Mirror arrangement for HiRes 2. The center corresponds to the Zenith angle. The outer perimeter is 3° above the horizon and the inner perimeter is 31° above the horizon. Up is North, and Right is East.

The major difference between HiRes 1 and HiRes 2 was in the electronics used. HiRes 2 used Flash ADC electronics instead of the sample and hold electronics of HiRes 1. Flash ADC electronics use a linear voltage ladder with comparators to compare an incoming voltage to preset references, allowing for the analog signal to be digitized in one pass. Instead of integrating over the entire signal, the signal from the phototubes is digitized and recorded in a series of 100ns time bins. This digitized wave form could then be analyzed, from which a pulse and integral signal could be obtained. The peak of the pulse was reported as trigger time, while the integral signal was converted to number of photoelectrons.

As with HiRes 1, the telescopes were arranged in a series of buildings located around the edge of Camel's Back Ridge. Two telescopes were stored per building. The exact location of each mirror was then measured relative to a central point on Little Granite Mountain. The exact pointing direction of each tube was also determined. These measurements make up the geometry of HiRes 2.

Calibration and Atmospheric Monitoring

Several different systems were used to calibrate the HiRes detector. These can be divided up into two major categories: atmospheric monitoring and detector calibration.

The HiRes detector uses scintillation light and the propagation of that light through the atmosphere to determine the energy of the shower. The amount of light lost traveling from the shower to the detector is important in making accurate energy measurements. Two important aspects of understanding the atmosphere were weather monitoring and atmospheric calibration using known light sources.

The weather was monitored by a cloud monitor and the operators. Operators were required to take an hourly survey and record the results in log files. The operators would determine if it was safe to continue operating the detector and make note of any weather problems. They would then enter a "weather code" into the logs. These codes were used only to select nights with few or no clouds.

Other sensors were also installed to give a more objective measurement of the weather. A cloud monitor measured the temperature of the night sky. Clouds appear as warm spots against the night sky, allowing infrared cameras to see them. Monitors for wind speed and rain were also installed. These measurements were used mainly to determine if it was safe to operate the detector and are generally not used in analysis.

To understand atmospheric attenuation, several known light sources were measured by the detector both during operation and on nights designated for calibration. The main part of the atmospheric monitoring was done using several lasers. Two steerable lasers were installed, one at HiRes 1 and one at HiRes 2 (the location of these lasers was constrained by the military). Each steerable laser used frequency tripled YAG lasers to produce 355 nm light. The lasers were fired both vertically and in set patterns during the night.

The HiRes 1 laser had a maximum energy of 50 mJ, while the HiRes 2 laser had a maximum energy of 7 mJ. The energy was measured at each shot by a photodiode. Optical filters and polarizers reduced the amount of beam contamination from other frequencies and circularly polarized the light. The lasers themselves were mounted on steering assemblies that allowed them to rotate as needed. This setup allowed for shots to be fired at known energies in known directions with a known polarization.

These lasers fired patterns of 1000 to 1300 shots per hour. These shots were controlled by programs that were initiated by HiRes 1 operators at the beginning of the night and then ran automatically. The patterns were controlled by scripts on the PCs that controlled the lasers. In addition to the shots described by these scripts, the lasers were able to fire in the direction of high energy shower candidates. These shots fired a set of patterns in the plane of high energy candidates a short time after they had been recorded by the detectors.

In addition to the lasers, a series of 11 Xenon flashers were installed at set positions relative to the detectors. Each flasher consisted of a Xenon bulb located at the focal point of a 20cm spherical mirror. The flashers were controlled by a radio link located at HiRes 2. At the start of the night, the HiRes 2 operators would initiate a script that controlled the firing pattern of the flashers. Five pairs of these flashers were located at distances of 1km, 2km, 4km, 8km, and 10km from HiRes 2 directly between the two detectors. An inclined flasher was located on the other side of HiRes 1.

The flashers provided an inexpensive reliable light source. They produced a pulsed beam of light with energy of 100 μJ in the 300-400nm range. Because the flashers were located on the ground pointing up, they were affected by local conditions like ground fog. However, they provide a good indication of clouds and haze in the atmosphere.

The detector calibration was performed using two standard light sources. The first was a system of fiber optics that illuminated all of the PMT cameras at a site with light from a 355nm YAG laser. This system was run at the beginning and end of each night. Both sites had this type of laser calibration.

The second light source used was a Roving Xenon Flasher (RXF). The Roving Xenon Flasher was mounted and moved from telescope to telescope. On each telescope, it would fire a set number of pulses that were then measured by the detectors. The RXF itself could be calibrated both before and after this procedure with NIST traceable detectors. This was used to determine absolute calibration of the PMTs. This procedure was time consuming, so generally done only at the beginning and end of each run. YAG samples were also taken when doing RXF calibrations to allow for cross calibration. The combination of YAG and RXF measurements could then be used to determine the combined gains of the PMTs and read-out electronics and the stability of the detector over time.

CHAPTER III

EXOTIC PARTICLES

UHECRs measured by HiRes during its operational lifetime have energies several orders of magnitude higher than those achieved in current ground-based accelerators. This makes the HiRes data set an interesting sample in which to search for exotic particles. The HiRes data provide a unique opportunity because of the large exposure of the data set and the stereo configuration of the fluorescence detectors. Several such searches have already been done, primarily for neutrinos [14, 15]. These searches use the low interaction cross sections of the neutrino to narrow possible candidates based on local topography and direction of travel. More specifically, these searches look for events traveling upward or sideways in the detectors view.

The stereo configuration of the HiRes detectors allows for a particularly unique search for exotic particles. The particles measured by HiRes have energies in excess of $10^{17.5}$ eV, or relativistic γ factors in the range of 10^{5}-10^{11} depending on primary nucleus mass. With these ultra-relativistic energies, even the secondary particles produced in the extensive air shower are highly relativistic. The air shower from an ordinary hadronic primary cosmic ray is often modeled as a "pancake" of particles a few meters in thickness propagating at essentially the speed of light. The assumption of light speed propagation is essential for monocular reconstruction of event trajectory based on the arrival times of

the fluorescence signal at the phototubes. Figure 7 shows a diagram of a single detector viewing the shower. Equation 11 shows the time lag for a given tube.

$$t = \frac{1}{v_{air}} \frac{|\overrightarrow{R_p}|}{\sin\theta} - \frac{1}{v_{shower}} \frac{|\overrightarrow{R_p}|}{\tan\theta} = \frac{|\overrightarrow{R_p}|}{c} \tan\frac{\theta}{2} \tag{11}$$

Here, t stands for the time in any given tube. $\overrightarrow{R_p}$ and the angle θ are shown in Figure 7. The term $\frac{1}{v_{air}} \frac{|\overrightarrow{R_p}|}{\sin\theta}$ gives the amount of time light spent traveling through the atmosphere from the shower to the detector. The term $\frac{1}{v_{shower}} \frac{|\overrightarrow{R_p}|}{\tan\theta}$ describes the time the shower spent moving through the atmosphere to the point where the tube could view it. Assuming the factor of v in both is just the speed of light the simplification shown can be made. Given this relation, R_p can be calculated by minimizing a χ^2 fit given in Equation 12.

$$\chi^2 = \sum_i \frac{1}{\sigma_i^2} \left\{ t_i - \left(t_0 + \frac{|\overrightarrow{R_p}|}{c} \tan\frac{\theta}{2} \right) \right\}^2 \tag{12}$$

Here, t_i is the time at which an individual tube triggered at, and t_0 is the first recorded trigger time in the shower. This allows for R_p and θ to be calculated, giving the geometry of the shower. If the speed of the shower in the atmosphere were unknown, minimizing this function would not result in a single value for R_p.

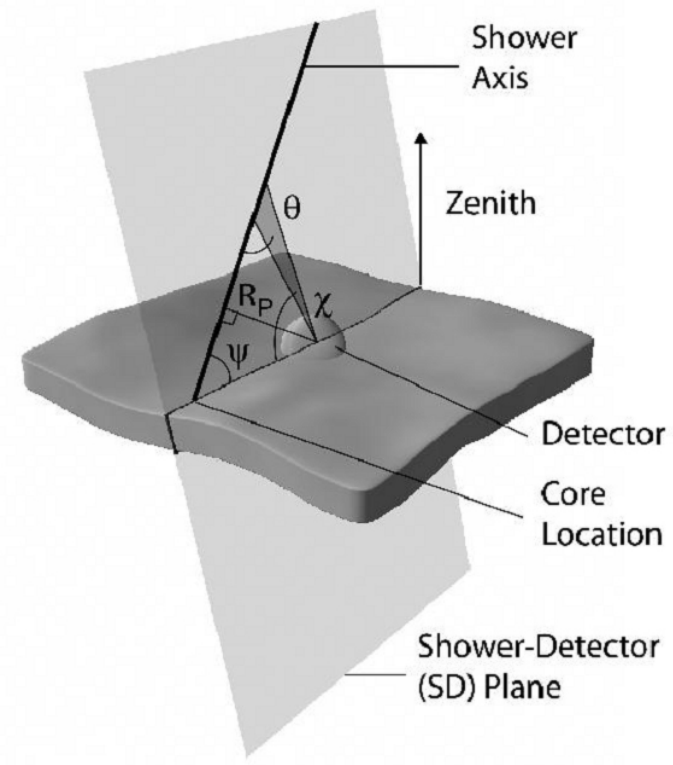

Figure 7 : Diagram for monocular reconstruction showing various reconstructed fit parameters.

In stereoscopic observations, the trajectories of the EAS can be determined by intersecting the shower-detector planes (SDP) observed from each of the two detector sites. The shower-detector plane is reconstructed to better than 0.5° precision using the pattern and the timing sequence of the phototube hits alone without assuming the speed of light for propagation. This is shown in Figure 8.

As the actual tube times are not used to fix geometry, the timing information from the individual tubes can then be applied to directly calculate the speed at which the shower is moving through the atmosphere. This provides HiRes with the ability to search for particles moving faster or slower than lightspeed.

The energy range covered by the HiRes experiment has not yet been accessible to accelerator based experiments or to any sort of measurement where particle-by-particle identification is possible. The nature of any exotic events where the air shower propagates at unexpected speeds is therefore entirely open to speculation. In the remainder of this chapter, we will examine one of several proposed candidates: strangelets.

History of Strangelet Observation

In 1973, the Japanese and Brazilian Emulsion Chamber Group observed strange looking cosmic ray events in their emulsion chamber [16]. These events produced showers with a large number of hadrons but few gamma rays. The Chacaltaya Emulsion Chamber Experiment was a two-story emulsion chamber using x-ray film to track showers. For these particular events, the bulk of the shower was found in the lower chamber. In the upper chamber, only small events seemed to share the same direction.

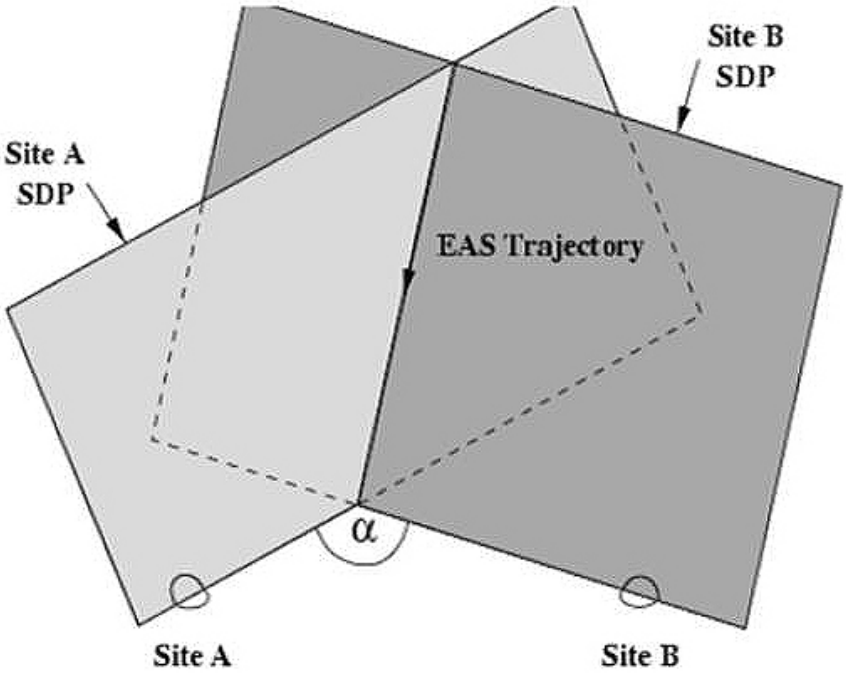

Figure 8 : Plane Crossing for Stereo Reconstruction

These odd events were quickly dubbed “Centauro” after the mythical Centaur because of their top down asymmetry [17].

The properties of these events were soon interpreted to be inconsistent with standard models of particle interactions. This led to a number of proposed explanations, including new exotic particles. Although the effect was eventually explained through detector systematics [18-20], the initial excitement sparked a number of speculations for UHECR of exotic composition.

Among the explanations offered was the possibility that these cosmic rays were the result of a new class of particles called strangelets. Strangelets are a hypothetical form of matter consisting of equal parts strange, up, and down quarks. Several unique properties make them ideal candidates for exotic cosmic ray events.

Basic Properties of Strangelets

One of the most striking properties of strange quark matter is the possibility that it is absolutely stable at zero temperature and pressure [21]. At first glance, this seems unlikely. Nuclear hadrons have been observed to be stable and not decay into quark matter. However, known hadrons containing one or more strange quark are all unstable. The reason for this can be seen by comparing the masses of strange baryons to the neutron and proton. Table 1gives the masses and strangeness for some common baryons.

This listing shows that as strangeness increases, mass tends to increase also. For this reason, substituting up and down quarks with strange quarks in normal matter does not increase the stability.

Table 1: Masses and strangeness for common baryons

Baryon	Quark Content	Mass (MeV/c^2)	Strangeness
n	*udd*	939.6	0
p	*uud*	938.3	0
Λ^0	*uds*	1115.7	-1
Σ^0	*uds*	1192.6	-1
Ξ^0	*uss*	1315	-2
Ω^-	*sss*	1672	-3

However, as the strangeness continues to increase (beyond A~100), some models have shown strange nuclei might become stable [22]. Calculations done using the MIT bag model show that the energy per baryon in strange matter can be lower than that of normal matter by as much as 50-70 MeV [21] in the high mass regime. However, the lower energy does not necessarily imply that normal nucleons (p,n) would decay into strange quark matter. There are two main reasons for this. First, this type of decay would likely be mediated by a high order weak interaction to translate u and d quarks to strange quarks. The rate of this reaction would be extremely small, making the actual decay difficult to observe.

In addition, as the atomic number decreases in strange quark matter, surface effects can make the nuclei unstable even if it is stable in bulk [22]. When an individual nucleus did decay into strange matter this instability would tend to cause further decays. To avoid these two effects, strange quark matter would have to be created in energetic environments where it could achieve a sufficiently high atomic number to be stable before decaying into something else.

Strange quark matter can grow in energy by absorbing nuclei. Absorption of protons would be obstructed by the Coulomb barrier much like that in normal nuclei. This would prevent charged particles from being easily absorbed, but would allow neutrons to be absorbed freely. There do not seem to be any barriers to this type of

growth, meaning that an individual strange particle could grow until it exhausted its source of neutrons. There are suggestions that neutron stars could be made entirely of quark matter, although there is still strong debate on the issue [21, 23, 24] and the majority opinion does not favor this nonstandard scenario.

The possibility of growth by neutron absorption leads to another striking property of strange quark matter. Because it is energetically favorable to absorb neutrons, the overall mass of strangelets can be very large. Atomic number (A) for strangelets is allowed to vary from small particles with A~10 to entire neutron stars being made up of strange matter. In literature, the term strangelet has been used to refer to strange quark matter with mass A ranging from $10^2 < A < 10^7$ [22]. This loose convention will be followed here.

At the low end, strangelets of A~100 are smaller than the typical Compton wavelength of an electron. At this size, positive quark constituents can group at the surface and strangelets can carry a small charge. This charge is small compared to the mass. The charge to mass ratio of strangelets would be much smaller than the charge to mass ratio of normal nuclei. Even with the charge, surface effects could overwhelm the Coulomb effects in the strangelet and prevent fission from occurring. More importantly, because the charge to mass ratio is smaller than that of normal nuclei, it is reasonable that strangelets could have much larger charges than normally allowed [22]. The importance of this property will be discussed when addressing strangelets as candidates for high energy cosmic rays.

The Possible Role of Strangelets in Cosmic Rays

The notion of a new ground state to hadronic matter involving ultra heavy strange matter is a very exciting one. The problem lies in determining if the theory is viable. This task inevitably falls into the realm of experimentation. Strangelets would not be found in ordinary environments on Earth because of their peculiar properties [22]. That leaves two options – create them or observe strangelets created elsewhere. Creating strangelets that can be observed is very difficult at currently achievable accelerator energies. Observation in detectors is further complicated by the lack of knowledge on specific interaction mechanisms. Both of these difficulties could possibly be avoided by observing strangelets created elsewhere.

Two major sources for Strangelets have been proposed. Strangelets could exist as relics from phase transitions in the early development of the universe. They could also be the result of collisions from strange stars [21, 25] (stars made entirely of strange matter) or produced in super novae. Strangelets produced in collisions with strange stars would add to the cosmic ray flux.

Two particular traits of strangelets could lead to observable signals. The first is the small charge to mass ratio. Because of the low charge and high mass, strangelets would be accelerated more efficiently by shock waves (Fermi Acceleration) [26]. These strangelet cosmic rays would not be affected by the GZK cutoff in the same fashion as normal nuclei. As such, they are excellent candidates to explain cosmic rays that fall above GZK energies. Several attempts have been made to calculate a flux for cosmic rays based upon propagation models from sources [24-26]. The low charge to mass ratio could allow for detection in experiments like the Alpha Magnetic Spectrometer [25].

The second trait that could lead to detection is the large mass of the strangelet. For this trait to be measurable, there must be some form of interaction in the atmosphere. As mentioned previously, little is known about the exact manner in which strangelets might interact with other particles. Theoretical work has shown that spallation in the atmosphere might be a plausible interaction method [27]. This evaporation could cause tracks that resemble air showers initiated by hadronic nuclei. However, because mechanics for particle interactions are different from those of normal hadronic nuclei, there is no firm basis for the expected shower profile. For that reason, shower profile was not used as part of this analysis.

Because of the lower speeds and higher dE/dx, strangelets would tend to be stopped much higher in the atmosphere. However, as Wu et al. have shown, much larger strangelets could penetrate deep enough into the atmosphere to be observed [27].

A fluorescence detector uses the atmosphere as a calorimeter. This allows for a measurement of the energy of the primary that initiates the shower. Because the energy of a particle is both a function of mass and speed, very slow showers exhibiting high energies can be used as a signature to strangelets in the atmosphere.

The ability to measure showers of this type depends on two assumptions for HiRes. First, the spallation process would need to result in secondary showers that produced measurable fluorescence light. The second assumption is that the detector can determine the speed of the shower with sufficient resolution to see possible events. For this work, the first is assumed to be true. To understand the second assumption, part of this work included studies of the sensitivity of the HiRes detector to particles at different

speeds. This work was done mostly using Monte Carlo methods. It will be discussed in more detail in Chapter IV.

CHAPTER IV

MONTE CARLO

At the simplest level, Monte Carlo methods refer to simulation procedures that use repeated random sampling to analyze a problem. A basic example often cited is the calculation of π. This method is similar to that used in calculating the acceptance and efficiency of detectors, particularly in particle physics. Because of this similarity and the simple nature of the model, it is worthwhile to review the basic procedure. The calculation begins by considering a circle inscribed in a square as shown in Figure 9.

The area of the circle and square are given by equations 13 and 14, respectively.

$$A_{circle} = \pi r^2 \tag{13}$$

$$A_{square} = 4r^2 \tag{14}$$

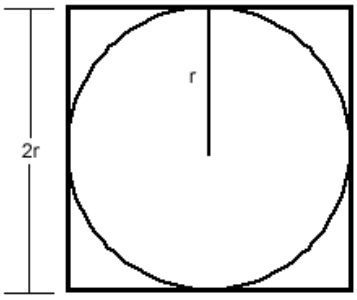

Figure 9: Circle inscribed in a square

The simulation procedure is logically equivalent to taking darts and randomly throwing them at Figure 9.

The darts are thrown in a uniform fashion so that it is equally likely for a dart to hit any portion of the picture. The ratio of darts that fall inside just the circle and those that fall inside the square should be equal to the ratio of the area of the circle to that of the square. This allows one to estimate π using Equation 15.

$$\pi = 4\frac{N_{inside}}{(N_{inside} + N_{outside})} = 4\frac{N_{inside}}{N_{thrown}} \tag{15}$$

The uncertainty in the acceptance fraction $p = \frac{N_{inside}}{N_{thrown}}$ can be estimated as the square root of the binomial variance, given by Equation 16.

$$\sigma_n = \sqrt{np(1-p)} \tag{16}$$

To estimate the confidence interval, the binomial proportion confidence interval can be used. There are a number of ways to do this. The most straightforward is given by Equation 17. This formula holds as long as the ratio is not close to 0 or 1.

$$\pm z_\sigma \sqrt{\frac{p(1-p)}{n}} \tag{17}$$

In this formula, z_σ is the $1 - \sigma/2$ percentile of a standard normal distribution, n is the number of samples, and p is the acceptance fraction from above. By using equations

16 and 17, the accuracy of the simulation can be controlled by generating a sufficient number of events to achieve the desired confidence interval.

More specifically, the algorithm for calculating π proceeds as follows. First, a pair of uniform random deviates is chosen independent of one another to form pairs (x, y), where x and y fall between -r and r. Each pair is checked to see if it lies in the circle by calculating the distance from the center. The value N_{inside} is incremented for each point where the distance from center is less than r, while $N_{thrown}$is incremented for each pair. The uncertainty of the measurement is calculated using 16 and 17. If the uncertainty is within the desired accuracy for the calculation, the calculation terminates and π is given by Equation 15. Otherwise, a new pair is chosen and the steps repeated.

This method has both advantages and disadvantages. One major advantage is that it allows for the calculation of π and an error with very little starting information. As systems get more complex, it becomes more difficult to gather the necessary information to calculate quantities of interest and their errors. For especially complex systems with many features that cannot be described in analytical form, this method may be the only plausible way to calculate certain quantities.

However, there are limitations. Higher precision requires more attempts. In the example algorithm for π, it becomes very time consuming to exceed 4 or 5 significant digits. If the probability density for the random deviate is known, this process can often be accelerated by using an inversion method instead of a rejection method. In general, this is accomplished as follows. Assume a random deviate x on the interval (a, b) with a known probability density distribution $f(x)$ is needed. If $f(x)$ is properly normalized according to equation 18 and is invertible as shown in 19, then a properly sampled

distribution of x can be obtained by generating uniform random deviates y in the interval $(0,1)$ and using equation 20.

$$\int_a^b f(x)dx = 1 \tag{18}$$

$$F(x) = \int_a^x f(x')dx' \tag{19}$$

$$x = F^{-1}(y) \tag{20}$$

Another limitation with both Monte Carlo methods is that the answer is model dependant. If the model chosen is incorrect, then the answer will be also. For example, in the case of calculating π, the model was fairly simple. However, if a triangle were chosen instead of a circle, the answer would be off by a large amount. Even so, as an experiment grows in complexity the use of Monte Carlo becomes more and more favorable.

Monte Carlo: HiRes

Two major factors contribute to the need to use Monte Carlo simulations with HiRes. The first is the complex nature of physical processes involved. The second is the complexity of the detector.

Each EAS involves a large number of particle interactions with the atmosphere. Even if it were possible to perfectly model the atmosphere, each particle interaction generally has a number of possible interaction modes. Given the number of interactions in each shower, it quickly becomes impossible to individually reconstruct every event in every shower.

However, there are many quantities of physical interest that can be observed even if the exact interaction for every particle in a shower is not known. By generating a large number of individual showers using Monte Carlo methods, differences in their visible signature in the HiRes experiment can be compared with measured results to test physical assumptions. For example, changing the composition of primary particles changes the elongation rate, as explained in Chapter I. Once the experimental elongation rate is calculated, it can be compared with elongation rates calculated using Monte Carlo methods with different compositions. This allows for the composition of high energy cosmic rays to be determined within the accuracy of our models without having to reconstruct showers exactly or measuring the primary particle directly.

Several such shower generators exist. For this HiRes analysis, CORSIKA[28] was used. Because the shower generators use physical models to simulate hadronic interactions, there is the possibility that the results become model dependant. This can be checked to a degree by comparing different models with the shower generator. HiRes has used both the QGSJET and SIBYLL hadronic interaction models to generate showers. Studies found that the two hadronic models give essentially the same results for all aspects observable by the fluorescence detectors. In particular, the speed that the shower travels through the atmosphere is mostly model independent. For this work, showers were taken from a library of CORSIKA generated showers using the QGSJET hadronic interaction model.

The HiRes Monte Carlo event generation occurs in three main steps. First, a shower is generated using CORSIKA. These are parameterized and stored in a library of showers. Events are then “thrown” at the detector by selecting showers from the library,

calculating the fluorescence light yields, and propagating that light to the detector. Finally, the detector response is modeled and the raw data recorded along with the "thrown" event information.

Showers are used to generate raw data with known energy, composition, and geometry. They are then fed into the same analysis software used for real data and reconstructed in an identical fashion to real events. Comparisons between the Monte Carlo data and real data ensure that the energy and geometry are correctly reconstructed.

Understanding the response of the detector is critical in this analysis. Therefore, what follows is a much more detailed consideration of the implementation of the Monte Carlo that is used in HiRes as well as the modifications made for this analysis.

Monte Carlo: mc_stereo

Data analysis is discussed in the next chapter. Here, only the process used to generate Monte Carlo shower data will be discussed. Notes will be made where the Monte Carlo was altered specifically for the exotic particle analysis.

The standard program used by HiRes to produce raw stereo data from randomly generated showers is referred to as "mc_stereo." This code was developed by a number of authors and refined over the lifetime of the HiRes project. Mc_stereo consists of two different programs: "stereo_main" and "st_anal_main."

The program "stereo_main" generates a file containing the raw shower data. When run, this program first looks for a set of parameters specified in a file called readinp_dat. Table 2 shows a list of the parameters that are set at runtime. An example of this file is included in Appendix A as a reference for the format of the file.

The variables “cair” and “cshow” were added for this analysis. The units for these variables were chosen to be consistent with previous units used in the analysis software. In testing, if “cair” and “cshow” are set to the same value as previously used for the speed of light (.0002997 km/ns), all results remain the same as before changes were made.

In addition to setting the propagation speed of the shower to values different from that of the speed of light, several other important quantities are set in this file. As illustrated in the table, simulated events can be generated for any given day in the calibration and atmospheric databases. This allows for the comparison of MC events to events recorded by the detector using the actual state of the detector and atmospheric conditions on that day. Alternatively, it is possible to fix the calibration quantities to arbitrary values in the generation of Monte Carlo events. Atmospheric parameters can be set to simulate different viewing conditions. These options allow a great deal of flexibility in testing the response of the detector under different conditions.

The user is also able to select which shower library to use when generating new showers. Each shower library corresponds to a different hadronic model. Shower libraries have been generated specifically for HiRes using CORSIKA for both the QGSJET and SYBLL hadronic interaction models. If desired, the shower libraries can be bypassed and a shower can be generated using the Gaisser-Hillas shower profile.

The Gaisser-Hillas shower profile [29] is described by Equation 21.

Table 2: Input parameters for mc_stereo

Variable Name	Example Value	Function
file1	inpar.dst	Input DST file containing exact set of events to be used
file2	y2003m12d12p001.dst	Output DST file. The date is parsed from the file name and used to determine calibration
file3	eventlog.dst	a log of events generated
file4	dst18.dump	a file to dump specified dst banks during event generation
file5	calib.dst	file containing pedestal and gain values
thelo	0.00	Zenith Minimum
thehi	89.99	Zenith Maximum
philo	0.00	Azimuth Minimum
phihi	360.00	Azimuth Maximum
mod_id	1	Select Shower Generation Type. 0: Gaisser Hillas only 1: QGSJet Corsika 2: Sybll Corsika
ineutrino	0	Boolean – generate neutrino events
laser_opt	0	Boolean – generate laser events
laser_energy	200.00	Laser Energy in micJ
laser_lambda	337.00	Wavelength in nm
laser_rms	5.0	Laser RMS Energy in micJ
laser_origin	20.0 0.00 -0.20	Laser Coordinates in km relative to centroid
rplo	0.50	Min RP
rphi	75.00	Max Rp
hal	24.0	Horizontal Attenuation Length (km)
vsh	1.20	Vertical Scale Height (km)
vmlh	0.0	Mix Layer Height (km)
atm_db_opt	3.20	Atmosphere database height (km)
gamlo	0.00	Min plane angle
gamhi	360.00	Max plane angle
elo	1.0E10	Min Energy (GeV)
ehi	1.0E10	Max Energy (GeV)
t0lo	-1.00	Min Interaction Height (km) neutrinos only
t0hi	2.0E01	Max Interaction Height (km) neutrinos only
iseed	28974593	Seed for random number generator
gamma	-3.017	Spectral Index
a	1	Corsika ID (1 for proton, 56 for Iron)
ntry	10000	Max Tries
nsuk	100	Maximum Successful Tries
use_data_set	0	Boolean – use file1 from above or not
*	0 0 0 0 0 0 0 0	Boolean flags – output variables during run (geo shwr petim S/H fadc fit fitu outp)
*	0 0 0 0 0 0 0 0 0	Boolean flags – dump banks to dst files (fmc raw trg fpho pho fpln pln ftim tim)
Cair	.0002997	Speed of light in air (Tm/s)
cshow	.0002997	Speed of the shower (Tm/s)

* these variables are used to output debug information only. Omitted names because of the number and length

$$N_e(X) = N_{max}\left[\left(\frac{X-X_1}{X_{max}-X_1}\right)^{\left(\frac{X_{max}-X_1}{\lambda}\right)}\right]e^{\left(\frac{X_{max}-X_1}{\lambda}\right)} \quad (21)$$

There are four parameters in this equation: X_1 , X_{max}, N_{max}, and λ. Respectively, these represent the depth of initial interaction, the depth of the shower maximum, the number of particles at shower maximum, and a characteristic length for air showers. They are given in units of grams/cm^2. While X_1 is referred to as initial interaction depth, other studies have shown that fixing the value to 0 has little effect on energy resolution [30]. N_{max} is nominally the number of charged particles in the shower at maximum and is proportional to the energy of the shower.

From this equation, the amount of energy deposited in the atmosphere at each step can be determined. This process involves calculating the number of electrons at each depth and then converting this into the amount of light provided at each depth. Several other factors are involved. A much more detailed description can be found elsewhere [31].

As a more realistic alternative to the Gaisser-Hillas model, the CORSIKA package can also be used to determine number of particles at a given height. Because of the time involved in generating a shower, it is impractical to call CORSIKA at runtime. Instead, a set of shower libraries have been generated and compiled.

CORSIKA allows for several different types of showers to be generated. For this research, showers were generated with iron and proton particles. Shower libraries for neutrinos and lasers also exist, but were not used in this work. These shower libraries contain events generated in (0.1)*log(E) energy bins. At the time of this work, there were between 400 and 500 iron and proton events for each energy bin. For energies that

fall between bins, the parameters for the showers are interpolated from the two nearest bins.

At run time, a random shower is selected from the shower libraries from within the requested energy range and placed in the atmosphere relative to the detector with randomly generated geometry. The randomly generated geometry allows the user to set ranges for the maximum and minimum zenith angle, azimuth angle, and $\overrightarrow{R_p}$.

After the readinp_dat file is parsed for user options, mc_stereo is fed the geometry of the detector. The geometry is stored in two DST banks: geoh_cent and geohr2_cent. These banks contain the locations of each mirror in relation to the HiRes coordinate system. They also contain the pointing angle of each individual PMT and information about the exact positioning of each mirror. The banks have locations to store the center of each detector. However, this location was not stored in these banks. Instead, mc_stereo uses the average position of the mirrors in each telescope to determine where the center of the detector is.

The geometry and user input parameters are passed to a function called "hr_chance." This is the heart of the Monte Carlo process. This function generates all of the physical parameters used in the shower, including the zenith angle, the azimuth angle, and the shower energy. Basic shower parameters are set based on the shower pulled from the shower library. Parameters that were not stored in the shower library are set to random values within the typical range for each value. The order in which the parameters are generated is random. This minimizes chance of correlation due to the random number generator used.

Once the shower itself has been fully defined, the detector itself is modeled. To do this, the fluorescence light generated by the shower is propagated through the atmosphere to individual mirrors. To calculate the fluorescence yield, the shower was divided into segments corresponding to lengths viewed by individual tubes. Because of changes that occurred to this process, a more detailed explanation of this process is necessary.

Initially, mc_stereo generated all showers at the speed of light to calculate tube times and shower geometry parameters. The basic geometry of a shower is shown in Figure 10. First, the overall shower time is calculated using Equation 22.

$$t_{track} = \frac{1}{c_{shower}} r_t + \frac{1}{c_{air}} \left(r_{first} - r_{last} \right) \tag{22}$$

In this equation, r_t is the total length of the visible track, r_{first} and r_{last} are the distances to the first and last viewable portion of the track, respectively. Then the angle between the first tube and the track is calculated using Equation 23.

$$\theta_{view} = -\cos^{-1}(\overrightarrow{p_{uv}} \cdot \overrightarrow{u_v}) \tag{23}$$

Once this angle has been determined, straightforward geometrical calculations can be used to calculate the time at any point on the shower as measured from $\overrightarrow{R_p}$. This calculation is shown in Equation 24.

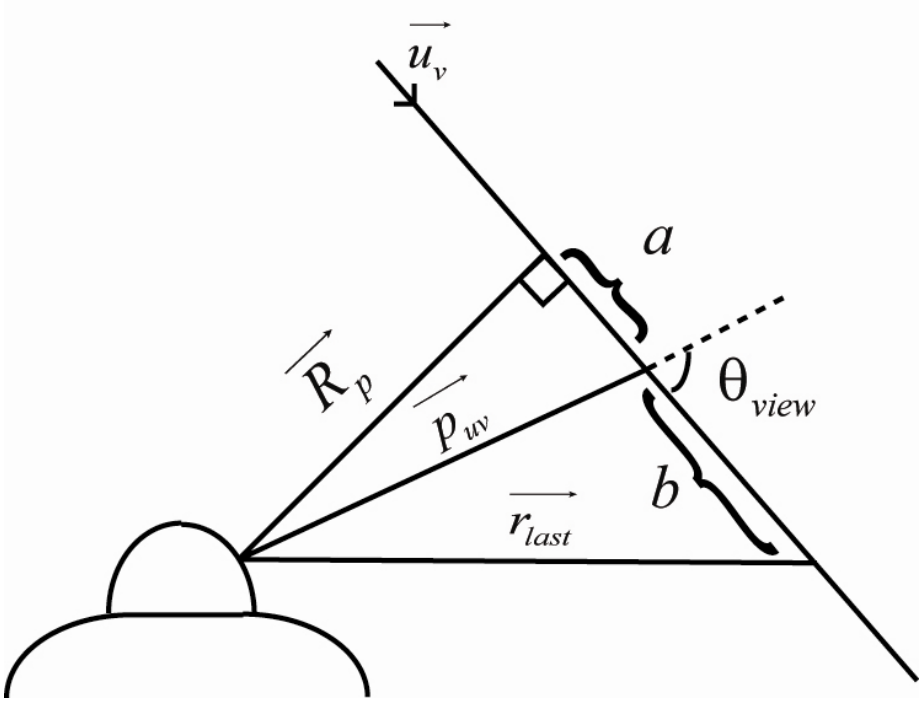

Figure 10: Geometrical representation of shower

$$t_0 = \frac{1}{c_{shower}} a - \frac{1}{c_{air}} |\overrightarrow{p_{uv}}| = \frac{1}{c_{air}} \frac{|\overrightarrow{R_p}|}{\sin \theta_v} - \frac{1}{c_{shower}} \frac{|\overrightarrow{R_p}|}{\tan \theta_v} \quad (24)$$

Here, $\overrightarrow{p_{uv}}$ is the pointing direction of the first tube to view the shower, c_{shower} is the speed of the shower in the atmosphere, c_{air} is the speed of light in air, and $\overrightarrow{R_p}$ is the vector from the detector that intersects the shower axis at a 90° angle.

Once $\overrightarrow{R_p}$ is known, the shower must be divided into segments viewed by the tubes. To do this, first the number of segments is determined using Equation 25.

$$N_{shwseg} = \left\lfloor \frac{\theta_{last\ view} - \theta_{first\ view}}{\Delta\theta_{view}} \right\rfloor + 1 \quad (25)$$

In the actual calculation, the number of segments is compared to the maximum and minimum allowed number of segments. If the number is greater or less than the maximum or minimum, N_{shwseg} is adjusted to match the maximum or minimum. The actual difference in view for the shower is then calculated using Equation 26.

$$\Delta\theta_v = \frac{\theta_{last\ view} - \theta_{first\ view}}{N_{shwseg}} \quad (26)$$

Once this is calculated, the times of each segment measured from $\overrightarrow{R_p}$ can be calculated using Equations 27 and 28.

$$\theta_v = \theta_v + \Delta\theta_v \tag{27}$$

$$t_i = \frac{1}{c_{shower}} a - \frac{1}{c_{air}} |\overrightarrow{p_{uv}}| = \frac{1}{c_{air}} \frac{|\overrightarrow{R_p}|}{\sin\theta_v} - \frac{1}{c_{shower}} \frac{|\overrightarrow{R_p}|}{\tan\theta_v} \tag{28}$$

If the speed of light and the speed of the shower are similar enough to be considered equal, these equations can reduce further. In previous literature this is done frequently, and Equation 28 is reported as shown in Equation 29.

$$t_i = \frac{|\overrightarrow{R_p}|}{c} \tan\frac{\theta_v}{2} \tag{29}$$

This simplification plays two important roles in mc_stereo. First, because equation 24 requires less processing time, all times were calculated using this formula. As part of this analysis, Equation 24 was replaced by 23 or 19 as appropriate. The other role this equation plays is in the determination of the number of photoelectrons per shower segment. This was done in a separate program that did not have access to the original length of the shower segment. At that point in the analysis, only the time of the segment and the magnitude of $\overrightarrow{R_p}$ were initially available for the computation.

Using Equation 29, this is a simple matter of solving for θ_v and plugging it into the appropriate trigonometric identity. However, θ_v cannot easily be determined using Equations 24 or 28. To address this problem, mc_stereo was adjusted so that segment lengths were calculated when determining the time and passed to the function requiring their use later in processing. In theory, these two methods should be identical. In practice, each calculation loses a small amount of precision during the process. As

segments get further away from $\overrightarrow{R_p}$, this small loss in precision can cause a small shift in the length of the segment.

To check the overall effect this change had on mc_stereo, samples generated with the original code were compared to samples generated with the new code using $c_{shower} = c_{air} = c_{original}$. Timing information for the tubes matched exactly within the precision allowed by hardware. Segment length did vary slightly. The effect of this was to increase or decrease the number of photoelectrons generated from that shower segment. However, because this effect was limited to distances far away from $\overrightarrow{R_p}$, in practice the number of photo electrons in a given segment was already small enough that the variation did not appear in actual shower reconstruction.

After the shower was divided into segments, contributions of scintillation and Cherenkov light are calculated for the shower segments. Using one of the models described above (Gaisser-Hillas, QGSJet, or Sybill) the number of photoelectrons for each segment is generated. This process is done using measured fluorescence yields. The number of charged particles for each segment is calculated. The average energy loss of an electron in the shower as a function of age is also calculated. The total yield can then be calculated using Equation 30[32].

$$Y = \frac{dE/dx}{\left(dE/dx\right)_{1.4MeV}} \rho \left\{ \frac{A_1}{1 + \rho B_1 \sqrt{T}} + \frac{A_2}{1 + \rho B_2 \sqrt{T}} \right\} \tag{30}$$

Here, A_1, A_2, B_1, and B_2 are constants. Their values are 89 m^2/kg, 55 m^2/kg, 185 m^2/kg, and 6.50 m^2/kg, respectively. With the total yield, the scintillation light can then

be calculated using an isotopic distribution given by Equation 26.

$$\frac{d^2N}{dld\Omega} = Y\frac{Ne}{4\pi} \tag{26}$$

Cherenkov light is also produced by the shower, and can add the signal produced by scintillation. This light must also be taken into account. Most Cherenkov light is directed along the shower axis. However, shower geometry and atmospheric scattering can lead to Cherenkov light in the direction of the detector. To calculate Cherenkov light, the total amount produced per meter is calculated [31]. The amount scattered from the shower can then be estimated and added to the total light signal passed to the phototubes.

The total length of the track as viewed by the detector is then calculated. Tracks that fall below a cutoff point are removed from consideration at this point. The lateral shower distribution is then implemented.

Using the segmented shower, ray tracing is performed to determine which tubes receive a signal. The ray tracing uses mirror shape, mirror reflectivity, the shape of the PMT cluster, and the UV filter to account for each mirror's geometry. It also takes into account cracks between cluster PMTs. The Number of Photoelectrons (NPE) for each tube is calculated using quantum efficiency curves from the tube manufacturers. A simulated signal is generated for each tube using the gain of the PMT and the pre-amplifier. The time at which each tube receives a signal is calculated.

The Monte Carlo program can also simulate noise tubes and electronics noise for a given shower. When used, this adds noise to each signal following a Poisson

distribution. Random noise tubes are added with the same mean and sigma as the actual data. After the response of the phototubes has been calculated, this is fed into a set of programs designed to simulate the electronics of each rack. The electronics simulation did not change for this work, and is described in detail in other documents [28].

At this point, the data calculated is output in banks to preserve all mc shower information and the simulated electronics information. The Monte Carlo set is stored fmc1 and fmc2, while the real data set is stored in fraw1 and hraw1 just as recorded data would be.

Monte Carlo Generated for Exotic Particle Search

To test the acceptance of the detector, a number of Monte Carlo sets were generated for this thesis. Shower sets were generated with energies starting at 10^{18}eV and then generated in half energy decades to 10^{20}eV. For each energy decade, a set of iron and proton events were generated with speeds of .050, .100, .150, .200, .299, .400, and .600 nm/s.

Each set allowed showers with Zenith angles between 0 and 89.99 degrees. The azimuth angle was allowed to vary between 0 and 360 degrees. RP was allowed to vary between .5 and 75 km. Each set attempted a maximum of 50,000 simulated events and stopped after 20,000 had been successfully "thrown." The number of actual events that triggered the detector varied from set to set.

These sets were then used to calculate the aperture at each speed and energy. The results of this calculation are shown in Chapter IX.

CHAPTER V

HIRES DATA SET AND STEREO RECONSTRUCTION

Reconstruction

Before the raw data set collected by the detectors is useful for most physical analysis, it must be processed into parameters describing the observed shower. There are two categories of physical information calculated from the data. Those in the first category can be determined directly from each individual shower measurement. Examples of these include X_{max}, shower geometry, and total energy in the primary. The second category of information includes quantities that must be calculated from the collective properties of the full data set, taking into account the finite capabilities of the detector system. Examples of quantities derived from statistics are the elongation rate and integrated flux.

For both of these categories, the raw detector data from each event must first be converted into physical and mathematically meaningful quantities. This is generally referred to as reconstruction. HiRes has used both monocular and stereo reconstruction analysis methods to reconstruct the data taken during its operation. As mentioned previously, monocular reconstruction assumes the shower propagates through the atmosphere at the speed of light. This makes it unsuitable for the analysis used in this study and is not described here. More information on monocular reconstruction can be found elsewhere [28].

Throughout the course of the HiRes experiment, several versions of stereo reconstruction were developed largely independent of each other. These variants use different methods to reconstruct showers from the data. While that is useful for checking the accuracy of the reconstruction, it presents a unique problem for this study. Three main stereo reconstructions have been done for the HiRes group. In order to avoid bias, all 3 were considered for use in this work.

However, two of the stereo reconstructions available at the time the work for this study was done included tube timing information in the geometrical reconstruction and assumed the speed of light when fixing the geometry of the shower. This assumption made them unsuitable for this method of calculating shower speeds. The third reconstruction relied purely on the crossing of shower-detector planes for calculating geometry, and relative timing information was used only to search for noise tubes. More detailed information on the reconstruction has already been covered by other collaborators [33]. However, due to the importance of the reconstruction to this work, a general overview follows.

Preselection

Before starting actual reconstruction, events were removed based on GPS time stamps. This was done to separate the two lasers used for atmospheric calibration and the vertical flashers. A set of rough random noise filters was also run to remove events like the triggering of entire mirrors. After these cuts were made, recorded events were passed on to the actual stereo reconstruction routines.

Stereo Reconstruction: Raw Data

Both HiRes detectors operated and recorded data independently of each other. While operated independently, certain basic quantities were recorded by both. For each tube trigger, a time was stored. This time is based on GPS clocks at each site. Stereo reconstruction uses this GPS time to match events between sites, so the accuracy of these clocks is vital to correctly reconstruct showers. Drift in either of the GPS clocks could result in differing times for shower triggers in each detector, making it impossible to match events to the same shower. Before any analysis was done, data from known sources seen by both detectors (e.g., the flashers described in Chapter II) were compared to ensure the clocks were accurate. If major differences were found, the raw data could be adjusted based on the difference in time between these known sources[34].

Other basic information about the tube recorded for each site included mirror number, site, tube number, and tube signal. The tube signals were dependant on the type of electronics, and were stored differently depending on detector. HiRes 2 used an 8-bit FADC system to digitize signals from the 42 telescopes. In total, there were 10,752 phototubes and 13,440 FADC channels. Incoming data were digitized into 100ns bits. When triggered, these data were then written out and stored locally at the detector sites. The raw data were transferred into flat binary files (referred to as DST files) and back to the University of Utah to be analyzed daily.

Figure 11 shows a sample FADC event. The histograms show the FADC profiles for 8 of the viewing channels in a 14μs window each. The corresponding event display is

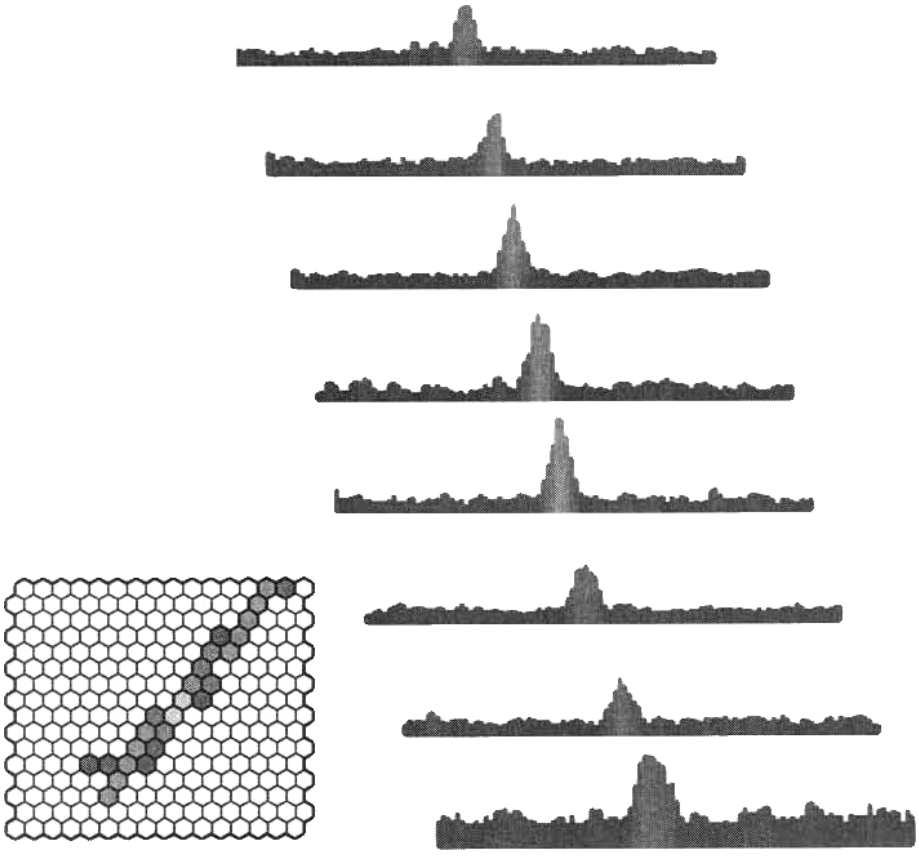

Figure 11: Sample FADC event

shown in the lower left hand corner. These profiles were then fit to determine the location of the peak. This peak location was recorded as the trigger time for each individual photo tube. The total signal was given as the sum of the signals in each of the recorded 100ns time bins in the triggered tube subtracting the baseline "pedestal." Direction of the event in the telescope could then be inferred from the relation of the tube times without needing to assume a speed of shower propagation.

HiRes 1 used "sample-and-hold" electronics. For each tube in an event, an integrated channel signal was output. The time for each tube was given as the time the tube actually triggered in the detector, which corresponds approximately to the leading edge of the peaks seen in Figure 11 and introduces a small pulse-height dependant offset. This "walk" correction tends to shift all the tube times, but the pulse-height dependence causes the shift to be different tube to tube and, as a result, HiRes 1 speed measurements were less precise than HiRes 2.

Reconstruction Process

The reconstruction process involves a series of calculations and cuts. A general overview of the process is given here. Details can be found in other works [33].

Before continuing with the actual reconstruction process, a critical technical detail for the collaboration is worth noting. Because the actual processing code was written at different times by a number of different people, the order in which the calculations and cuts were made does not always directly follow the physical reasoning behind them. When calculating the number of photoelectrons for each mirror, corrections had to be made for both the mirror reflectivity and atmospheric conditions. Parts of the mirror reflectivity correction were applied in initial stages of processing. However, as only part

of the correction was applied, photons recorded at this stage were not normal photons on the cluster. Instead, another portion of mirror reflectivity was applied only in the final stages of processing. Because time information for the phototubes was folded into geometry in the final stages of processing, this study could not use that information. Instead, the necessary time-independent geometry was extracted earlier. The end result is that the photon numbers in this study are not normal photons on the cluster. However, because shower profiles were not examined in detail for this analysis, this has no impact on the results of this study.

Basic reconstruction attempts to determine the geometry and amount of fluorescence light generated by an event. For stereo detectors, geometry can be determined using trigonometry without using timing information.

To do this, tubes that triggered are fit to a plane called the shower detector plane. This is done separately for each site. Each tube that triggers has a known location in space and a pointing direction. The shower detector plane is a best fit for a plane that passes through the center of the detector and the triggered tubes in the direction they point.

Once the shower detector planes are determined, the shower axis can be determined by "crossing" the two planes. Mathematically, the cross product between the normal vectors for each plane gives a vector perpendicular to both planes. That vector is parallel to the line formed by their intersection. Once that vector is known, all that remains is to find one point on that line. This can be done by writing down the equations for a line in each plane where the vertical (z) component is zero. Finding the point where these two lines intersects gives the "core" location of the shower. It should be noted that

core location in this sense refers to the z = 0 point. Because local terrain varies in height, this does not correspond to where the shower actually impacted the ground. The vector found by the cross product of the two planes and the core location define the shower axis.

A vector which intersects the shower axis at a 90° angle is calculated for each detector. This vector is the $\overrightarrow{R_p}$ vector that has been mentioned several times previously. From the shower plane and $\overrightarrow{R_p}$ vector, the zenith and azimuth angle of the cosmic ray are found. Figure 12 illustrates the geometry calculation done by intersecting the shower detector planes.

In addition to calculating the geometry, the amount of light from each phototube is calculated. The number of photons incident on each phototube is determined using the known tube and electronic gains stored in the calibration database.

The number of photons generated by the shower is then calculated by propagating the signal back through the atmosphere. This requires the geometry of the shower to be known so that the amount of Rayleigh scattering and aerosol attenuation (the latter calculated from aerosol calibration database) can be calculated. This allows for the amount of fluorescence light generated by the shower to be calculated. From here, the process followed is very similar to that described in Chapter IV for Monte Carlo. The resulting points are fit to a shower profile specified at run time. For this study, the profile used was a parameterized profile generated from Corsika Monte Carlo using the QGSJet hadronic interaction model. This profile fit gives the shower maximum X_{max} and total energy of the primary.

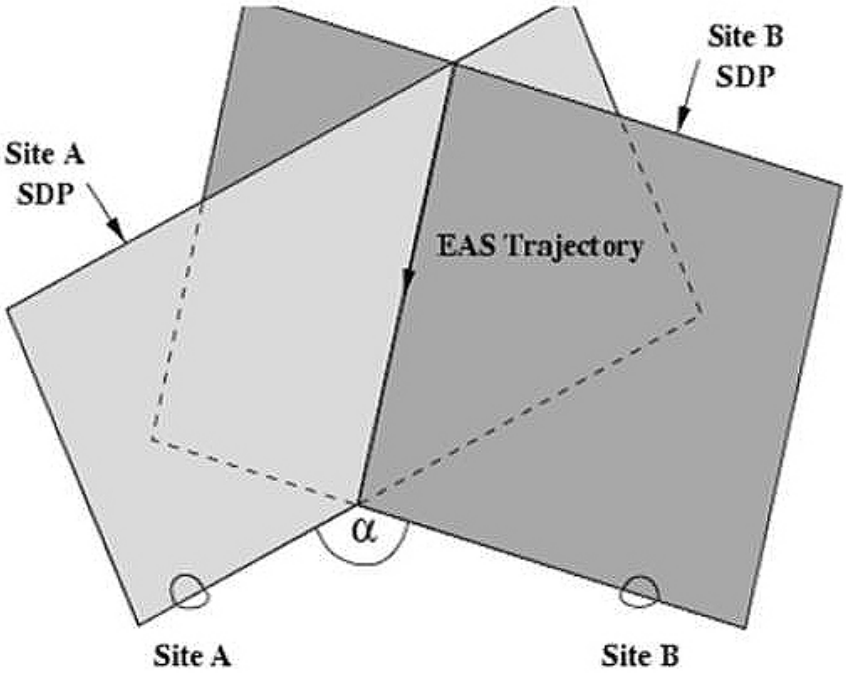

Figure 12: Stereo geometry calculation

In the actual reconstruction software, these steps are divided up into a number of separate routines with quality cuts at each stage. It is common to refer to a set of data according to the routine in which it was generated. As such, it is worthwhile to explain briefly what happens in each phase of reconstruction.

For historic reasons, each routine is generally referred to as a "Pass.". Pass 1 and 2 are in general done at the same time. They refer to manipulations done on the raw data to get them ready for processing. This includes writing them into appropriate DST banks and separating out system information.

In Pass 3, the SD plane fit for each site is calculated. Minimum and maximum cuts are made on track length. At this stage, these cuts were 57.0 (36.0) degrees for HiRes 2 (HiRes 1) maximum track length, and 6.0 (3.0) degrees for minimum track length.

In Pass 4, the planes are crossed, resulting in the shower geometry. First, each tube is checked to see if it meets certain criteria for inclusion. If the number of photoelectrons per tube falls below 1.0, the tube is rejected. Events with fewer than 6 tubes are rejected. If the average number of photoelectrons in the event is less than 6, the event is rejected.

If the event survives to this point, the planes are crossed and the shower axis, $\overrightarrow{R_p}$, zenith, and azimuthal angles are determined. If this fails, the event is cut. The shower is then divided into angular "bins." Each angular bin contains the sum of signals for phototubes that view an angular segment of the shower. A molecular atmosphere model is then applied to the binned signal to account for attenuation. Using experimental

fluorescence yields, the total amount of light generated by the shower is determined. For this study, the fluorescence yield calculated by Kakimoto [32] was used.

After binning is done, the event is fit to a profile as described above. A χ^2 fit is performed on the trigger times for the phototubes. If the event fails to fit, the event is thrown out. This fit does not assume the speed of light. It is only a check on relative timing. For reference, Table 3 shows all cuts made during the reconstruction process.

In addition to the processing done to this point, additional processing sometimes referred to as "Pass 5" can be carried out. For this study, reconstruction was taken through Pass 4 only. Pass 5 redoes the fitting for shower detector planes using timing information to improve the plane fits. The binning is redone. For Pass 5, two separate forms of binning are used: angular binning and time binning. The light signal for the new bins is then adjusted for attenuation losses in the atmosphere and a fluorescence yield is applied. The new signals are fit to shower profiles and statistical information about the shower recorded. Detailed information can be found in William Hanlon's thesis [33].

Table 3: Cuts performed during reconstruction

Pass	Cut	Value
Pass 0-2	HR2SLS, HR1SLS, Roving SLS	GPS time
Pass 0-2	Flasher	GPS time
Pass 0-2	Event lacks both detectors	na
Pass 3	Min Track Length HR2 (HR1)	6° (3°)
Pass 4	Minimum PE in a tube	1.0
Pass 4	Minimum Tubes	6
Pass 4	Minimum Average PE for Event	15.0
All	failure on any fitting parameter	na

Data

The HiRes detector ran in stereo mode from December 1999 to March 2006. At the time this thesis was written, calibration data were available only up to November, 2005. As such, this date was used as a cutoff for events. Table 4 shows the events remaining after various stages of processing. In all, over 2,000,000 stereo triggers were recorded. A large portion of these events were calibration sources or noise. Approximately 85,000 of these events survived plane fitting. As shown in Table 4, The majority of these events made it past Pass 4.

As a note for collaborators, this number does not include any quality cuts. During Pass 5, quality cuts are made. The number of events left after all quality cuts are made at all energies is approximately 11,500. As mentioned previously, Pass 5 makes several assumptions that make it unsuitable for this particular search.

Table 4: Events left after each stage of processing

Stage	Events
HiRes 1, pass 1	136,099,385
HiRes 2, pass 1	50,685,473
Stereo Pass 1	2,658, 769
Stereo Pass 2	300,290
Stereo Pass 3	84, 752
Stereo Pass 4	83,890

CHAPTER VI

SHOWER SPEED DETERMINATION

After the event reconstruction described in the previous chapter, processing diverges based on the type of information desired. The process for spectrum analysis can be found in other works [33]. For this study, we proceed next with the determination of the speed of the shower and related statistics. The next three chapters cover this process. This chapter covers the basic formulation for determining the speed of an individual shower. The succeeding chapters describe the data selection and statistical analysis.

Up to this point, only the shower trajectory has been extracted from the raw data for each individual shower. The next stage is to calculate the speed at which the shower develops in the atmosphere. This is done in a two-step process. The first is to use the reconstructed trajectory to determine a time and distance along the shower for every "good tube." The second is to fit those points to a line whose slope represents the speed of the shower and refine that fit to eliminate noise tubes. Each will be discussed in turn.

Determining Time and Distance

The calculation of the speed of the shower requires a sequence of distances and times corresponding to each PMT hit by the event. Each tube views a portion of the shower and contains a trigger time. Using the $\overrightarrow{R_p}$ vector described in Chapter V as the space-time origin, the shower trajectory is used to calculate the distance along the shower

to the center of each triggered tube, and to calculate the time that the shower was at that point. This means correcting for travel time of light from the shower to the detector.

Each tube views a finite portion of a shower. In this analysis, only one extracted time (trigger time for HiRes 1 and the peak signal time for HiRes 2) is used. Therefore, the distance along the shower to the location corresponding to the center of the tube is used for that tube's distance. However, the lines of sight of the tube centers do not in general intersect the shower axis obtained from geometrical reconstruction. Thus, we use the point of closest approach between the shower axis and the line of sight of the tube as an approximation for the light propogation distance.

The shower axis is defined by the geometry calculated in stereo reconstruction. In vector form, it can be written as shown in Equation 31.

$$\vec{s} = \overrightarrow{r_p} + b \cdot \overrightarrow{u_v} \tag{31}$$

Here, $\vec{s}$ is the vector representation of the shower axis, $\overrightarrow{r_p}$ is the vector from the center of the detector that intersects the shower axis at a 90° angle, b is a scalar distance parameter, and $\overrightarrow{u_v}$ the unit vector pointing in the direction of shower propagation along the shower axis.

The tube's line-of-sight is defined by the surveyed geometry of the mirrors. The line-of-sight can be represented as a vector line by Equation 32.

$$\vec{r} = \overrightarrow{m_v} + a \cdot \overrightarrow{t_v} \tag{32}$$

Here, $\vec{r}$ is the location of an arbitrary point along the tubes line-of-sight, $\overrightarrow{m_v}$ is the vector from the center of the HiRes coordinate system to the surveyed center of the telescope, a a scalar distance parameter, and $\overrightarrow{t_v}$ a unit vector giving the direction in the sky that a tube points relative to the HiRes coordinate system.

At this point, it is necessary to include a critical technical detail for the benefit of collaborators. For reconstruction, a geometrical transformation is applied such that each mirror is moved to the origin before the geometry for an event is determined. This corresponds directly to setting $\overrightarrow{m_v}$ to the center of each detector site regardless of where the mirror is actually located in the detector site. This leads to a small shift in the distance (up to ~30m) between the mirror and the event calculated using Equation 32.

After the distance to the shower is calculated, a small correction can be applied to account for this geometrical calculation. In practice, it was found that this correction was small and nearly equal for every tube. While the distance itself was not exact, because the correction applied was nearly equal for every tube, it did not significantly alter the slope. It did significantly alter the time necessary to calculate the speed of a shower and greatly complicated the process of plane rotation described in Chapter VII. For this reason, the correction was omitted for all processing.

Figure 13 shows the two lines described by Equations 31 and 32. The two detectors are represented by half spheres on the ground. The shower axis represented by the thick line impacting the ground between them. The vectors and scalars are labeled as used in Equations 31 and 32.

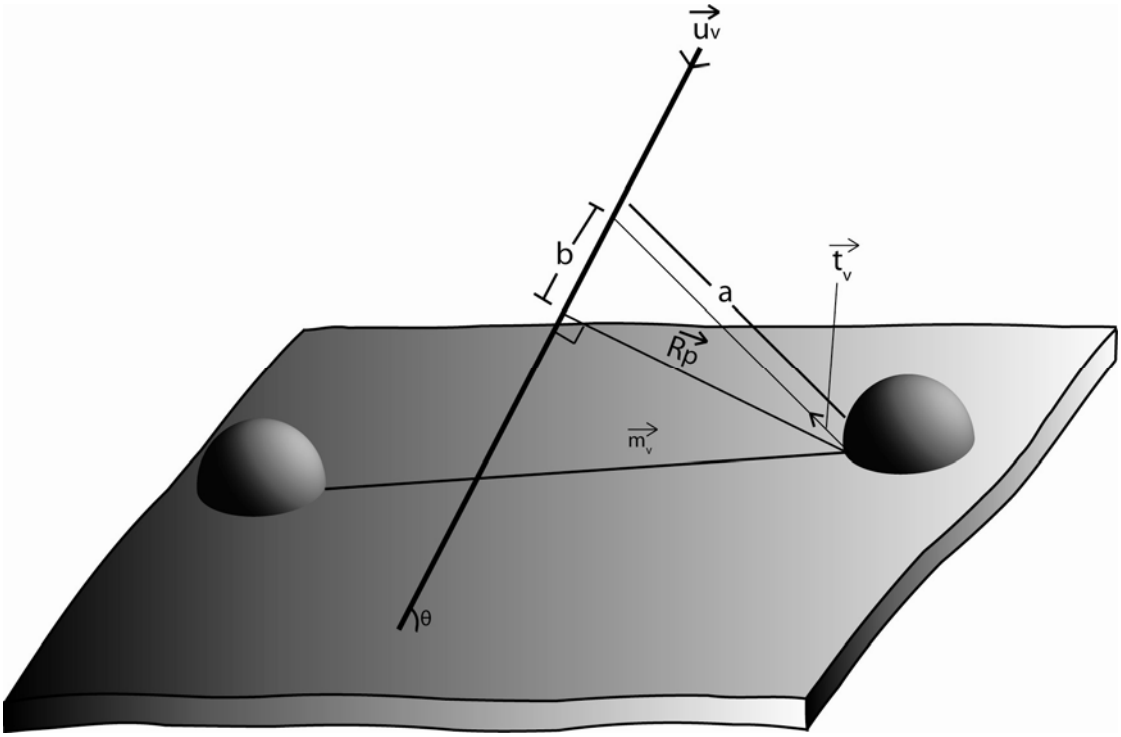

Figure 13: Vector diagram for speed reconstruction. Here $\overrightarrow{u_v}$ is the unit vector pointing in the direction of the shower, $\overrightarrow{m_v}$ is the vector from the HiRes coordinate system center to the mirror containing the triggered tube, $\overrightarrow{R_p}$ is a vector from the center of the detector site that intersects the shower axis at a 90 degree angle, $\overrightarrow{t_v}$ is a vector pointing in the direction of the line of site of the triggered tube, a is the distance to the shower, and b is the distance from a reference point defined by $\overrightarrow{R_p}$ and the line of site of the tube.

The closest point of approach between these two lines can be found by minimizing Equation 33 simultaneously with respect to the parameters a and b. This can be done using the standard method of taking the derivative of Equation 33 and setting it equal to zero as shown in Equation 34.

$$R^2 = |\vec{r} - \vec{s}|^2 \tag{33}$$

$$\frac{\partial R^2}{\partial a} = 0 \, , \frac{\partial R^2}{\partial b} = 0 \tag{34}$$

This calculation results in Equations 35 and 36. The Equations 37a through 37g define values used to simplify the form of Equation 35 and 36.

$$b = \frac{-2DC+FB}{F^2-4CE} \tag{35}$$

$$a = \frac{-Fb-B}{2C} \tag{36}$$

$Where$:

$$B = 2\left(\overrightarrow{-m_v} \cdot \overrightarrow{u_v} + \overrightarrow{r_p} \cdot \overrightarrow{u_v}\right) \tag{37a}$$

$$C = \left(\overrightarrow{u_v} \cdot \overrightarrow{u_v}\right) \tag{37b}$$

$$D = 2\left(-\overrightarrow{r_p} \cdot \overrightarrow{t_v} + \overrightarrow{m_v} \cdot \overrightarrow{t_v}\right) \tag{37c}$$

$$E = \overrightarrow{t_v} \cdot \overrightarrow{t_v} \tag{37d}$$

$$F = -2\left(\overrightarrow{t_v} \cdot \overrightarrow{u_v}\right) \tag{37e}$$

As discussed in the above technical note, each mirror vector $\overrightarrow{m_v}$ is given as a distance measured from the HiRes coordinate system center. The $\overrightarrow{r_p}$ vector is given from

the center of each detector. Once again, as a technical note for collaborators, the surveyed center locations of HiRes 1 and HiRes 2 were not stored in the geometry banks of the data files. Instead, for both reconstruction and Monte Carlo, the center of each detector was calculated by using the average of the mirror positions. For consistency, this process was followed in this analysis as well.

Once both the distance along the shower from $\overrightarrow{r_p}$ and the distance from the detector to the shower are known, the next step is to correct the trigger time for the distance the light travelled in the atmosphere. While the trigger times are calculated differently for each detector, correcting for the distance light traveled from the shower to the detector is done using the same calculation.

The corrected time is given by Equation 38.

$$t_c = t_t - \frac{a}{c_{air}} \tag{38}$$

In this equation, t_t is the trigger time reported by the tube, a is the distance to the shower calculated in Equation 36, and c_{air} is the speed of light in air. The difference between the speed of light in a vacuum and the speed of light in air is negligible for the calculation done here, so the speed of light in a vacuum was used.

Calculating the Speed

Once the time and distance are calculated, a point can be formed from each tube with the form (b, t_c). A linear least χ^2 fit is then performed on the set of points calculated for each detector. This resulted in independent speeds for HiRes 1 and HiRes 2. To

improve the fit, each point is weighted according to the number of photoelectrons the corresponding tube recorded. Showers have a finite width and, depending on their distance and trajectory, may cross multiple tubes. For showers that are several tubes wide, this assignment of weight gives tubes near the center of the shower the most weight. For showers at extreme angles, this assignment reduces the possible bias for showers that cross only the edge of a tube. In both cases, the end result is that tubes nearest the shower axis receive the largest weight in the least χ^2 fit.

In order to reduce the number of noise tubes in the fit, a recursive fitting procedure is followed. The orthogonal distance, from each point to the resulting fitted line, is calculated using Equation 39 (see Appendix B).

$$\delta_i = \sqrt{\frac{(s_0 + mt_i - b_i)^2}{1 + m^2}} \tag{39}$$

Here, s_0 and m represent the intercept and slope respectively found by the least $\chi 2$ fit and δ_i represents the distance from the i^{th} point to the line found by the least χ^2 fit. Once this distance is calculated, the mean and standard deviation for the set of distances are calculated. The number of standard deviations from the mean is calculated for each point. Points that are greater than 5 standard deviations from the axis are rejected as being noise tubes. The χ^2 fit is performed again and this process repeated until no new tubes are rejected.

This process results in a propagation speed m for each shower. These are subjected to a process of data selection and statistical analysis. The actual processing is described in the following chapter. Data selection criteria are explained in Chapter VIII.

CHAPTER VII

PROCESS

Preprocessing

Data were processed in several stages. First, the events were reconstructed as described in CHAPTER V. A set of scripts scanned the resulting reconstructed data and created a list of data files for each individual night with possible shower candidates. To ensure quality of data, these scripts only included data from December of 1999 until November of 2005. This period of time marks the epoch in which stereo data with calibration began to be recorded.

All together, 6304 data files including ~50,000 events were selected from 775 days that the detector ran during this period for further processing. Once the list was generated, a series of scripts then ran each in turn through the process described in the preceding chapter. The bulk of computational analysis was contained in a program called *shower_speed*. The remainder of this chapter details the computational steps and statistics performed during processing.

Shower_Speed

The *shower_speed* program was designed to perform the computational analysis. Processing was divided into smaller steps corresponding to specific types of calculations.

Each step will be discussed only briefly to cover relevant calculations and general operation. The options given to the program at run time determined which of the steps would be run. A brief list of options is given in Table 5 for the benefit of collaborators.

Input

The first step was to read in reconstructed data from a given data file and determine the type of data present. HiRes data were separated out into individual binary files. Each file contains a set of events recorded on a given day. It was common for each day to have multiple data files. Each event is made up of a set of banks. A bank generally corresponded to a specific stage of processing or subset of stored data.

As different analysis programs often shared the same set of data files, it is important to note the function of certain banks that were required for processing. This

Table 5: Options for shower_speed.run for the benefit of collaborators

Option	Example Usage	Purpose
-f	-f filelist.txt	Read in a file with a list of dst files to process.
-o	-o output.dst	If present, all events that failed any cut were output in dst format for review.
-c	-c cuts.txt	Specified an input file for user specified cuts.
-a	-a abnormal.dst	Specified outputting of abnormal events and the file to output to.
-p	-p planeout.dst 2222	Specified use of plane rotation routine. The first argument was a file name. The second a set of codes that described possible plane rotations to perform. It is of the form ABCD where A is hr1phi, B hr2phi, C hr1theta, D hr2theta and each could be a 0,1, or 2 where 0 meant do nothing, 1 meant output only final plane, and 2 meant output all steps.
-d	-d	When this option was specified, the mirror number, each tube, and matching time were dumped to a text file for each event. Text files were named m<event_number>.slopefile
-n	-n	When specified, the NPE for each tube and shower depth were dumped to a text file for each event. Text files were named m<event_number>.npefile
-q	-q	This option specified assuming set flasher geometry.

is provided in Table 6 for the benefit of collaborators. A brief description of each bank used is included, also for the benefit of collaborators.

Upon reading, events were sorted according to the types of available banks. If all necessary banks were present, then information was read in to a *shower* class designed to hold information throughout the entire processing cycle. In this chapter, this class is just referred to as the shower. If necessary banks were missing, events were removed from further processing. In general, an absent bank simply signified that the event in question had not passed minimum criteria for reconstruction at the stage where that bank was filled. For example, if plane fitting failed, the bank *hctim* would not be present.

The *fmc1* and *fmc2* banks were created for all showers generated by Monte Carlo(MC) and filled with the thrown shower information. If the *fmc1* and *fmc2* banks were filled, the bank was flagged as Monte Carlo(MC) for further processing and a shower created with the MC information. The *hctim* bank was created during stereo geometry determination. If the *hctim* bank was present, a shower was created with reconstructed information.

Table 6: Banks required for processing

Bank name	Bank Purpose
fmc1	Contains stereo MC information generated for HiRes 1
fmc2	Contains stereo MC information generated for HiRes 2
hctim	Contains reconstructed information from hr_process
fpho1	Contains reconstructed npe information for HiRes 2
hraw1	Contains raw npe information for HiRes 1

Independent MC and reconstructed showers were created for Monte Carlo data. The MC showers contained the geometry information recorded in *fmc1* and *fmc2*. The reconstructed shower used the geometry determined in the reconstruction process for the same shower stored in *hctim*. If *fmc1* and *fmc2* were not present, only one shower was filled. Once the showers were read in, the method of processing was identical.

For each type of event, data were read from the banks listed in Table 6. A list of what information was used and which banks from which this information was pulled is given in Table 7 for the benefit of collaborators. A special check was made to see if flasher geometry should be used. To test response to certain weather conditions, flasher geometry was set manually according to survey results. The flashers were then sorted according to which mirror and tube they appeared in.

Time Correction

Once the data were read in, the first calculation done was the correction of tube trigger times. The process was described in the preceding chapter. Several additional steps were involved in actual implementation. Because the $\overrightarrow{R_p}$ vector stored in each bank was relative to the center of each detector, the first step in this process was to transform the vectors involved from the HiRes coordinate system into a coordinate system specified by the center of each detector. This was done with Equation 40.

$$\overrightarrow{R_{p_{new}}} = \overrightarrow{R_p} + \overrightarrow{HR_{cen}} \tag{40}$$

Table 7: Banks used to set variables

Variable	Reconstructed Bank	MC Bank	Information
localsite_hr1	geoh	geoh	Average of all HR1 mirror positions. Represents center of HR1 in the HiRes coordinate system.
localsite_hr2	geohr2	geohr2	Average of all HR2 mirror positions. Represents center of HR2 in the HiRes coordinate system.
rp_hr1	hctim	fmc1	The Rp vector for HiRes 1
rp_hr2	hctim	fmc2	The Rp vector for HiRes 2
uv_hr1, uv_hr2	hctim	fmc1, fmc2	The unit vector in direction of shower. The two different variables indicate different plane fits.
mshwn_hr1	hctim	fmc1	The normal vector to the shower plane for the HR1 plane
mshwn_hr2	hctim	fmc2	The normal vector to the shower plane for the HR2 plane
hr1_jday, hr1_jsec, hr1_msec	hctim	not used	This is the Julian time of the event for HiRes 1 split into day, seconds, and milliseconds.
hr2_jday, hr2_jsec, hr2_msec	hctim	not used	This is the Julian time of the event for HiRes 2 split into day, seconds, and milliseconds.
hr1psi, hr1phi, hr1theta	hctim	fmc1	The psi, phi, and theta angles for HR1 calculated with stereo geometry.
hr2psi, hr2phi, hr2theta	hctim	fmc2	The psi, phi, and theta angles for HR2 calculated with stereo geometry.
good	hctim	all set good	A flag for each individual tube indicating whether or not the tube was used in stereo reconstruction
mirror_number	hctim	all set good	The mirror number for a given tube in the event
tube_number	hctim	fmc1, fmc2	The tube number for a given tube in the event
tv	geoh, geohr2	fmc1, fmc2	The pointing direction of the tube given by mirror_number and tube_number. Bank was chosen based on site
s_time	hctim	fmc1, fmc2	The time in nanoseconds of tube trigger
npe	fpho1, hraw1	fmc1, fmc2	The number of npe for a given tube. For HR1 this came from hraw1 and was not corrected for mirror gain. For HR2 this came from fpho1 and was only partially gain corrected. In both cases, it was used only as a relative measure.

Here, $\overrightarrow{R_p}$ was the vector read from the data banks, and $\overrightarrow{HR_{cen}}$ a vector from the HiRes origin to the calculated center of each detector. Once the transformation was accomplished, the distance was determined as described in Chapter VI. In addition to the calculations detailed in Chapter VI, one other calculation was made at this stage of processing.

Each tube in HiRes looks at approximately one degree of sky, so the shift from the center to the edge of the tube was approximately half a degree. To estimate possible error in the distance due to resolution, all tube vectors were shifted by a half degree from the pointing direction of the center of the tube. The distance was then recalculated using the shifted vector. The difference between this recalculated distance and the original distance was kept as an error estimate to be used later in the calculation.

Basic Calculations

At this stage of processing, several values of interest were calculated. First, the opening angle was calculated using Equation 41.

$$\theta_{opening} = \cos^{-1} \frac{\overrightarrow{n_{hr1}} \cdot \overrightarrow{n_{hr2}}}{|\overrightarrow{n_{hr1}}| * |\overrightarrow{n_{hr2}}|} \tag{41}$$

Here, $\overrightarrow{n_{hr1}}$ and $\overrightarrow{n_{hr2}}$ are vectors normal to the shower detector plane, and the factors on the bottom were to shift both normal vectors into unit vectors. The length of the observed track was calculated for both HiRes 1 and HiRes 2 in both degrees and meters by finding the tubes furthest along the track in either direction and applying the appropriate arithmetic. The duration of the shower in the HiRes 2 detector was calculated in a similar manner.

Speed Determination and Iterative Fit

The resulting pairs of speeds and times were fit as described in Chapter VI. The calculated slope (speed), the primary observable of interest in this study, was stored along with the intercept and covariance matrix from the fit for further processing. At this stage, χ^2 per degree of freedom was calculated for the least χ^2 fit. While χ^2 per degree of freedom serves as a useful indicator of problems in any given fit, it was not as useful as a determination of error in the entire data set. Each individual least χ^2 fit represented only the uncertainty in the fit itself. Many different factors, for instance, a poorly fitted shower trajectory, could cause a fit to return a speed different from that of the shower. Because of this, when looking at the entire data set it did not serve as a useful gauge for the accuracy of the propagation speed measurement.

Instead, in order to estimate the possible effects of various physical constraints of the detector, such as pixel resolution, timing resolution, and uncertainty in the condition of the atmosphere due to weather, a bootstrap method was used.

In the bootstrap method, the total number of good tubes in the shower was recorded. A new shower was created with all of the parameters of the old shower, but no matching tubes. Tubes were then selected at random from the original shower and used to fill the new shower. This was repeated until the new shower had an equal number of good tubes that the original shower had. During random selection, tubes could be selected multiple times and there was no requirement that a given tube needed to be selected at all. The new shower was then fit using the weighted χ^2 fit. The resulting speed for the new shower was recorded. The new shower was emptied, and then the random selection process repeated.

This cycle was repeated a number of times. During testing, the exact number of times this cycle was repeated was changed from a few to several thousand. After roughly 100 repetitions, the statistical improvement gained by increasing repetitions is in general less than the significance of the speed calculated. However, the increase in processing time required for increased accuracy was significant. To balance statistical significance and processing time, cycles of 100 repetitions were chosen.

After the bootstrap error had been calculated, the standard deviation and mean for the set of slopes were computed. The standard deviation from the bootstrap method was then used as an estimated error for the slope. The number of tubes in each mirror was counted and the maximum number of good tubes and triggered tubes recorded for later cuts. If output flags were specified at runtime, all statistical information calculated was output in text format for import into analysis programs. As a note to collaborators reviewing the processed data, the files containing statistical information were labeled as .origin files (in reference to statistical analysis software being used). Integrated signal for each phototube and shower timing information files were also output if specified by the user and labeled .slope files.

Event Cuts

At this point in processing, the first stage of event selection was done. The data selection process will be discussed at length in Chapter VII. Events were output according to options specified at run time.

Postprocessing

After the shower_speed program had run, a set of files corresponding to anomalous events was output. As will be described in far more detail in the succeeding

chapters, a set of MC events was generated and used as a basis for determining what an anomalous event was. An event is deemed anomalous if it is more than 3 standard deviations from c, where the standard deviation was calculated with a standard Gaussian fit to the resulting distribution.

These events were each examined individually to determine possible causes for the anomalous speed. Even with aggressive data selection requirements, it was possible for events that had problems in reconstruction to make it to this stage. Examples of these problems include incorrect fitting of the planes and noise events with just enough spatial correlation to make it through processing but without enough physical form to separate them from noise. While all events flagged as anomalous were kept for reference, events in which there were obvious problems with reconstruction were not processed further. This determination was made by visual inspection (as a last resort) as described in Chapter XI.

A series of postprocessing data selection cuts were then applied to the resulting set. This included events that fell on bad weather days. A cut was also applied to the normalized difference (the ratio of the difference between HiRes 1 and HiRes 2 in speeds to the estimated error). The speeds from the two sites were observed to be correlated due to the common geometry used in determining the plane intersection. This is shown in Figure 14. Because all speeds are necessary to calculate the correlation, this cut could

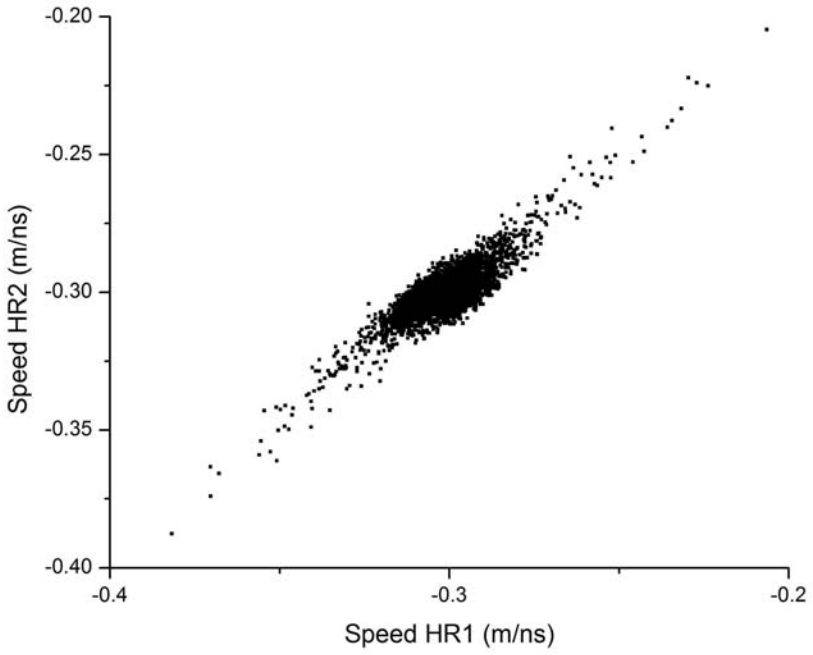

Figure 14: HiRes 2 speed vs. HiRes 1 speed

not be performed until after the entire set was processed. The ratio and covariance factor where then calculated as shown in Equations 42 through 43.

$$\partial_n = \frac{m_{HR1} - m_{HR2}}{\sqrt{(\sigma^2_{HR1} + \sigma^2_{HR2}) + 2 * Cov(\sigma^2_{HR1}, \sigma^2_{HR2})}} \tag{42}$$

$$Cov(\sigma^2_{HR1}, \sigma^2_{HR2}) = \frac{1}{n-1}\sum_{=1}^{n}(x_i - \bar{x})\,(y_i - \bar{y}) \tag{43}$$

All events with a ∂_n greater than 10 were cut from further consideration. At this point, individual events were examined to see if their speed could be brought back into standard ranges without altering the signal the detector recorded. This was done by rotating the shower detector planes from each site around different axis until the speed was at the speed of light, then comparing the newly rotated shower detector planes to the triggered tubes. This process is described in more detail in Appendix A and in Chapter IX. The results will be discussed after data selection criteria have been covered.

CHAPTER VIII

DATA SELECTION

Motivation

The primary goal of this study was to search for possible candidates for showers induced by "exotic" primary particles in the HiRes data set. Assuming that the bulk of events are associated with ordinary hadronic matter as is assumed by the composition measurement [12], this problem reduces to that of searching for a small number of possible outliers in a large, regular data set. Ideally, any event that reconstructed with a speed different from *c* would be a possible candidate. In practice, our measurements have finite resolution and not every event is reconstructed correctly. The latter adds "tails" to the distribution of measured shower speeds.

Because of the size of the HiRes data set, it is impractical to review each event that falls into one of these tails individually to determine if it is a candidate. An automated algorithm was used to measure the shower speeds. Thus, a great deal of effort was put into simulation studies aimed at finding possible causes for poorly reconstructed events and devising algorithms for removing these from the data set without reference to the Monte Carlo "cheat" [1]information. The goal of each individual filter is to remove as

[1] "Cheat" information refers to information available in Monte Carlo simulations that would not be available for real data. For example, the shower geometry is determined when a Monte Carlo shower is generated, but must be calculated for real data.

many poorly reconstructed events as possible while minimizing the probability of removing "real" exotic candidates.

This process of refining the data set can lead to biases in final results if not done carefully. To avoid "tuning" cuts to the real data, nearly all of the work done to select cuts was completed using only Monte Carlo events. Most of this work was done before any real data were analyzed. When cuts needed to be revised after real data had been analyzed, the same steps used to determine the initial cuts was repeated with only Monte Carlo data run through the updated process.

This chapter describes the steps used to determine cuts. It includes a detailed account of each filter used.

Data Set Used to Determine Cuts

Several sets of Monte Carlo simulations were generated as part of this study. A very large set (~50000) of showers that corresponds to the actual measured stereo spectrum from HiRes was used to set the event selection cuts. This was done on the assumption that essentially all data events are of ordinary hadronic (and mostly light) nuclear composition. These showers were generated with the propagation speed set to the canonical value of $c = 0.299\ {}^{m}/_{ns}$. These simulated events were subjected to the same reconstructed code as the real data and run through the slope (propagation speed) fitting procedure described in Chapter VI.

Figure 15 and Figure 16 show the distribution of the fitted speeds for HiRes 1 and HiRes 2 respectively. For these plots, the known input geometry of the shower is used to determine the distance along the track. However instead of thrown times, the simulated tube times measured by the detector were used. The sharply peaked distribution with

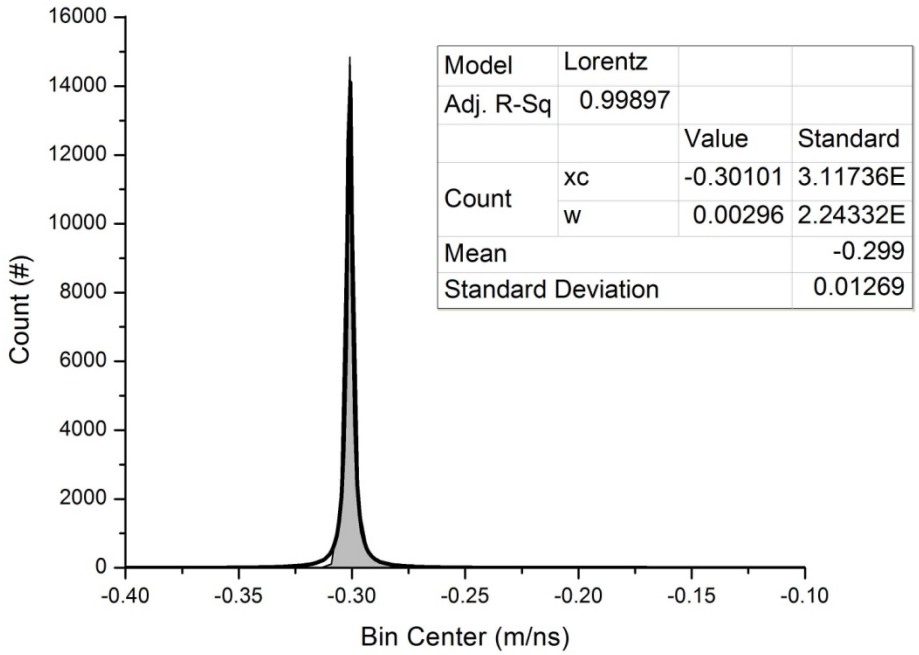

Figure 15: Binned count vs. Speed for thrown geometry for HiRes 1 with Lorentz fit

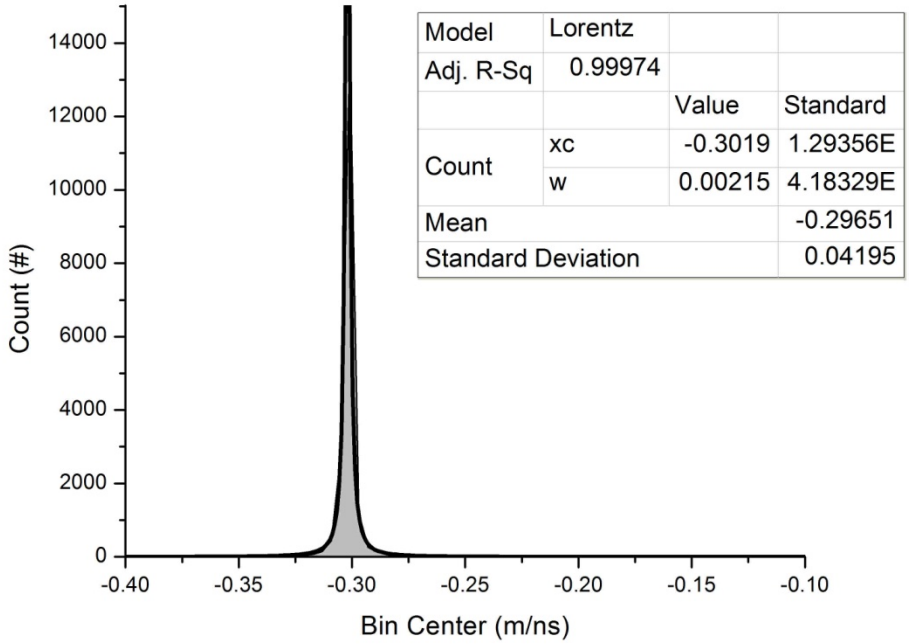

Figure 16: Binned count vs. Speed for thrown geometry for HiRes 2 with Lorentz fit

full width at half max (FWHM) of 0.003 m/ns (~1% of speed of light) and 0.002 m/ns (~0.7% of speed of light), respectively, for HiRes 1 and HiRes 2. The distributions in each case are clearly compatible with the generated propagation speed of -0.299 m/ns (the negative sign indicating downward moving showers). The width of each peak can be attributed to the small uncertainty in geometry caused by tubes having a one degree field of view. Because events are fitted with as few as 6 pixels, the least χ^2 fit result can vary slightly around the actual speed of the shower even using known geometry. These plots serve to validate the slope fitting procedure that is central to this analysis.

It is worth noting that while HiRes 2 provides a more sharply peaked distribution, the RMS of HiRes 2 is actually greater than that of HiRes 1. This is a result of the different electronics used. Both sets of electronics are subject to noise. As mentioned when discussing the fitting procedure, points are fitted according to the integrated signal in the tube. This generally results in the tubes near the center of the event having the most weight. Noise tubes near the end of the event skew the fit by forcing it to rotate around the weighted average given by the center tubes. A large amount of effort is made to remove noise tubes; however, not all noise tubes can be removed. As HiRes 2 views longer tracks, the effect is more pronounced. However, HiRes 2 also has better timing resolution due to the FADC electronics. This combination of factors leads to a sharper peak with longer tails than that given by the HiRes 1 data.

The fits to Lorentzian curves in this case were used primarily as a robust estimation for the FWHM, but not to represent the tails of the distribution. We use these FWHM values so determined to help compare various distributions. While fitting slightly better than either a double or single Gaussian, these fits still do not perfectly

mirror the distribution. Long tails at the end of each distribution fall outside the parameters given by the fits.

In order to test the effect of the event reconstruction on the data set, the same set of Monte Carlo events was then processed using the same reconstruction code used for real data. The results for the propagation speeds are shown in Figure 17 and Figure 18. Events shown here are the same ones used to create Figure 15 and Figure 16. For these plots, the reconstructed geometry from the process described in Chapter V was used for each event.

In Figure 17 and Figure 18, the peaks of the distributions are each still centered on the thrown speed of the showers. The FWHM of the HiRes 1 peak was calculated at .010 m/ns, and that of HiRes 2 was .0057 m/ns. This represents a three-fold increase for HiRes 1 and a two-fold increase for HiRes 2 compared to FWHM attained using the input geometry. Once again, the distributions have long non-Gaussian tails.

For the benefit of our collaborators, Table 8 shows a list with a brief explanation of various cut parameters that impact the overall accuracy of the shower speed measurement. A large number of variables were compared while looking for quantities that effected reconstruction. Where possible, data selection cuts were made to identify poorly reconstructed events. This was done to minimize the number of false anomalies caused by reconstruction errors.

A set of graphs and a brief discussion will follow for several of these variables. Of these, the opening angle $\theta_{\hat{n}\hat{n}}$, the θ and ψ angles from Figure 7, and σ_{boot} were

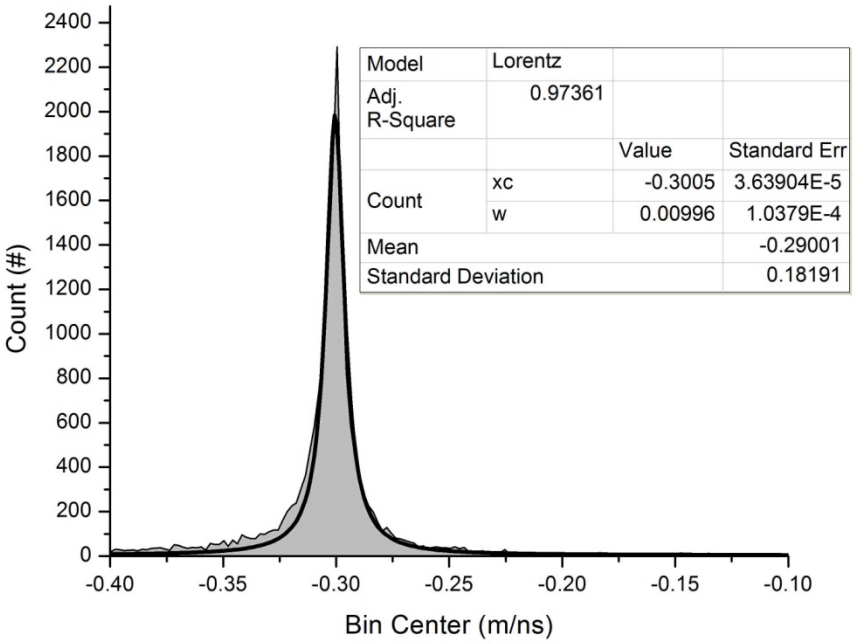

Figure 17: Binned Count vs. Speed for reconstructed geometry for HiRes 1 with Lorentz fit

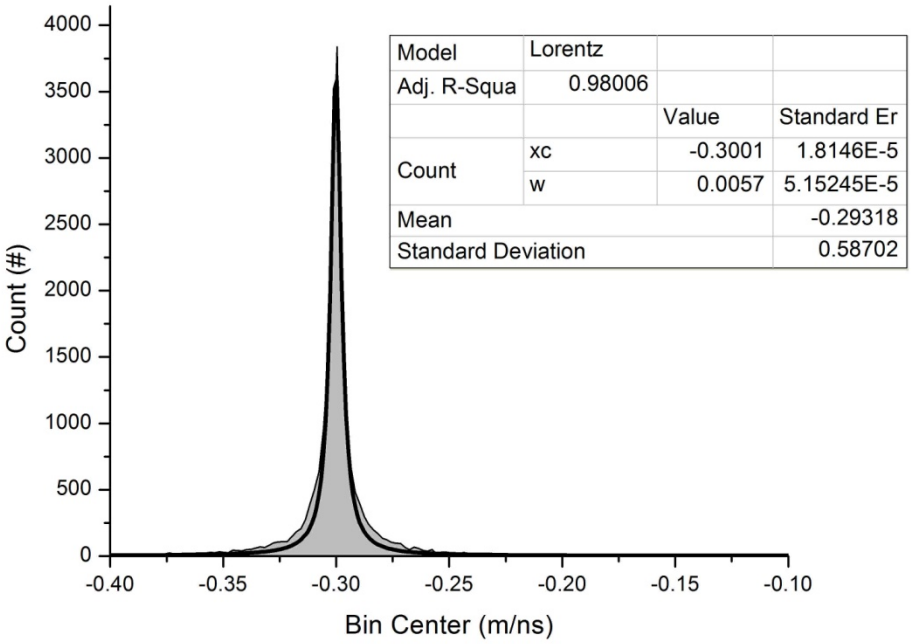

Figure 18: Binned Count vs. Speed for reconstructed geometry for HiRes 2 with Lorentz fit

Table 8: List of variables that had reconstructed speed compared to thrown speed

Variable Name	MC/Reconstructed	Description
r_viewfirst	MC	Distance to first point viewable by detector
r_viewlast	MC	Distance to last point viewable by detector
rp_true	MC	Thrown Rp
Rphr1	Reconstructed	Reconstructed Rp to HiRes 1
Rphr2	Reconstructed	Reconstructed Rp to HiRes 2
opening_angle	Reconstructed	Opening Angle between shower detector planes
mctlngth	MC	Thrown Track Length for HiRes 2 (degrees)
tlngth_hr1	Reconstructed	Reconstructed Track length for HiRes 1 (degrees)
tlngth_hr2	Reconstructed	Reconstructed Track length for HiRes 2 (degrees)
mctlngth m	MC	Thrown Track Length for HiRes 2 (meters)
tlngth_hr1m	Reconstructed	Track Length in Meters for HiRes 1
tlngth_hr2m	Reconstructed	Reconstructed Track Length for HiRes 2 (meters)
Chi2	Reconstructed	χ^2 Value for HiRes 2 fit
Chi2n	Reconstructed	χ^2 per degree of freedom for HiRes 2 fit
Psimc	MC	Thrown psi angle
Thetamc	MC	Thrown theta angle
Phimc	MC	Thrown phi angle
Energy	MC	Thrown Energy
shower_time	Reconstructed	Reconstructed time shower was in mirror view for HiRes 2
hr1shower_time	Reconstructed	Reconstructed time shower was in mirror view for HiRes 1
Hr1chi2	Reconstructed	χ^2 Value for HiRes 1 fit
Hr1chi2n	Reconstructed	χ^2 per degree of freedom for HiRes 1 fit
Hr1psi	Reconstructed	Reconstructed Psi angle as seen by HiRes 1
Hr1theta	Reconstructed	Reconstructed Theta angle as seen by HiRes 1
Hr1phi	Reconstructed	Reconstructed Phi angle as seen by HiRes 1
Hr2psi	Reconstructed	Reconstructed Psi angle as seen by HiRes 2
Hr2theta	Reconstructed	Reconstructed Theta angle as seen by HiRes 2
Hr2phi	Reconstructed	Reconstructed Phi angle as seen by HiRes 2
Hr1energy	Reconstructed	Reconstructed Energy using HiRes 1 fits
Hr1tubes	Reconstructed	Number of good tubes at HiRes 1
Hr2tubes	Reconstructed	Number of good tubes at HiRes 2
chi2pnmc	MC	χ^2 per degree of freedom for thrown geometry fit

chosen as the most efficient variables to use for event selection. The reasoning for determining the exact cut value for each will be included when discussing these variables.

Hardware Motivated Cuts

Before discussing the postprocessing cuts, it is useful to understand several hardware motivated cuts applied mostly during reconstruction. A number of cuts were applied during the reconstruction itself in order to eliminate as many events as possible that could not be accurately reconstructed. Those cuts are summarized in Chapter V in Table 3. In addition, a set of very loose quality (of the successful reconstruction) cuts was used.

First, the number of triggered phototubes present in a given event directly affects how accurately the SD planes can be determined. For stereo reconstruction, events were rejected if they had fewer than six good tubes at either site. Second, the procedure used to determine propagation speed used an iterative filter to remove noise tubes in an event. After this filter, the number of "good" tubes remaining in each event was again examined. Events with fewer than three good tubes in HiRes 1 or fewer than six good tubes in HiRes 2 were removed. Third, in order to eliminate correlated electronic or optical noise events, those events with more than 170 tubes in any single mirror were also removed.

Two more cuts were made on reconstructed geometries. The first removed events with reconstructed ψ angle in the SD plane (Figure 7) greater than 120 degrees at either site. These corresponded to events pointed at a detector where the light signal was dominated by direct Cherenkov light that would not give reliable propagation speeds from the tube timing. The second geometrical cut removed events with track lengths of

less than 8 degrees at either site. Such events generally included insufficient information to calculate the speed of the event with the process described in Chapter VI.

Finally, during processing, the logarithm of the probability that the correlated time-angle structure of the event could be accounted for from a coincidence of noise tubes modeled as a 2D random walk was calculated. The process for calculating this probability follows. Assuming vector $\vec{r}$ is the vector that results from a sum of N independent steps, then the probability density is given by the Rayleigh probability density shown by Equation 44.

$$p(r) = \frac{r}{\sigma^2} e^{-r^2/2\sigma^2} \tag{44}$$

For the HiRes mirrors, $\sigma = \frac{1}{2}\sqrt{N}$ where N is the number of time ordered pairs of adjacent triggered phototubes and the factor of 2 prevents double counting. The probability that a displacement of magnitude $r > R$ for a given vector of length R occurs is given by integrating this formula. Performing this operation and taking the log of both sides results in Equation 45.

$$plog = \log_{10} P\{r > R\} = \frac{R^2}{N \ln 10} \tag{45}$$

This value is referred to as *plog*. As a result of writing this in log base 10, the chance that a given event could occur from a random walk can be given as Equation 46.

$$Prob_{rw} = \frac{1}{10^{plog}} \tag{46}$$

This means that an event with a plog value of 2 has a 1% chance of corresponding to a random walk coincidence. The details of calculating the plog value are given

elsewhere[28]. For the purpose of this dissertation, events with a plog value of less than 2.0 were cut. This is the standard cut for nearly all HiRes studies.

Fitting Error

Figure 19 and Figure 20 show plots of the calculated shower speed versus the standard deviation, σ_{boot}, calculated using the bootstrap method described in the previous chapter for MC events. Because the σ_{boot} values fall extremely close together, the horizontal axis is displayed on a log scale to allow full view of the data. The resulting scatter plot shows that showers for which σ_{boot} is small are more likely to reconstruct near the correct thrown speed.

Also in the figure is a small section of events located at a shower speed of 0 m/ns that form almost a straight line above the distribution. This is just a result of the graphs including the entire data set without any cuts. These events are those where the fit failed.

Various events were examined one by one to see what caused the fitting error. A sample event is shown in Figure 21. This event demonstrates the most common cause for high sigma values. The event itself is spread out over a large number of tubes in the HiRes 2 display. While on average, using a weighted fit should give a plane near the actual center of the shower, such a wide distribution allows the plane to rotate almost freely over a one or two degree field of view. This makes the plane in individual events very difficult to calculate accurately.

As discussed in Chapter VII, σ_{boot} is a measure of how much the speed can fluctuate within the set of triggered phototubes. For wide events like the one shown in

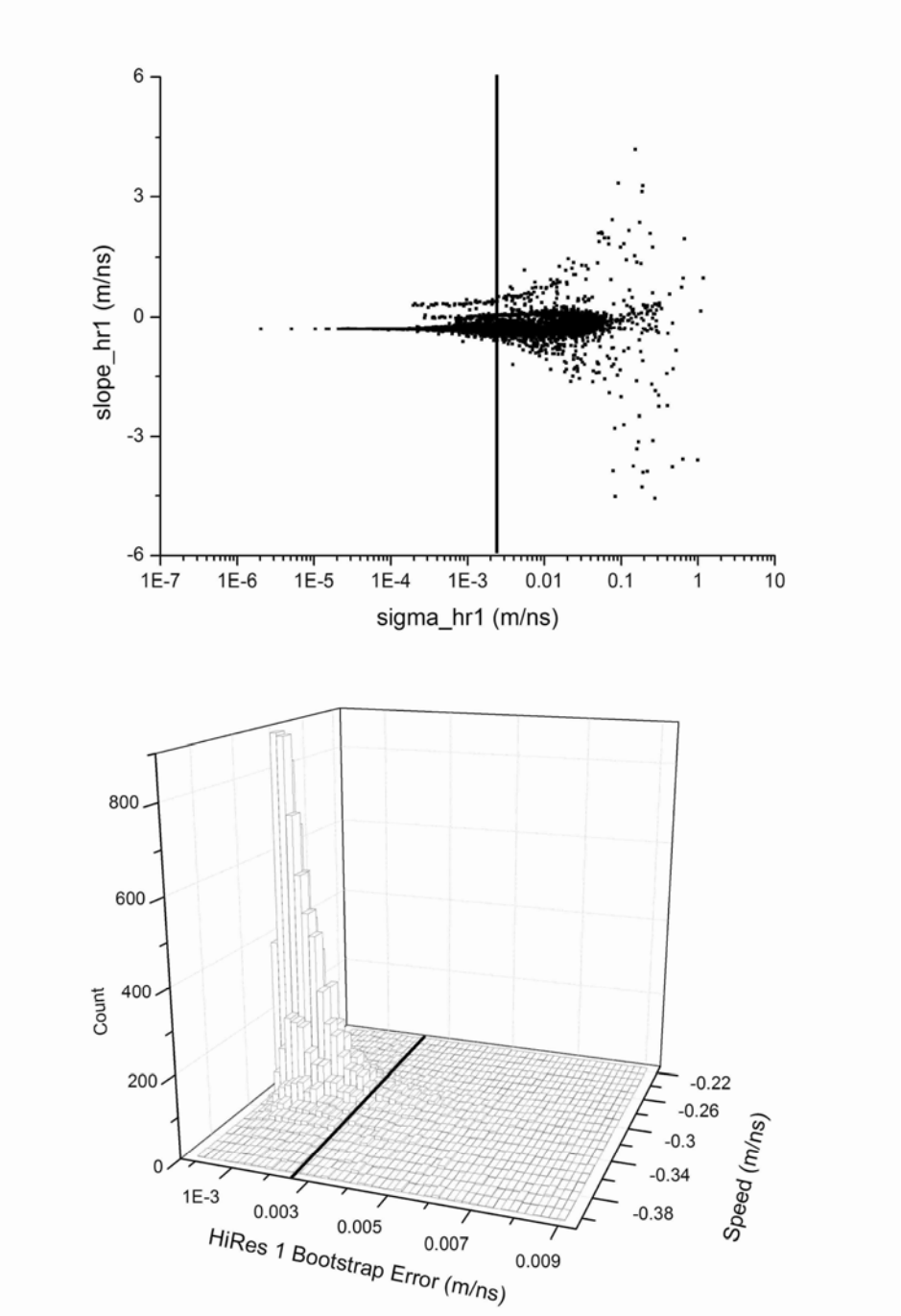

Figure 19: Top: Shower speed vs. standard deviation calculated with bootstrap method for HiRes 1. Line shows proposed cut (events to right of line removed). Bottom: Lego plot showing relative number of binned events. Line shows proposed cut. This data is all-inclusive. The small structure in the top plot centered near 0 speed are events whose geometry did not reconstruct.

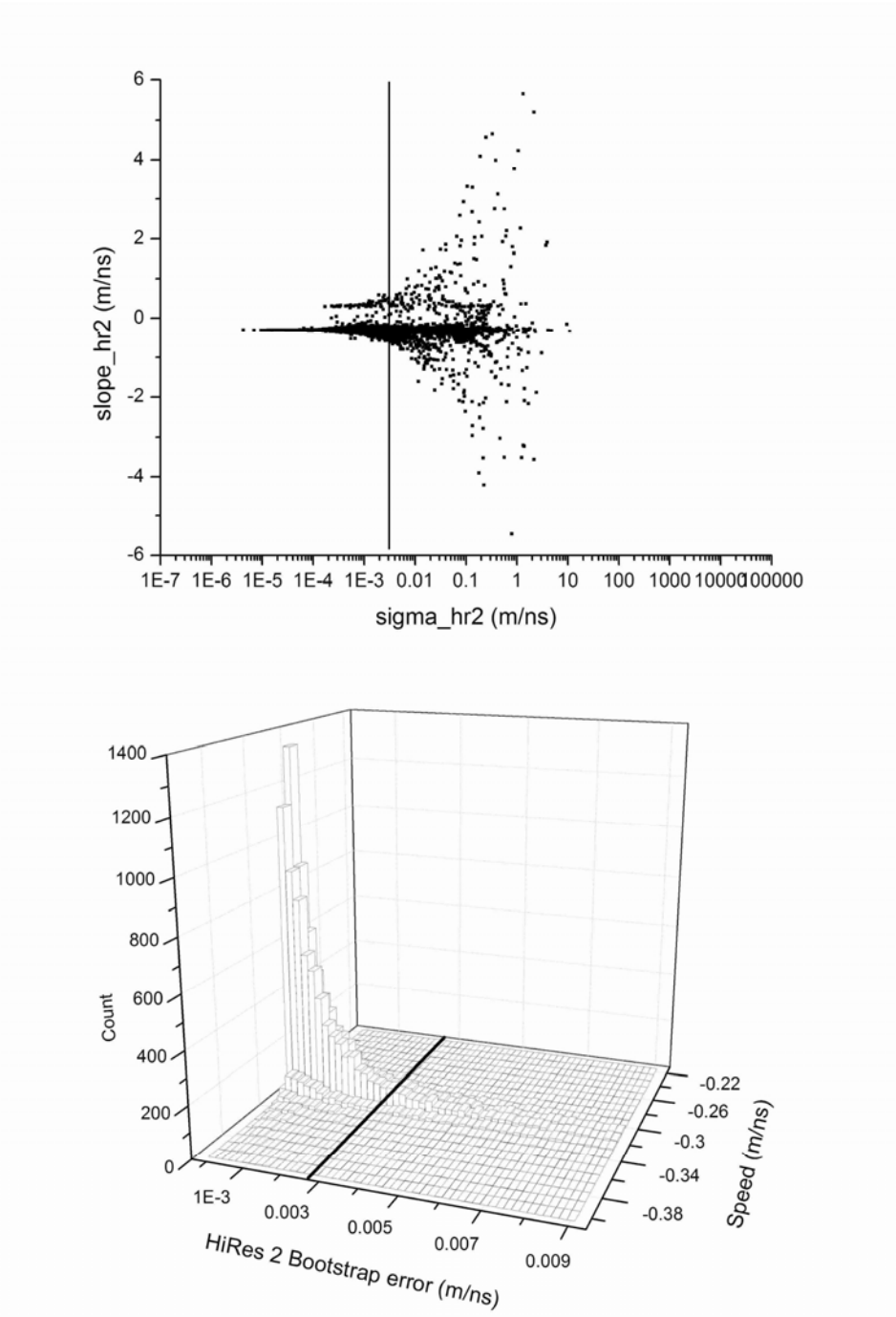

Figure 20: Shower speed vs standard deviation calculated with bootstrap method for HiRes 2. Line shows proposed cut (events to right of line removed). This data is all-inclusive. The small structure in the top plot centered near 0 speed consists of events whose geometry did not reconstruct.

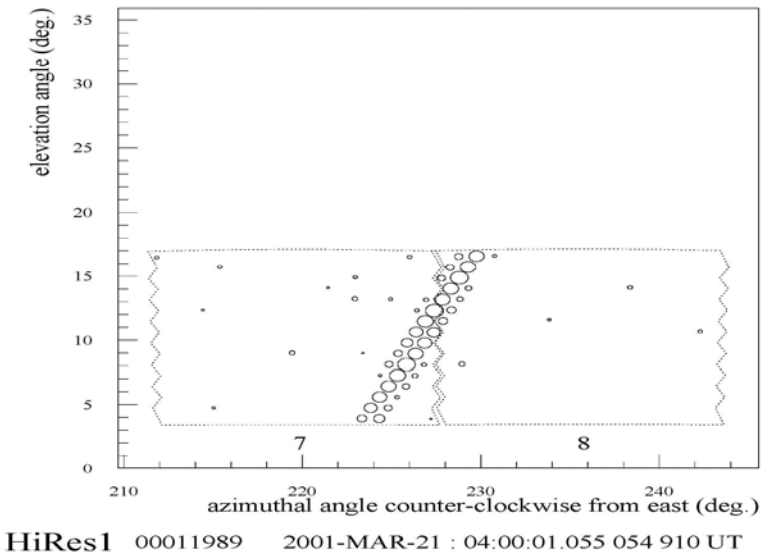

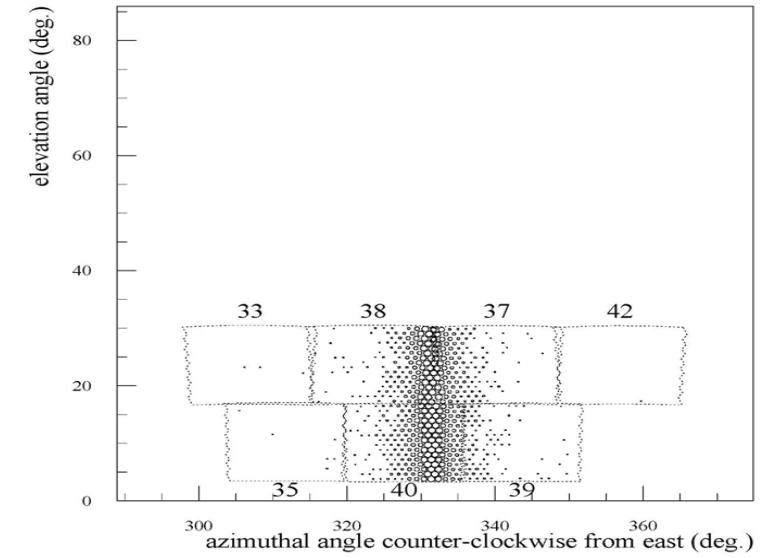

Figure 21: Sample MC event with high sigma_hr2

Figure 21, the actual phototubes used to determine the speed given a fixed geometry become very important. The fluctuations in speed caused by selecting just a subset of these tubes makes σ_{boot} a rough estimate of how much freedom a plane has to be rotated in a given event.

It is possible to remove the worst of these events with a cut on σ_{boot}. To determine the proper cut for σ_{boot}, different values were tried. For each value, the standard deviation and the fraction of events removed was then calculated. The results of this are shown in Figure 22 and Figure 23.

Looking at Figure 22, the RMS calculated from the set of speeds remaining after the cut is shown on the vertical axis of the lower graph. On the top plot, the vertical axis shows the fraction of events remaining after events with σ_{boot} values greater than the cut value are removed.

The RMS of the data set drops almost linearly over the entire range of the plot. Above a cut value of 0.002 m/ns, data are removed in an almost linear fashion as well. At 0.002 m/ns, a sharp increase in the amount of data removed with a tightened cut occurs. Roughly speaking, the portion of the plot above 0.002 m/ns corresponds to cutting events from the tail of the distribution. At 0.002 m/ns, events in the actual distribution begin to get cut; hence, the amount of data removed per cut increases dramatically.

The same behavior is seen when examining HiRes 1 in Figure 23. Once again, an almost linear decrease in the RMS is shown over almost the entire range of the graph. The break occurs at the same point, roughly 0.002 m/ns.

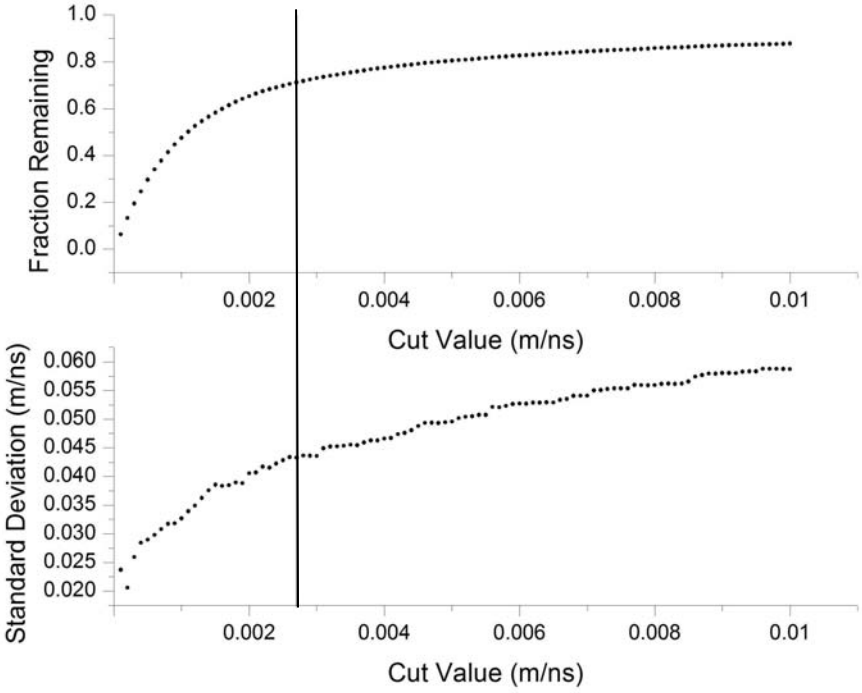

Figure 22: HiRes 2 plots for σ_{boot} cut

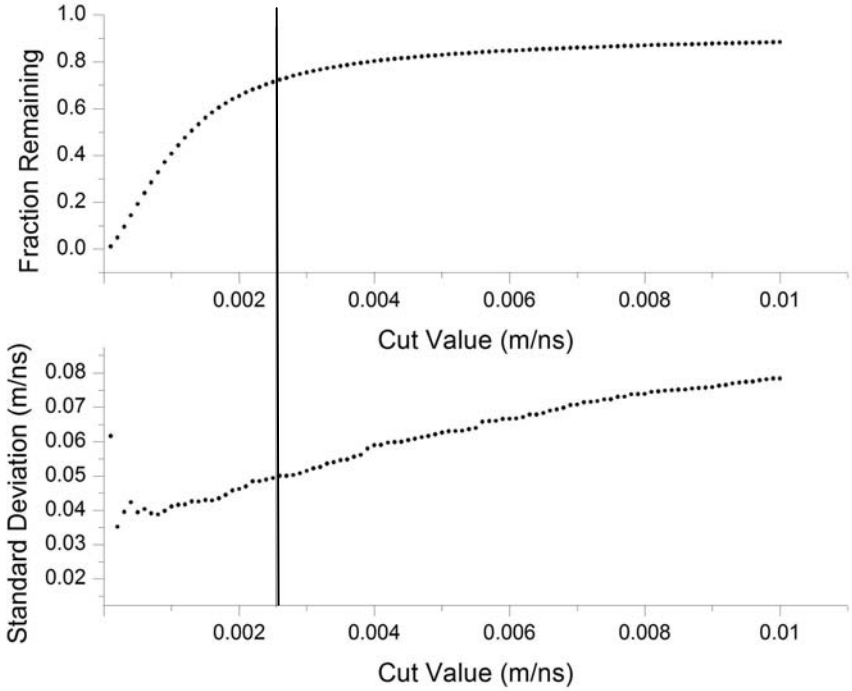

Figure 23: HiRes 1 plots for σ_{boot} cut. Line shows proposed cut.

This is a natural break point to use as an estimated starting point for the actual cut. The actual cut was selected by comparing the standard deviation to full width at half max (FWHM) of a standard Gaussian fit when combined with other cuts that were made. This will be discussed in further detail when combined cuts are considered.

$(\boldsymbol{R_p})_{min}$ Cut

As discussed previously, $\overrightarrow{\boldsymbol{R_p}}$ is a vector from the detector to the shower axis that intersects the shower at a 90 degree angle. The magnitude (R_p) of the $\overrightarrow{\boldsymbol{R_p}}$ vector is the minimal distance from the shower to the detector. As events are seen closer to the mirrors, several systematic errors can affect speed reconstruction. Some of this is seen while trying to fit events and is therefore taken care of by the σ_{boot} cut. However, other physical effects, like spherical aberration, parallax from the mirrors, or the actual lateral extent of the shower becoming increasingly large, become more pronounced the closer an event occurs to a mirror. It was important to see how these effects affected the determination of the shower speed. Figure 24 and Figure 25 show two plots dealing with the effect R_p has on shower speed at each detector.

The bottom plot shows the RMS calculated after the cut $R_p > (R_p)_{min}$ was made. The top plot shows the percentage of events left after this cut. In both plots, cutting on R_p actually makes the RMS of both HiRes 1 and HiRes 2 larger than leaving the data uncut. There does appear to be a small dip in the RMS of HiRes 2 at around 5 km, but this improvement is very small compared to the amount of data being removed by the cut.

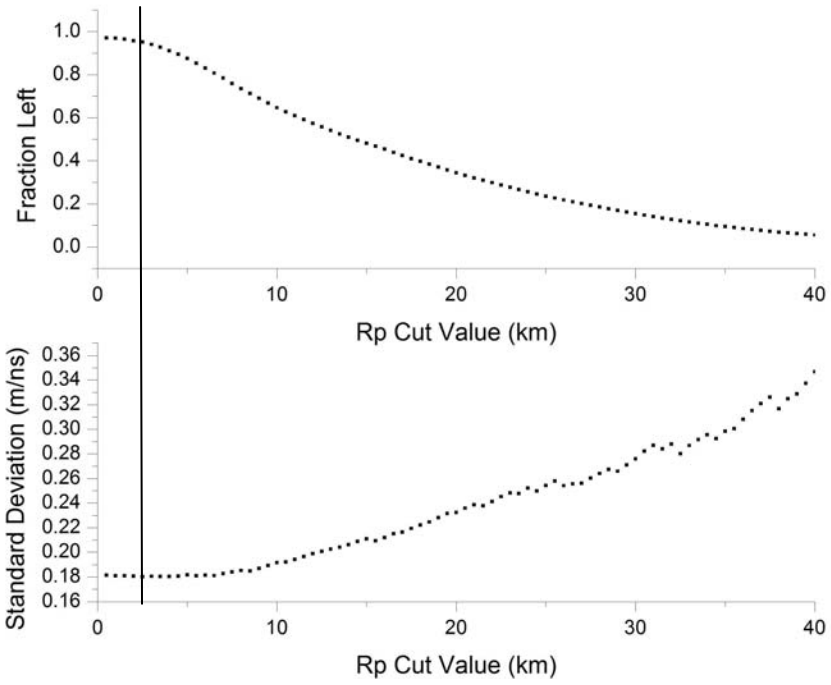

Figure 24 HiRes 1 Rp cut plots. Line shows proposed cut.

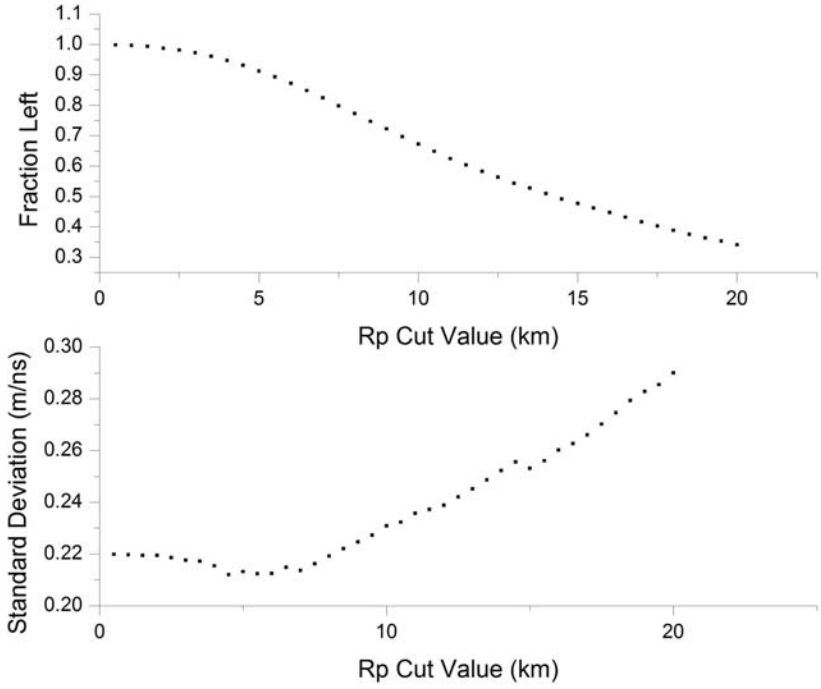

Figure 25: HiRes 2 Rp cut plots

From these graphs, there is no obvious point at which to cut on R_p. However, for reasons that will be discussed later in reference to the analysis of real data, a cut was made on R_p for HiRes 1. That cut was set at 2.5 km.

Opening Angle

Figure 26 shows a schematic diagram of two shower detector planes crossing. The opening angle is labeled α in the picture. If the shower were to fall in line with both detectors, the shower planes would be identical giving α or either 180 degrees or 0 degrees and the geometry could not be determined from crossing the planes alone. Theoretically, as long as the shower does not lie on this line, the geometry is precisely determined by plane crossing. In practice, however, the resolution of the detector is limited such that a wider area exists wherein geometry is poorly determined by plane crossing. By looking at the variation that opening angle causes on speed for showers thrown with a known speed,this effect can be examined.

Figure 27 shows the speed of HiRes 1 and HiRes 2 events plotted against opening angle in degrees. Figure 28 shows a binned versions of this plot. The reconstructed speed broadens for both detectors as the opening angle approaches the extremes. This effect corresponds to the uncertainty in geometry defined solely by plane intersection as detailed above. To determine the best location to cut on opening angle, a series of trial cuts in 1 degree steps were made. These cuts were a symmetric "bracket" cut such that a cut of n degree corresponded to removing events with an opening angle of less than n degrees or greater than 180-n degrees. As an example, a cut of 10 degrees would

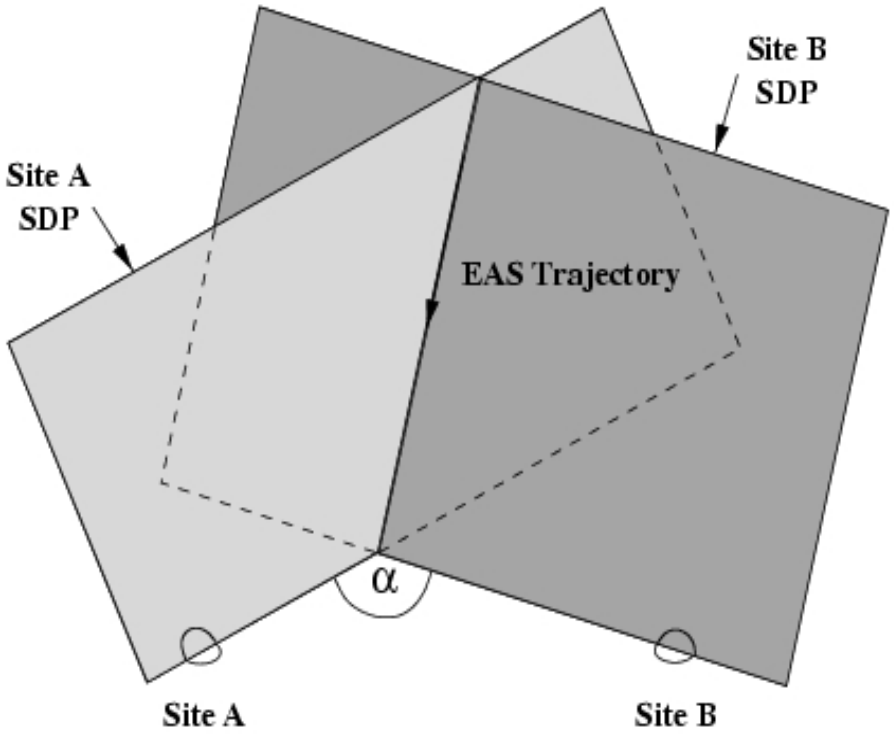

Figure 26 : Opening angle between shower detector planes

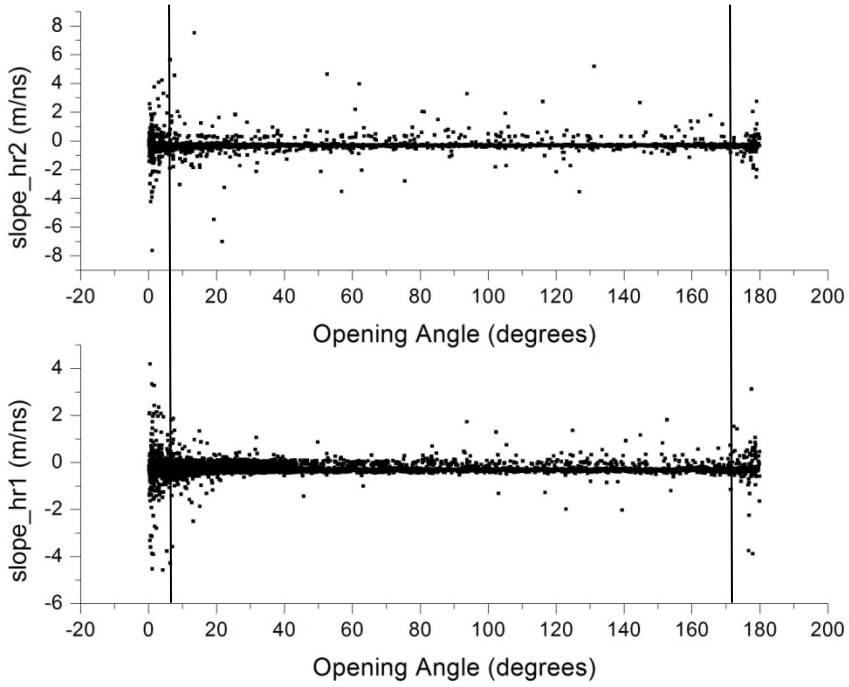

Figure 27: Opening angle cut plots. Line shows proposed cut (events between two lines kept).

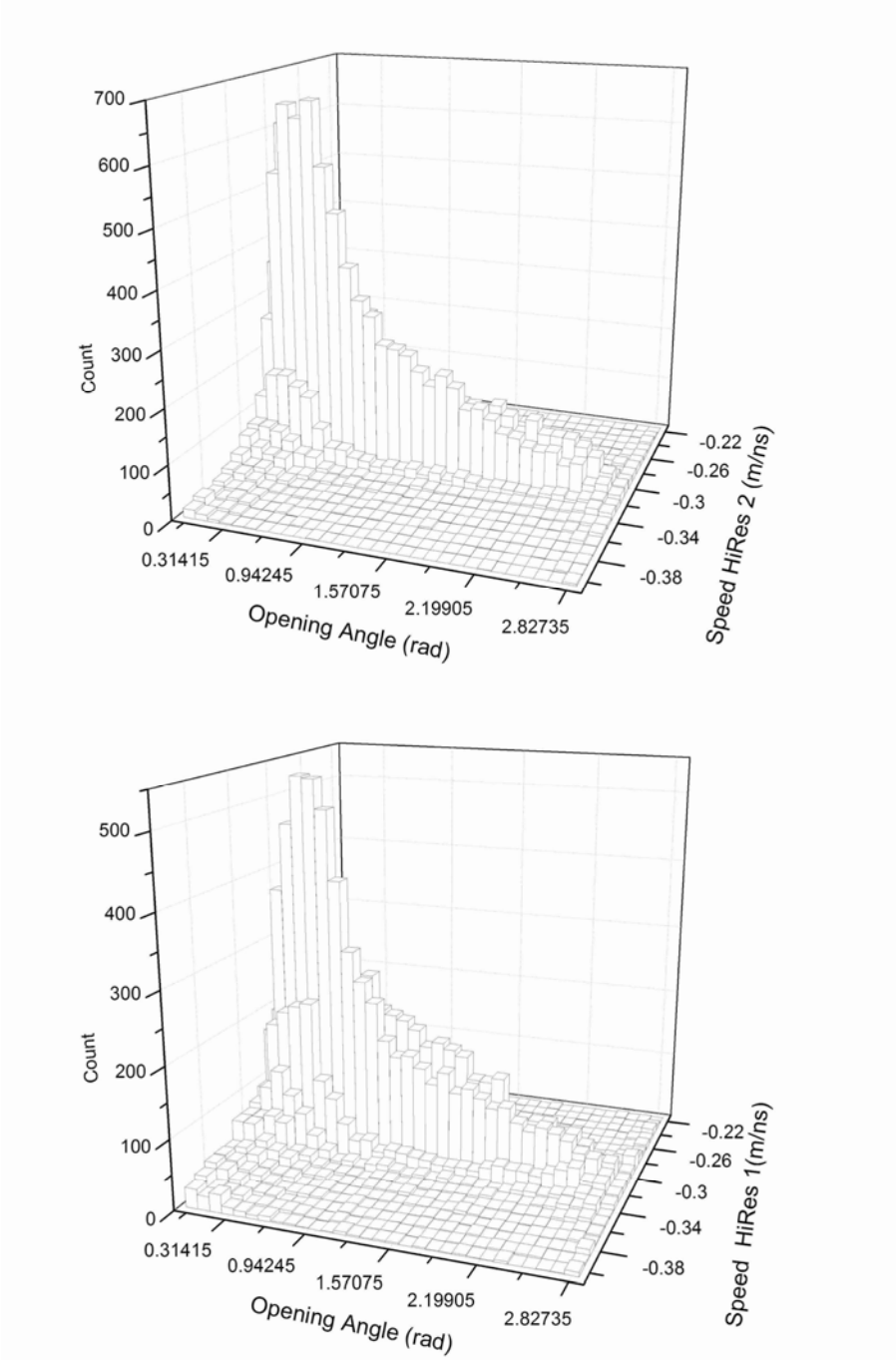

Figure 28: Plots showing opening angle vs. speed vs. binned count for HiRes 1 (bottom) and HiRes 2 (top).

correspond to removing events with an opening angle of less than 10 degrees or greater than 170 degrees.

After each cut was made, the standard deviation of the set of remaining shower speeds was calculated. Figure 29 shows the result for the HiRes 1 reconstructed speeds, and Figure 30 shows the results for HiRes 1 speeds. The bottom plot in both Figure 29 and Figure 30 show the RMS calculated after a cut of $Cut\ Angle < \theta_{\hat{n}\hat{n}} < (180 - Cut\ Angle)$. So a Cut Angle of 10° drops any shower with an angle of less than 10° and greater than 170 degrees. The top plot in both Figure 29 and Figure 30 shows the percentage of events left after that cut has been made.

As demonstrated by the plots, the RMS of the set of events remaining after the cut improves rapidly at first but then levels off. The "ladder" effect in Figure 30 is a result of cutting certain events with very large values that skew the RMS by a large amount. In both cases, the percentage of events remaining drops at an almost constant rate over the course of the range displayed. From these plots, a starting cut on opening angle of 10 degrees was chosen. As with other cuts, this was used only as a starting point. The exact cut will be discussed when looking at combined cuts.

Ψ Cut

Various angles calculated during reconstruction are shown in Figure 31. The ψ angle corresponds to the angle between the shower axis and the ground in the shower detector plane. As already discussed for hardware motivated cuts, this has a hard cut of 120 degrees dictated by Cherenkov light generated by the shower. Events moving at near horizontal are difficult to reconstruct properly. The ψ cut effectively cuts away events moving at near horizontal towards the detector.

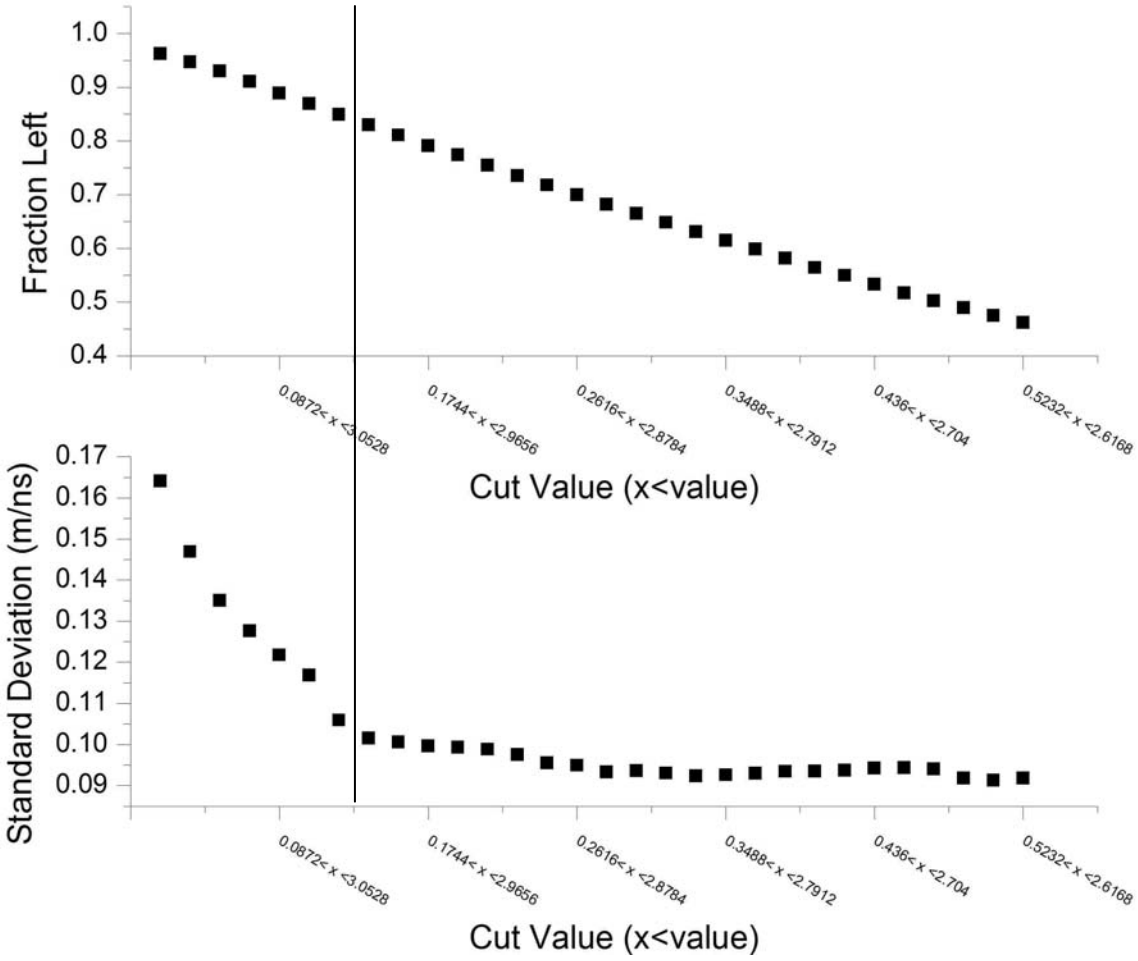

Figure 29: Opening angle cut comparison for HiRes 1. Line shows proposed cut.

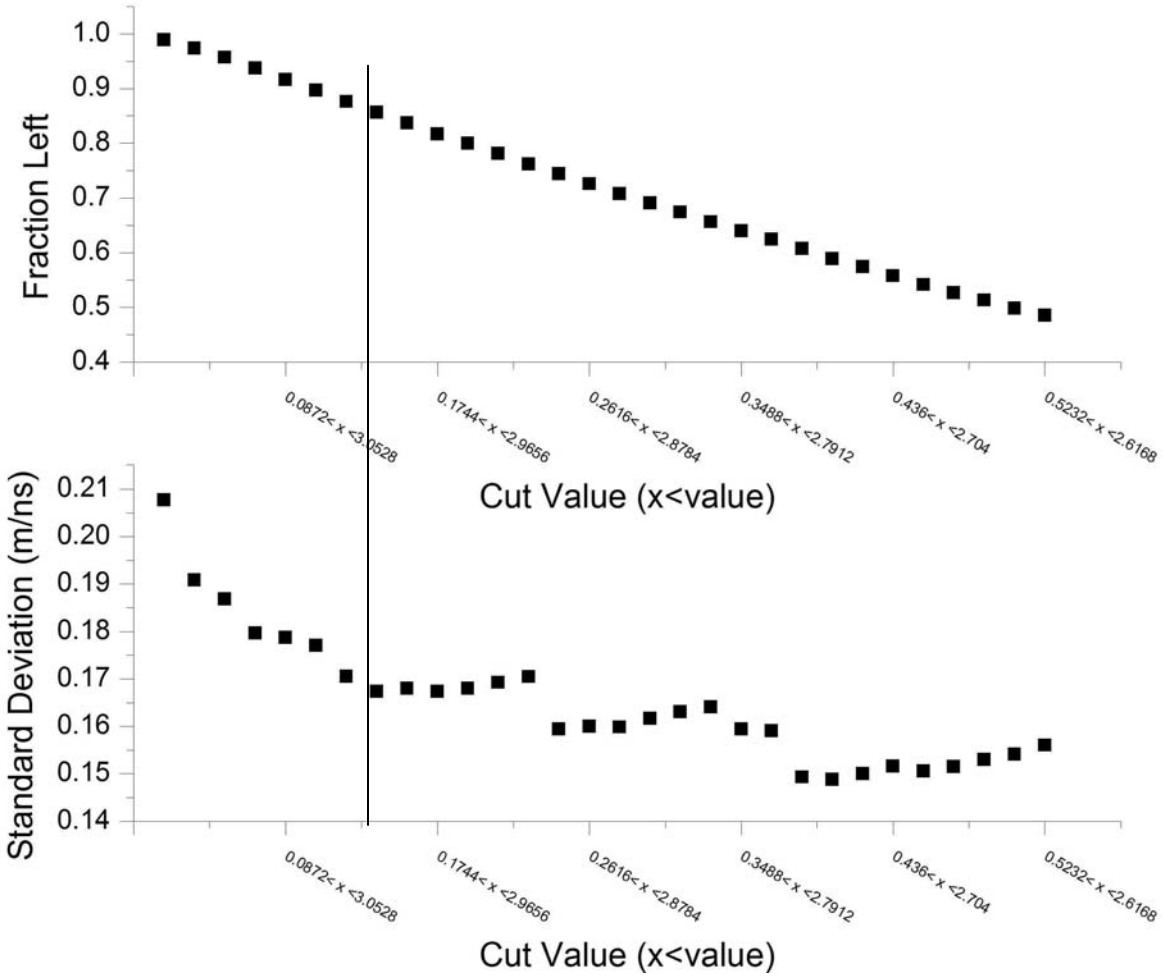

Figure 30: Opening angle cut comparison for HiRes 2. Line shows proposed cut.

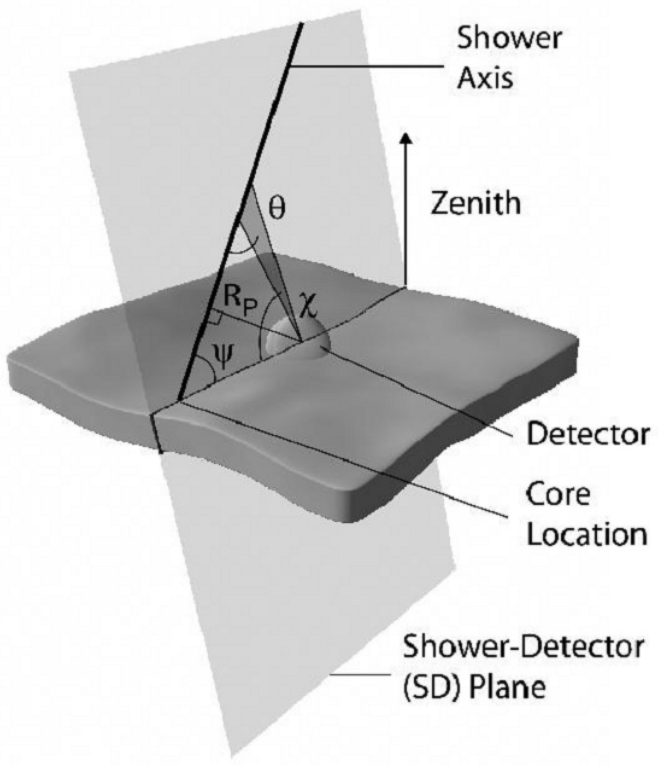

Figure 31: Angles calculated during reconstruction

It turns out that it is also useful to look at events moving at near horizontal away from the detector. When observed, these events often pass over one of the two detectors and very close to mirrors. While comparing reconstructed shower detector planes to thrown shower detector planes, it was noted that these events also tended to reconstruct incorrectly.

Figure 32 and Figure 33 demonstrate the effect of cutting away events with ψ less than a given cut angle. As with previous graphs, the bottom plot of each shows the RMS of the set of speeds for each detector remaining after events with ψ less than the cut value given on the horizontal axis is made. The top plot shows the percentage of events remaining after the same cut has been made. Looking at the top plot of each, a fairly small portion of data is removed under initial cuts up to approximately 30 degrees. The RMS, however, does decrease in this range. The decrease in the RMS levels out at approximately 60degrees before starting to increase as more data is removed. This suggests that a cut can be made on ψ. Given that the actual improvement in RMS was small under this cut, this cut was performed after both the Opening Angle and Fitting Error cuts.

θ Cut

As shown in Figure 31, θ is the angle between $\overrightarrow{R_p}$ and the vertical. As with the ψ cut, this cut removes events traveling at near horizontal. While ψ deals mostly with events coming towards or going away from the detector, θ deals with events traveling directly over the detector. As with events traveling towards or away from the detector, it is often difficult to reconstruct events that pass directly over one of the two detectors.

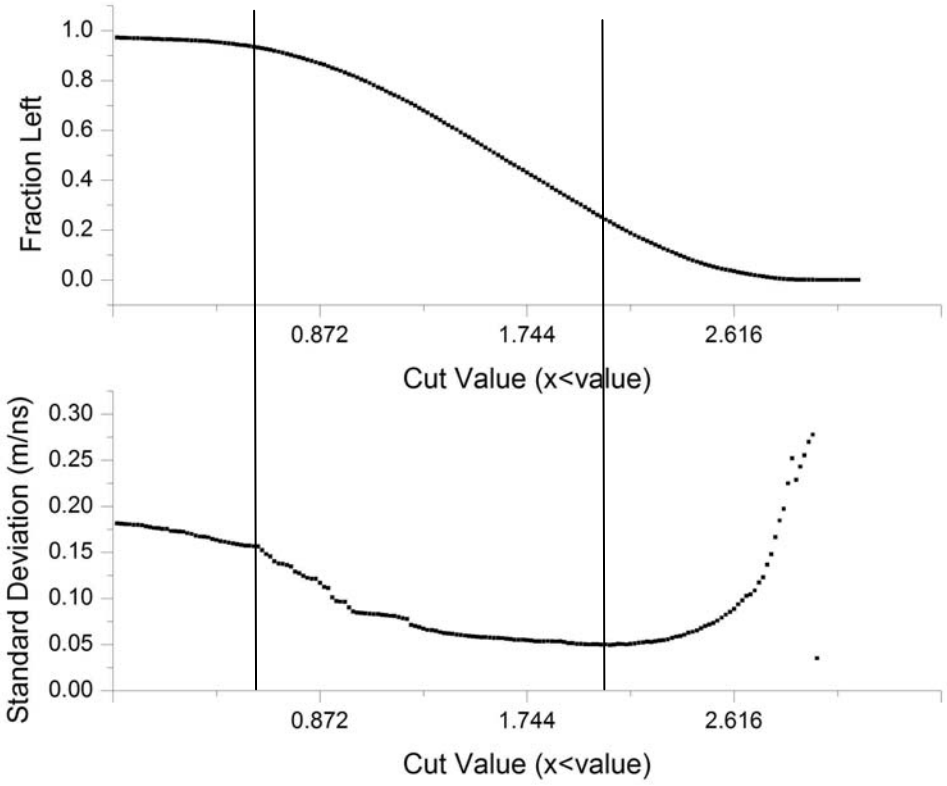

Figure 32: The ψ angle comparison plot for HiRes 1. Angle given in radians. Lines show proposed cuts (events between lines kept).

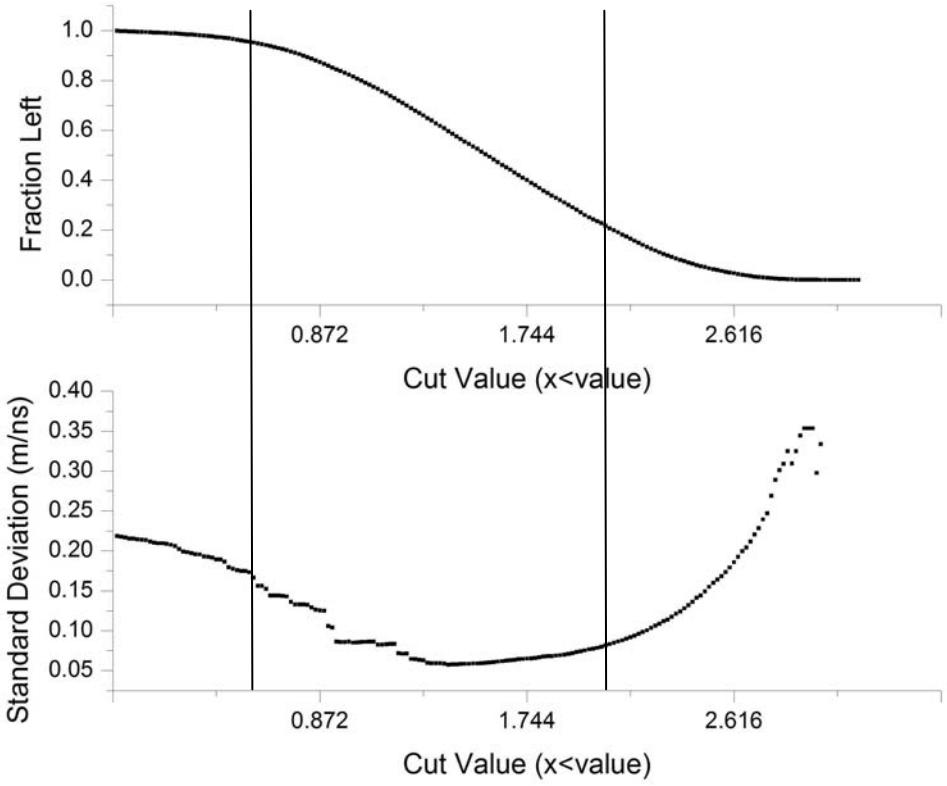

Figure 33: The ψ angle comparison plot for HiRes 2. Angle given in radians. Lines show proposed cuts (events between lines kept).

Figure 34 and Figure 35 show comparisons made between the RMS and percentage of data cut for different values of θ. Here the cut corresponded to removing all events with θ greater than the cut value. As can be seen in both plots, at large angles of θ, the RMS drops slightly while the percentage of data remains mostly constant. This effect is not as pronounced as in previous cuts.

Both graphs also exhibit somewhat erratic behavior as the amount of data left grows smaller. This is expected as individual data points have a greater weight on the overall RMS as the size of the data set diminishes. For this reason, no attempt to determine what value of θ to cut was made at this point. Instead, the value was only determined after other cuts were made.

Normalized Difference Cut

As mentioned previously in Chapter VII, a cut was applied to the normalized difference (the ratio of the difference between HiRes 1 and HiRes 2 in speeds to the estimated error). The speeds from the two sites were observed to be correlated due to the common geometry used in determining the plane intersection. Because all speeds are necessary to calculate the correlation, this cut could not be performed until after the entire set was processed. It was therefore the last cut performed on the read data. The ratio and covariance factor where then calculated as shown in Equations 47 and 48.

$$\partial_n = \frac{m_{HR1} - m_{HR2}}{\sqrt{(\sigma_{HR1}^2 + \sigma_{HR2}^2) + 2 * Cov(\sigma_{HR1}, \sigma_{HR2})}} \tag{47}$$

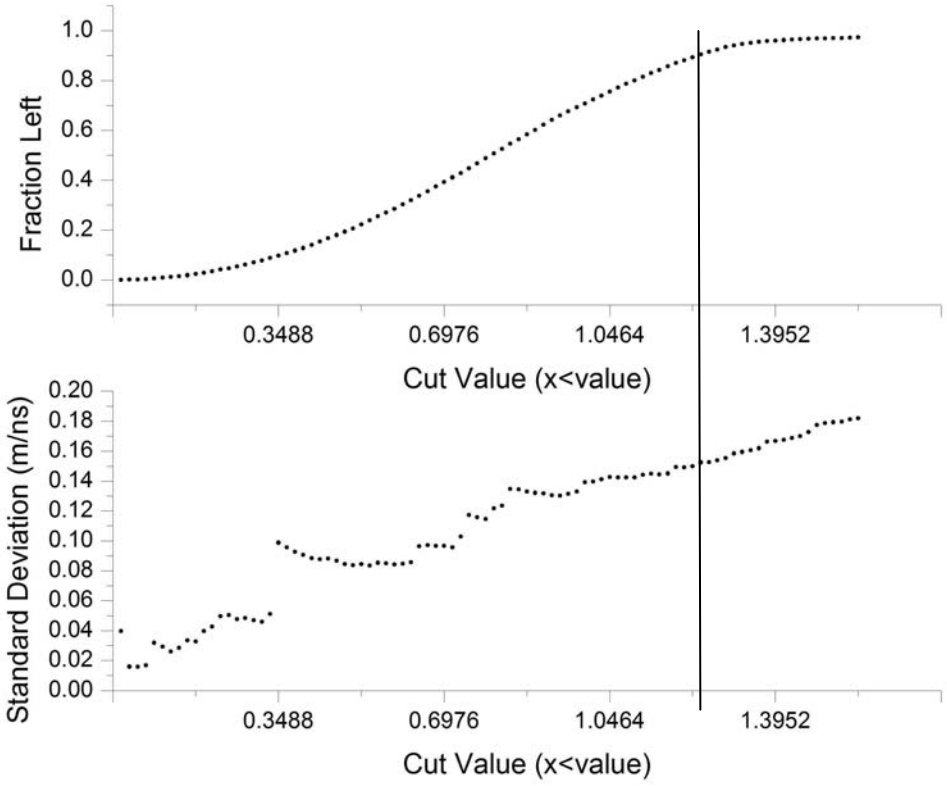

Figure 34: The θ angle cut comparison for HiRes 1. Line shows proposed cut.

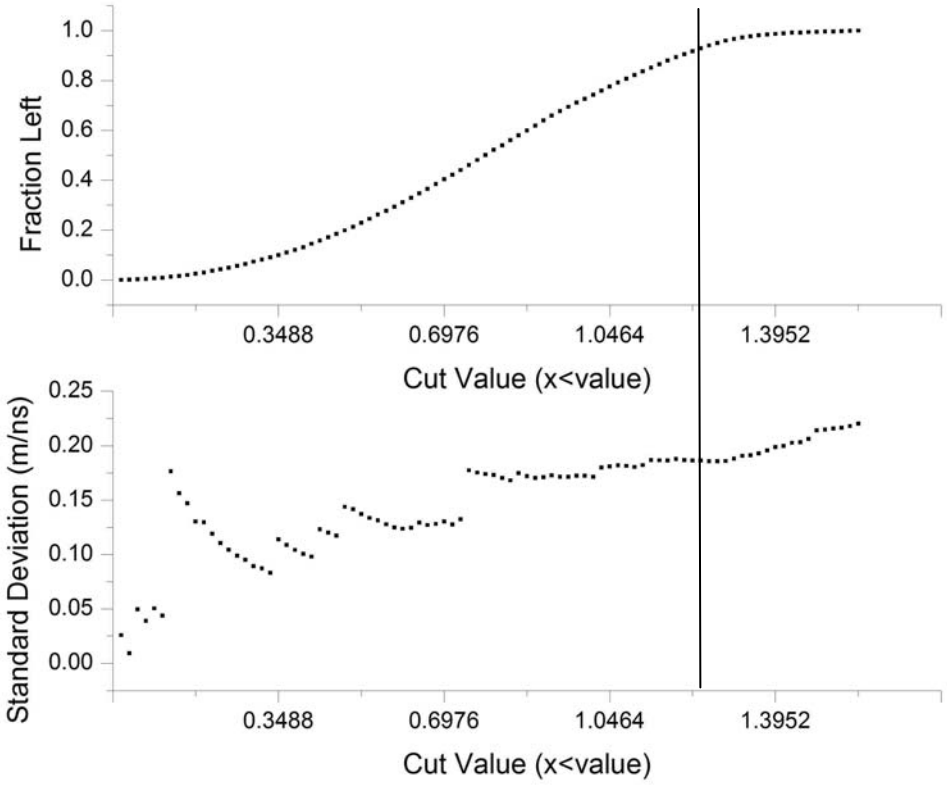

Figure 35 : The θ angle cut comparison for HiRes 2. Line shows proposed cut.

$$Cov(\sigma_{HR1}, \sigma_{HR2}) = \frac{1}{n-1}\sum_{i=1}^{n}\left(\sigma_{HR1_i} - \overline{\sigma_{HR1}}\right)\left(\sigma_{HR2_i} - \overline{\sigma_{HR2}}\right) \quad (48)$$

To validate the cut, the same procedure used with previous cuts was followed. The results are shown in Figure 36 and Figure 37. To calculate these values, the RMS for HiRes 1 and HiRes 2 was used in place of a Gaussian standard deviation.

If the Gaussian standard deviation had been used, then Equation 48 would result in the number of standard deviations by which the two speeds were separated. Using the RMS instead results in a fraction of the RMS by which the events are separated. The actual value for this cut could not be calculated until after the real data had been analyzed, so these plots are included only as reference to show how the ratio correlates with the RMS.

Cuts Not Made

For reference, a number of other variables were examined for possible data selection cuts. Ultimately it was determined that none of them increased the quality of the data set enough to justify the amount of data they removed. Due to the number of possible cuts tried, it is not practical to list each of them here. However, for the benefit of collaborators, a summary of each cut and the reason they were not chosen is given in Appendix C.

Combined Cuts

After selecting the quatitites to cut on, the set of cuts must be optimized to minimize the amount of data removed. In this process, the order is important. Each cut removes a portion of the data resulting in a new data set. The effect of a cut on the new

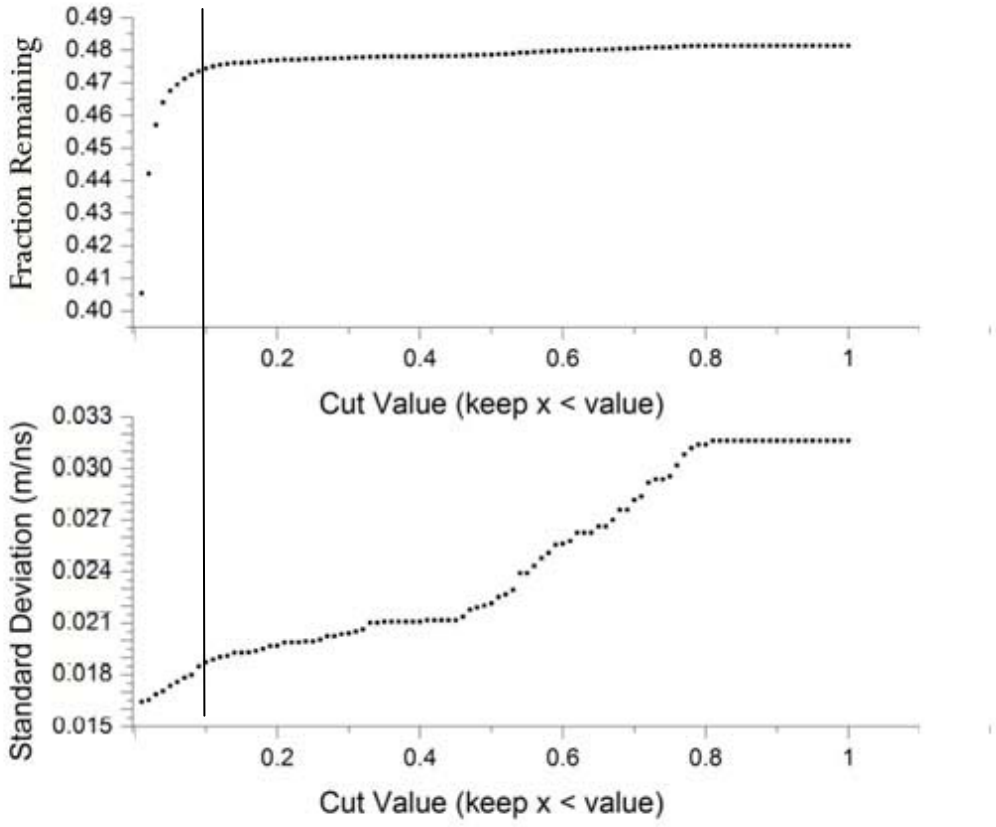

Figure 36 : RMS comparison for HiRes 1. Line shows proposed cut.

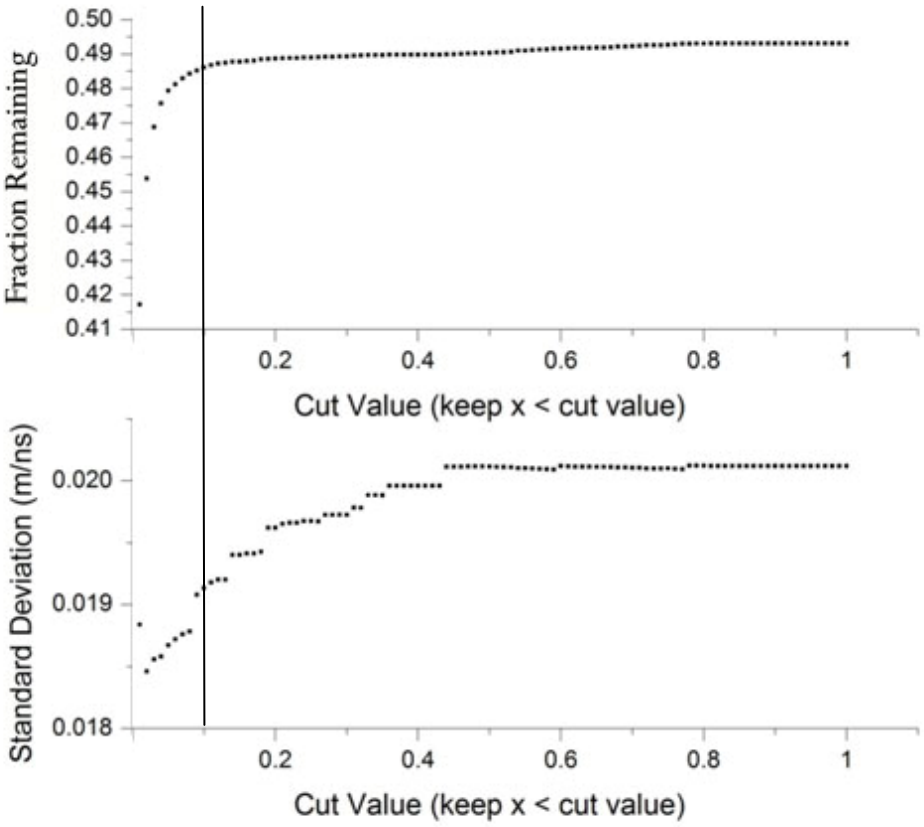

Figure 37: RMS comparison for HiRes 2. Line shows proposed cut.

data set is not guarenteed to be the same as that on the original. As an example of why this happens, wide events with large σ_{boot} tend to happen close to a detector. This in general gives very small opening angles. Therefore cutting on opening angle removes many of the events a cut on σ_{boot}would remove. The desire is to keep the cuts as loose as possible while still improving the quality of the data. A strict cut on opening angle may allow for a much looser cut on σ_{boot} or vice versa.

It is important to note that the goal of the cuts was to retain as much data as possible for the search while still eliminating common causes for error in the speed calculation. The philosophy of applying loose cuts that removed data slowly first was adopted in an attempt to minimize data loss. Therefore, the most important factor in determining which cut to apply first was the rate at which individual cuts remove data. Figure 22, Figure 23, Figure 27, and Figure 29 show that the opening angle cut removes data much faster than the σ_{boot} cut. To minimize data loss, the σ_{boot} cut was performed first, followed by the opening angle cut.

Because both the cuts on θ and ψ cut data very quickly once they begin to remove data, these were applied after the opening angle plots.

Once order had been determined, several plots of standard deviation of shower speed vs. opening angle were made for given cut values of σ_{boot}. These plots were generated by first making the cut $\sigma_{boot} < \sigma_{cut}$. After this cut was made, a series of cuts of the form $Cut\ Angle < \theta_{opening} < (180 - Cut\ Angle)$ were made. $\theta_{opening}$ was varied between 0 and 30 degrees. Examples of these are shown in Figure 38 and Figure 39.

Each figure includes three plots. These plots were selected to be near the starting range for the σ_{boot} cut found earlier in the Fitting Error section. These plots are similar to those shown earlier for cuts. The top panel in each plot shows the percentage of events left after a cut on opening angle has been made. The bottom panel of each plot shows the RMS of the remaining sample after the cut has been made.

The plots in both Figure 38 and Figure 39 share some common features. As the opening angle cut increases, the RMS drops quickly at first until it approaches a minimum value. The amount of data removed by each cut is approximately linear. For the HiRes 1 plots, the RMS follows a smooth curve until approximately 10 degrees. For the HiRes 2 plot, the RMS begins to level out at around 7.5 degrees.

These plots show 3 different values of σ_{boot} for each used to cut on. As expected, the amount of data available at the start of each cut drops as the σ_{boot} cut gets tighter. Choosing the exact cut value then becomes a balancing act. Looking at Figure 39, we can see that an Opening Angle cut of 7.5 degrees with $\sigma_{boot} = 0.0025$ m/ns results in approximately the same RMS as a cut of 10 degrees with $\sigma_{boot} = 0.0030$ m/ns. HiRes 1 follows a similar pattern to that shown in Figure 38. This was used as a baseline value to choose cuts. These cuts were set at $\sigma_{boot} = 0.0025$ m/ns for HiRes 1, $\sigma_{boot} = 0.0027$ m/ns for HiRes 2, and 7.5 degree < Opening Angle < 172.5 degree.

Once the cuts for σ_{boot} and Opening Angle were determined, the cuts for ψ and θ were reexamined. Similar plots to those made from the whole data set were mad from the data set remaining after the cuts on σ_{boot} and Opening Angle had been made. These

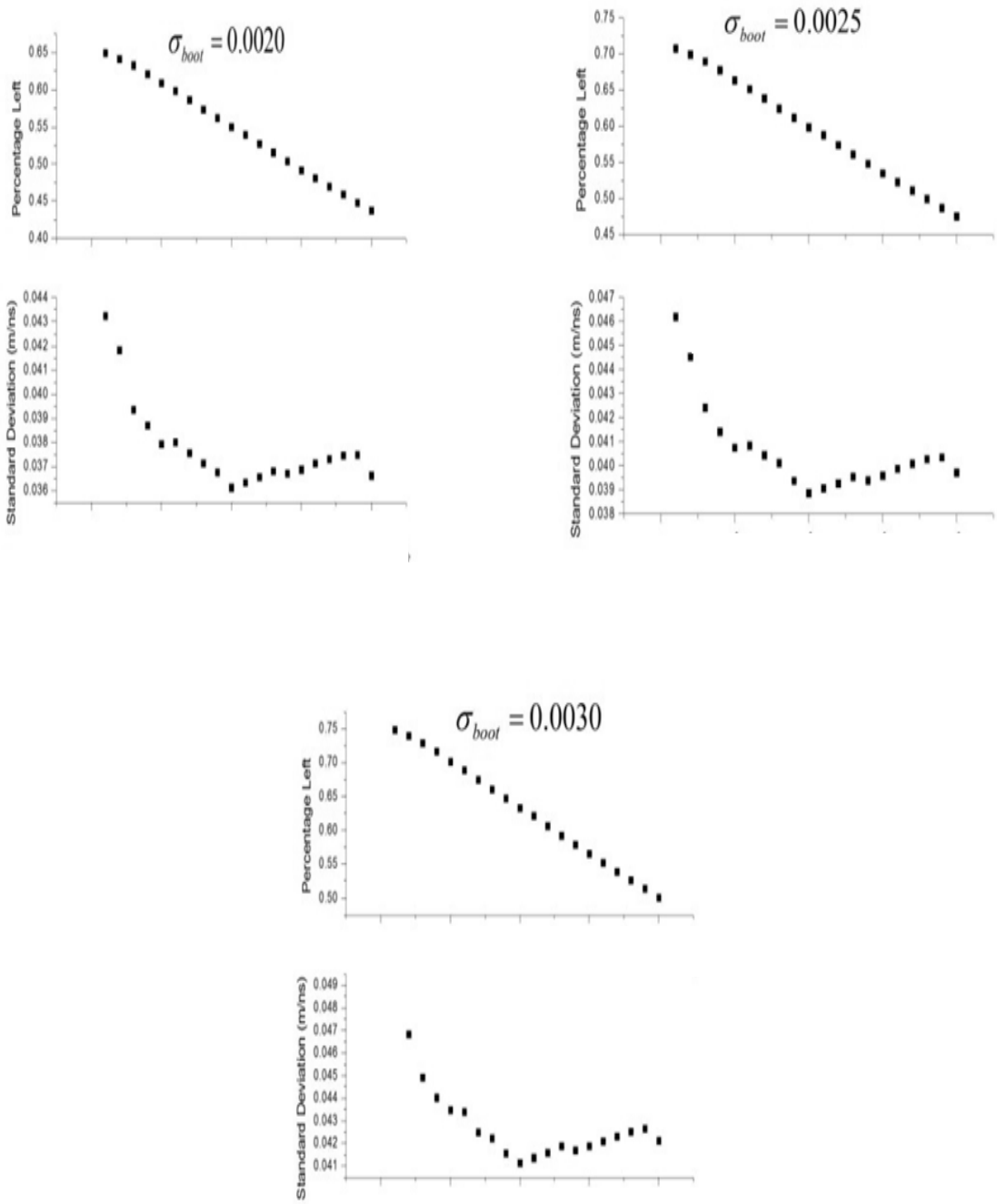

Figure 38: Example in order cut plots for HiRes 1. Horizontal points each represent 1 degree cuts starting at 0.

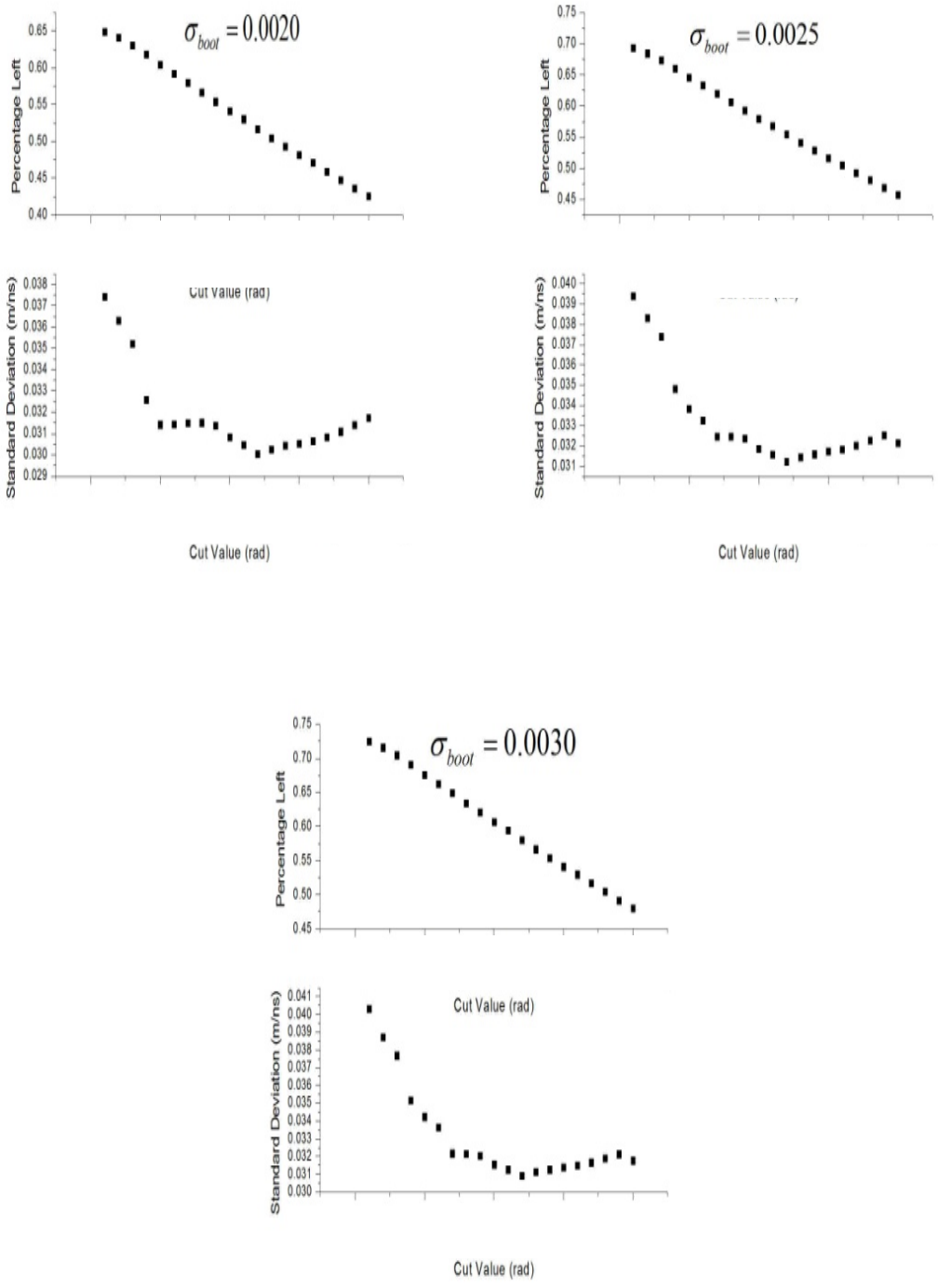

Figure 39 : Example in order cut plots for HiRes 2. Horizontal points each represent 1 degree cuts starting at 0.

are shown for θ in Figure 40 and Figure 41. They are shown for ψ in Figure 42 and Figure 43.

For these cuts, the goal was to remove as little data as possible while still lowering the RMS of the resulting distribution. One of the first things apparent comparing Figure 40 and Figure 41 with previously shown Figure 34 and Figure 35 is that the cuts made on σ_{boot} and Opening Angle removed much of the data, causing the lower portions of these graphs to behave erratically. When cuts are made removing portions of the data set with θ > ~70°, only small portions of the data set are actually removed. This can be seen by looking at the top panel in Figure 40 and Figure 41. On the other hand, the corresponding drop in RMS is on the order of 30%.

A similar trend appears when looking at Figure 42 and Figure 43. In this case, a cut removing data with ψ < ~30 degrees also reduces the remaining data set by only a small amount (~4%) but reduces the RMS by approximately 30%.

The bounds θ>70° and ψ<30° were chosen as data selection parameters for the data set. The same value was used in each case for HiRes 1 and HiRes 2, resulting in 4 total cuts from these two angles.

All cuts made to this point are summarized in Table 9. The cuts are separated into two sections, with cuts made during reconstruction appearing on the left and those made after on the right.

To this point, comparisons for cuts have been done using the RMS for the set of all shower speeds. As can be seen in Figure 17 and Figure 18, with no cuts made, these were calculated to be $\sigma_{hr1} = 0.181$ m/ns and $\sigma_{hr2} = 0.587$ m/ns. As can be seen from

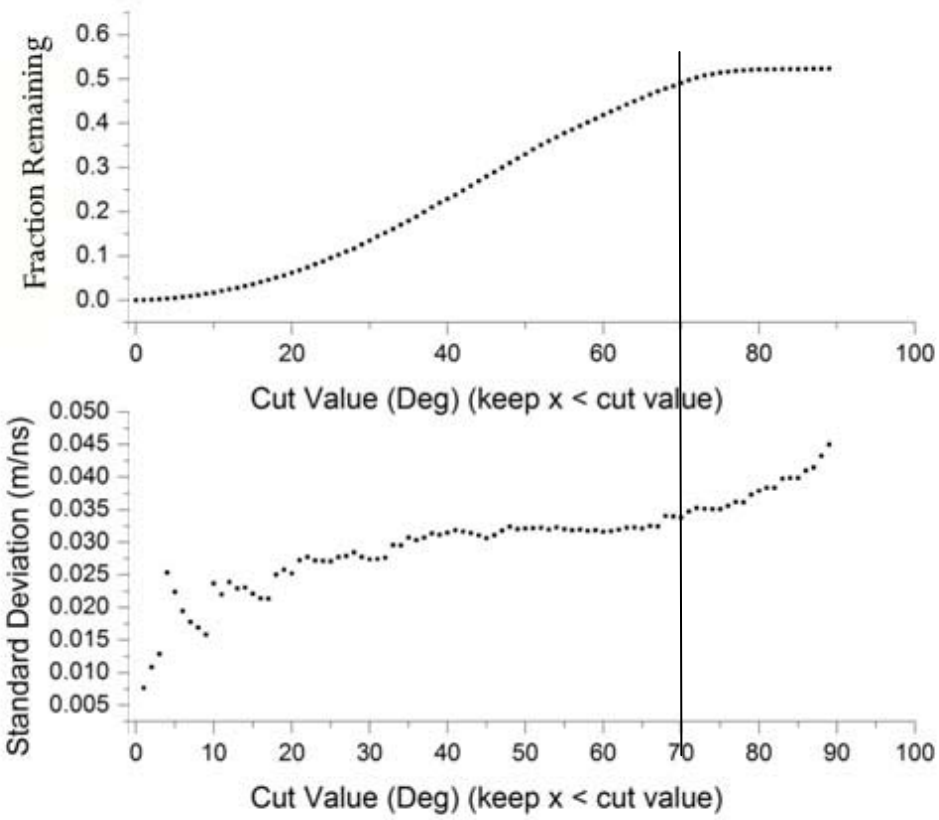

Figure 40 : Post σ_{boot} and opening angle cut on θ for HiRes 1. Line shows used cut.

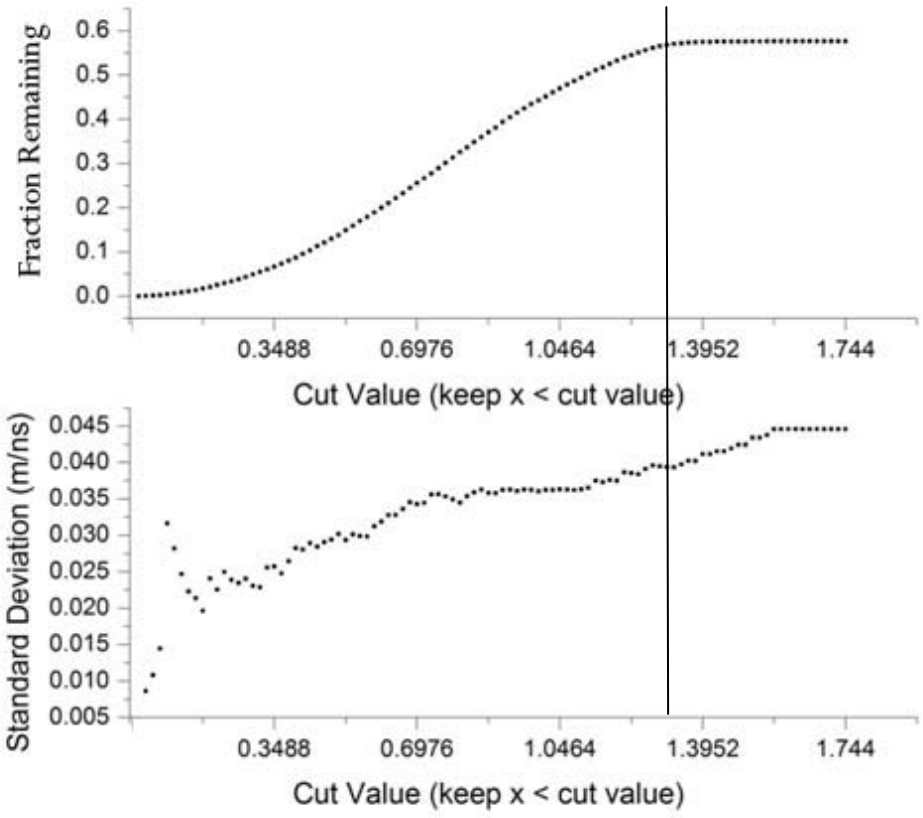

Figure 41 : Post σ_{boot} and opening angle cut on θ for HiRes 2

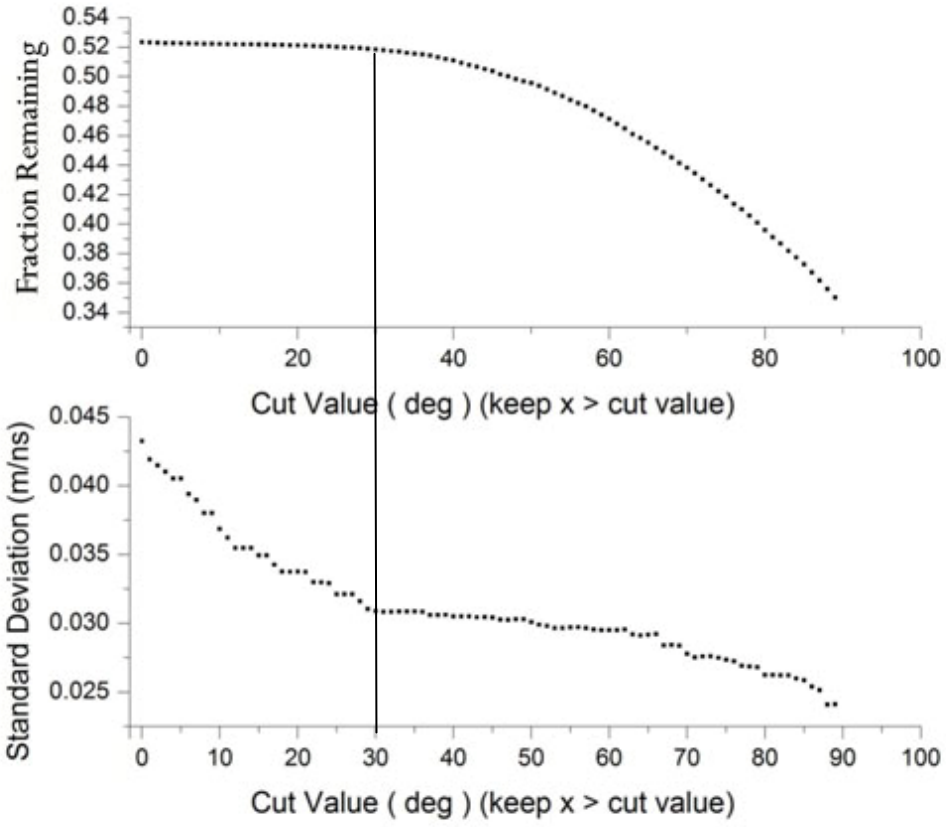

Figure 42 : Post σ_{boot} and opening angle cut on ψ for HiRes 1

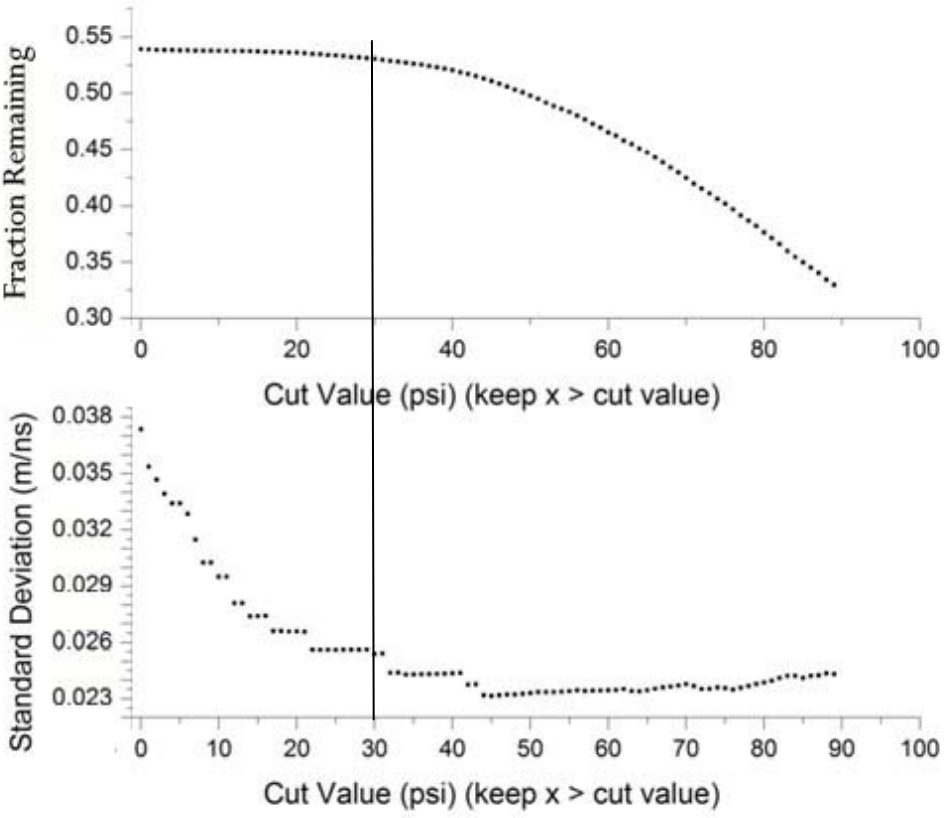

Figure 43: Post σ_{boot} and opening angle cut on ψ for HiRes 2

Table 9: Summary of data selection cuts made on real data

Reconstruction Cuts (Events kept if)	**Quality Cuts** (Events kept if)
Photoelectrons per tube > 1.0	7.5° < Opening Angle < 172.5°
Triggered tubes > 6	HiRes 1 σ_{boot} < .0025
Photoelectrons per good tube > 15.0	HiRes 2 σ_{boot} < .0027
3° < Track Length HR1 < 36°	HiRes 1 and 2 ψ > 30°
6° < Track Length HR2 < 57°	HiRes 1 and 2 θ < 70°
plog > 2.0	Track Length > 8°
	HiRes 1 $\vec{R}_p$> 2.5 km
	HiRes 1 and 2 ψ < 120
	$\partial_n < .15$
	HR1 adjusted “good” tubes > 3

Figure 44 and Figure 45, these are reduced to $\sigma_{hr1} = 0.019$ m/ns and $\sigma_{hr2} = 0.017$ after the cuts are made. Both show improvement over their initial values.

However, comparison of the RMS calculated in this manner does not necessarily indicate overall changes in the distribution. To compare distributions before and after, Figure 44 and Figure 45 show the resulting histograms of the data after all cuts had been made. The data is then fit with a Lorentz function as it was in Figure 17 and Figure 18 for comparison. Both distributions show marginal improvement in the FWHM of the peak. However, overall, the distribution did not change significantly after cuts, except that the long tails were shortened significantly.

This is both the expected and desired result. As the cuts are designed to remove the tails of the distribution and not alter the distribution itself, significant changes to the width of the distribution would indicate that data was being removed at a rapid rate from the peak centered around the actual thrown speed. It is worth noting that while the center of the peaks did not shift, the mean for HiRes 1 did shift. The mean after all cuts were completed is much more in line with the actual fitted peak of the Lorentz distribution.

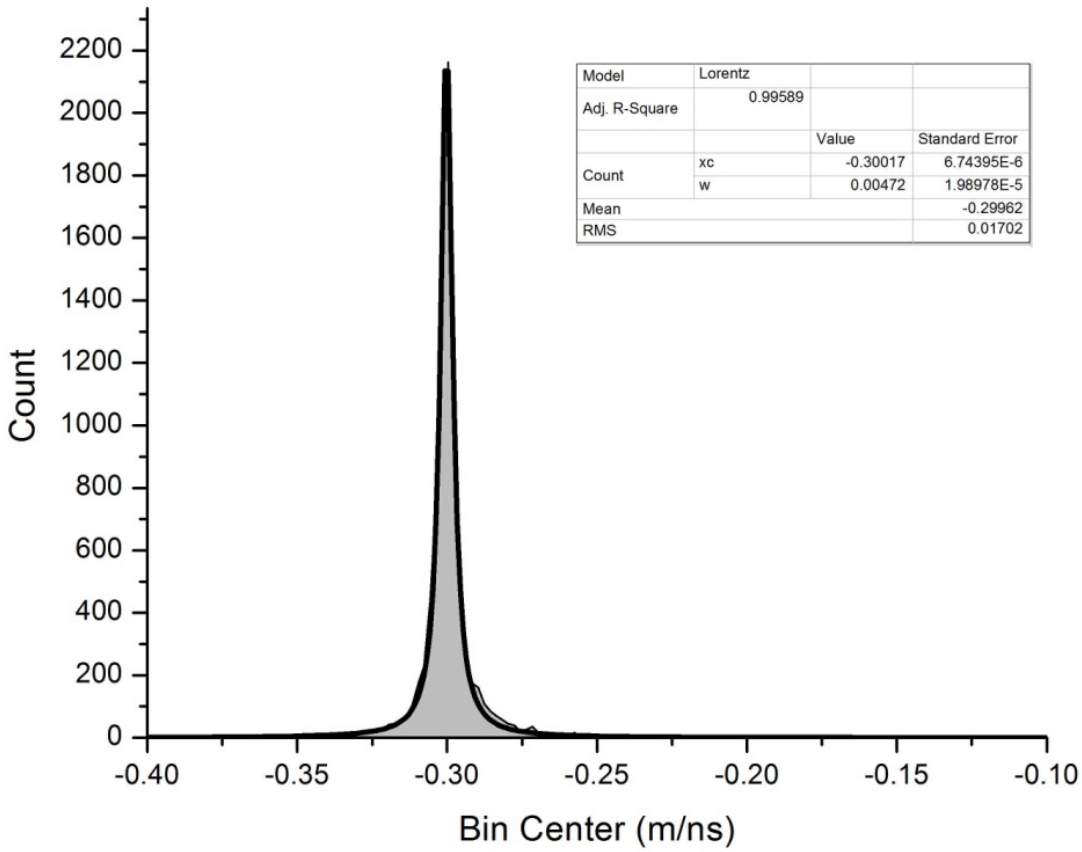

Figure 44: Histograms of Monte Carlo data after all cuts have been made for HiRes 2

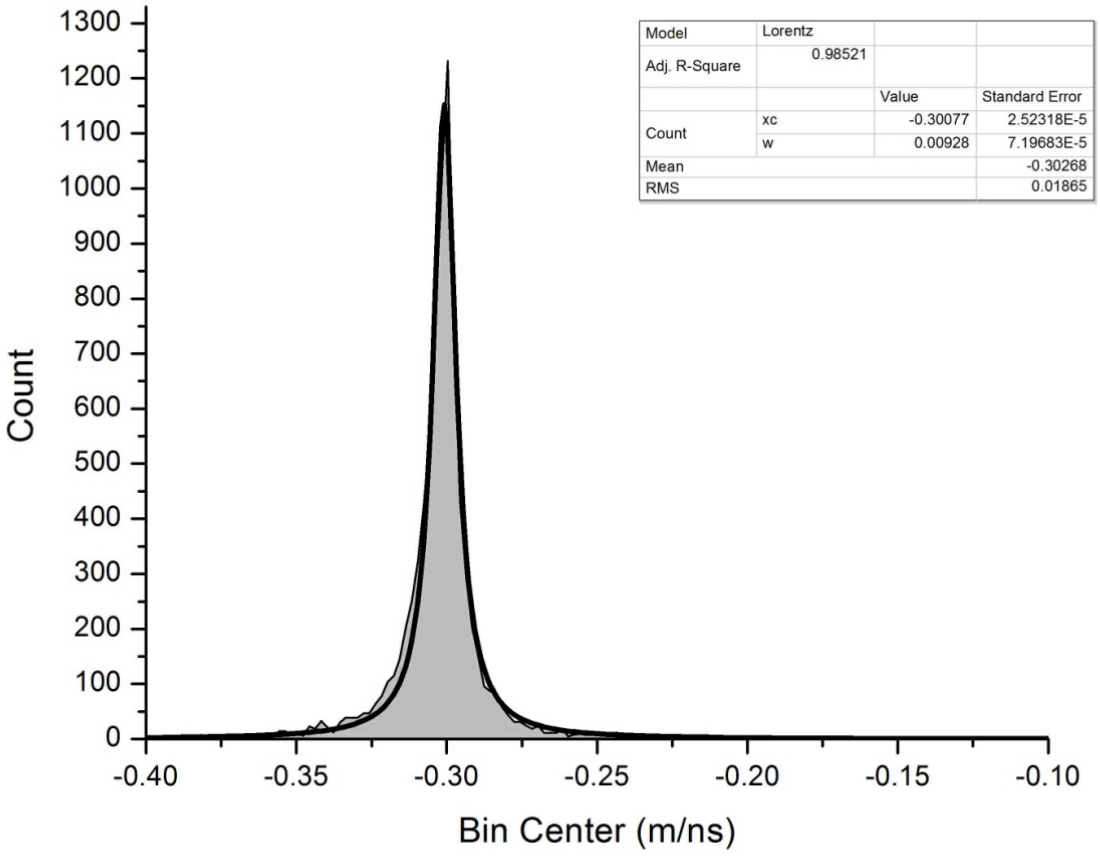

Figure 45: Histograms of Monte Carlo data after all cuts have been made for HiRes 1

CHAPTER IX

PROCESSING RESULTS

The HiRes stereo data collected between December of 1999 and November of 2005 were processed and run through the *shower_speed* program described in Chapter VI. From these, 49,164 events contained the necessary information for speed reconstruction. Those events were further subjected to the data selection criteria given in Chapter VIII. For reference, a summary of those cuts was given in Table 9.

In total, 49,164 events were processed. The resulting distributions of shower speeds with no cuts applied are shown in Figure 46 and Figure 47.

There are several notable features in both graphs. First, each shows three distinct peaks. The first of these peaks is located at -0.300 m/ns in each graph. This is consistent with the speed of light. The negative sign indicated downward moving events. This peak then corresponds to normal hadronic events entering the atmosphere. A second peak on each graph is located at 0.290 m/ns for HiRes 2 and 0.299 m/ns for HiRes one. This peak is also consistent with the speed of light in both cases. This peak corresponds to upward-going events. The bulk of these are vertical Xenon flasher events that were not removed in previous processing. The third peak for each graph is located ~0 m/ns. This peak consists mostly of correlated noise events, including airplane triggers left over from previous filters.

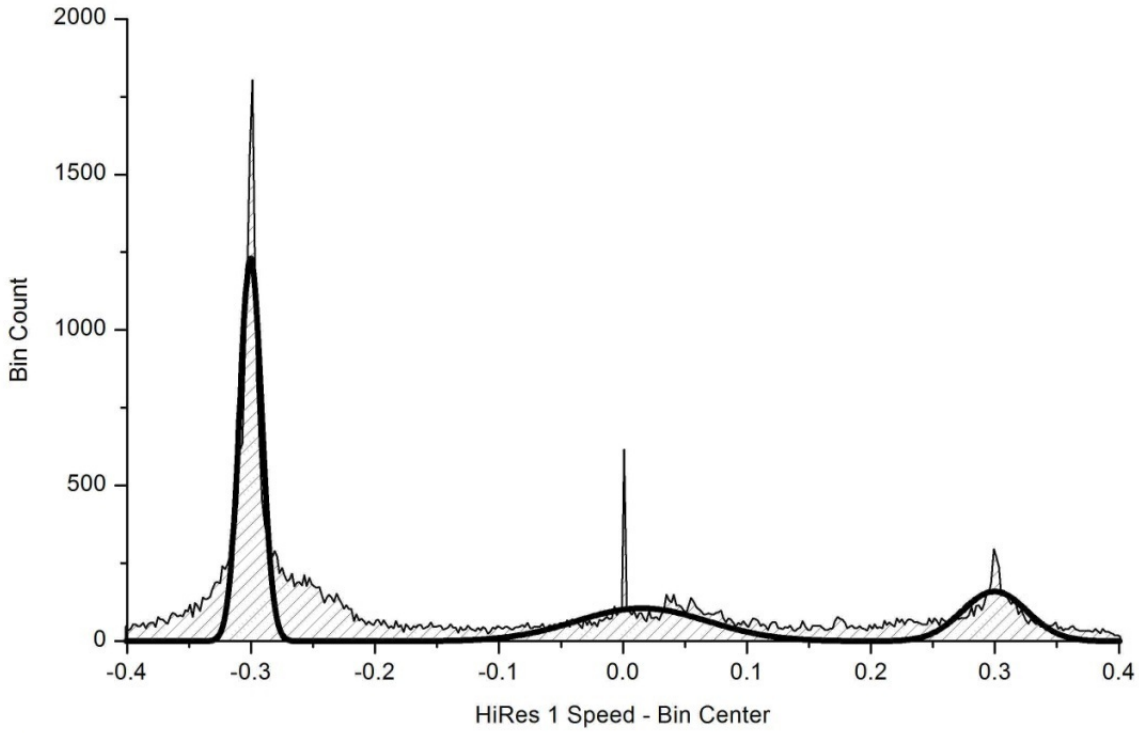

Results

Peak Type	Area Intg	FWHM	Max Height	Center Grvty	Area IntgP
Gaussian	27.38616	0.02089	1231.81894	-0.30026	52.74601
Gaussian	14.08155	0.12539	105.50076	0.01523	27.12121
Gaussian	10.45311	0.06159	159.44933	0.29975	20.13279

Figure 46: Histogram of shower speeds for uncut real data for HiRes 1. Graph includes fit to 3 best peaks. Speed is given in m/ns.

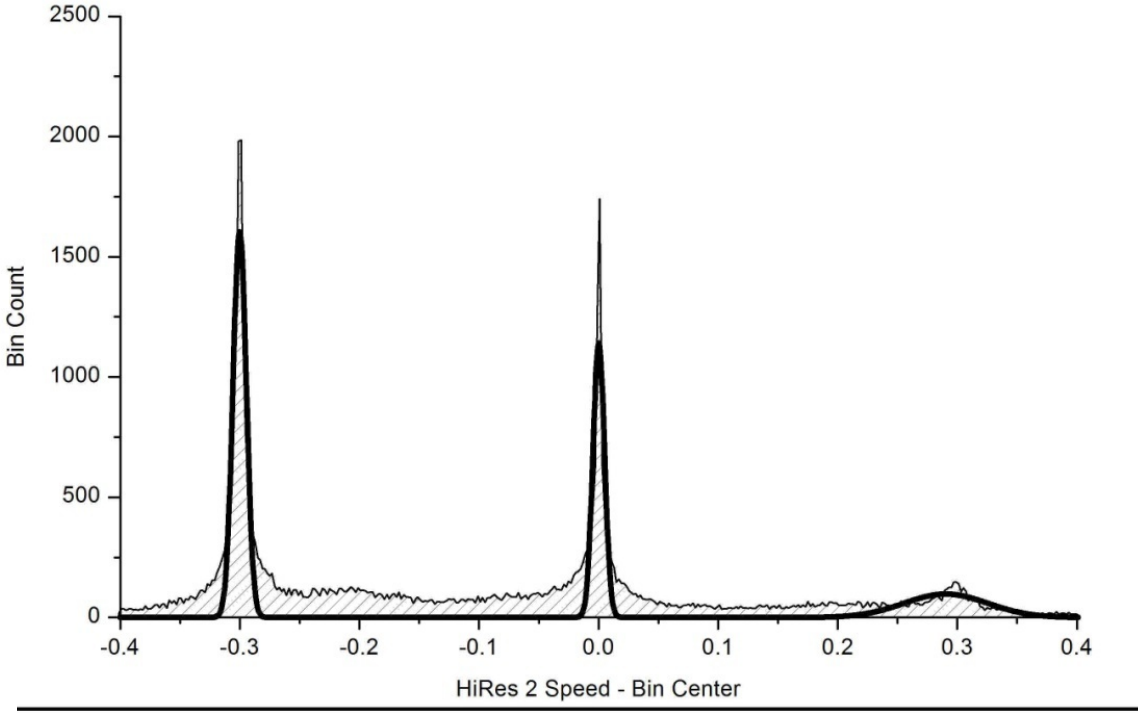

Results

Peak Type	Area Intg	FWHM	Max Height	Center Grvty	Area IntgP
Gaussian	22.35341	0.01309	1604.45913	-0.30016	50.02263
Gaussian	13.79404	0.01136	1140.80776	1.5E-4	30.8684
Gaussian	8.53915	0.08258	97.14752	0.2904	19.10897

Figure 47 : Histogram of shower speeds for uncut real data for HiRes 2. Graph includes fit to 3 best peaks. Speed is given in m/ns.

Table 10: Number of events removed by cuts

Cut	# events	% cut (in order)
No good speed fit for either site	1227	2.5%
Plog	201	.41%
Opening Angle	37	.08%
Hr1 bootstrap error	949	1.9%
Hr2 bootstrap error	1283	2.6%
Hr1 θ	41	.08%
Hr2 θ	1796	3.7%
Hr1 Track Length	1378	2.8%
Hr2 Track Length	258	.53%
Hr1 $\overrightarrow{R_p}$	2461	5.0%
Maximum Recorded Tubes in a single mirror	4825	9.8%
Normalized Speed Difference > 5 rms	29297	60%

Table 10 shows the number of events removed by each cut made. The cuts are listed in order made from top to bottom. For each cut, the number of events cut when the cuts are performed "in order" is listed. This gives comparative values for how much data each cut removed.

After cuts, 3568 events remained for analysis. The resulting distributions are shown in Figure 48 and Figure 49. Each distribution is fit to a Lorentzian for comparison to MC distributions in Chapter VIII. As can be noted from each plot, the resulting centers for both peaks are located at ~ -0.300 m/ns. This is consistent with the speed of light.

The FWHM of each are 0.007 (~2.3% of speed of light) and 0.005 (~1.7% of speed of light), respectively, for HiRes 1 and HiRes 2. From these plots, the bulk of reconstructed events fall within a few percent of the speed of light. This supports the assumption that the majority of events seen are hadronic in nature and result from particles traveling at near the speed of light.

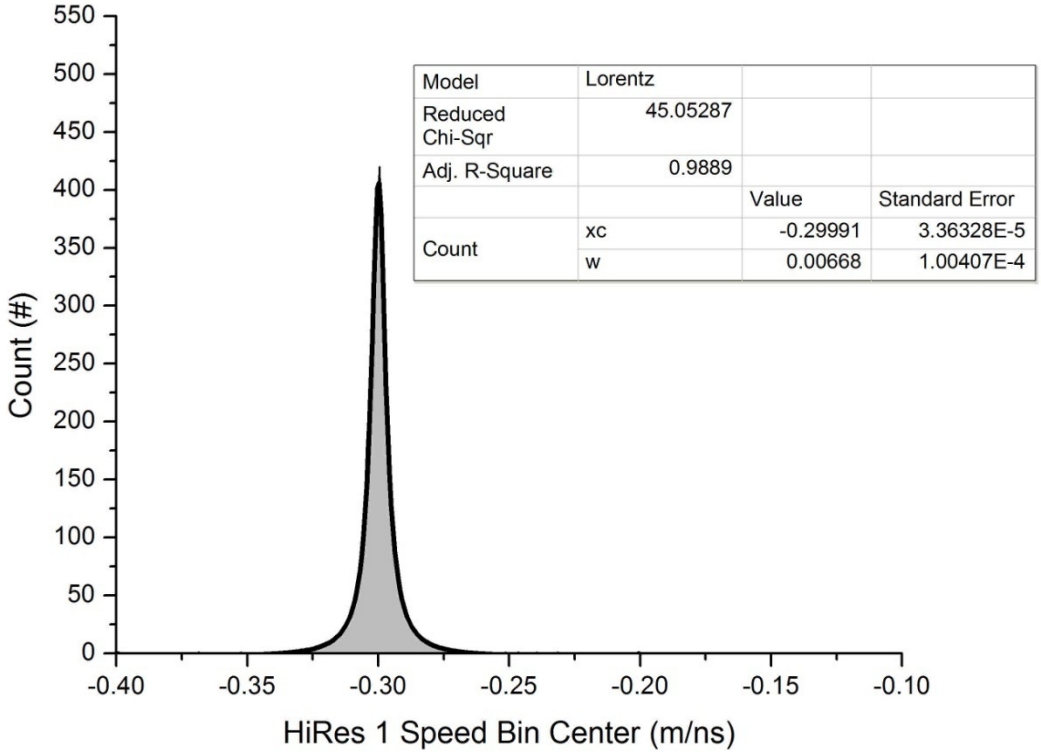

Figure 48: Histogram of HiRes 1 speeds fit to Lorentzian.

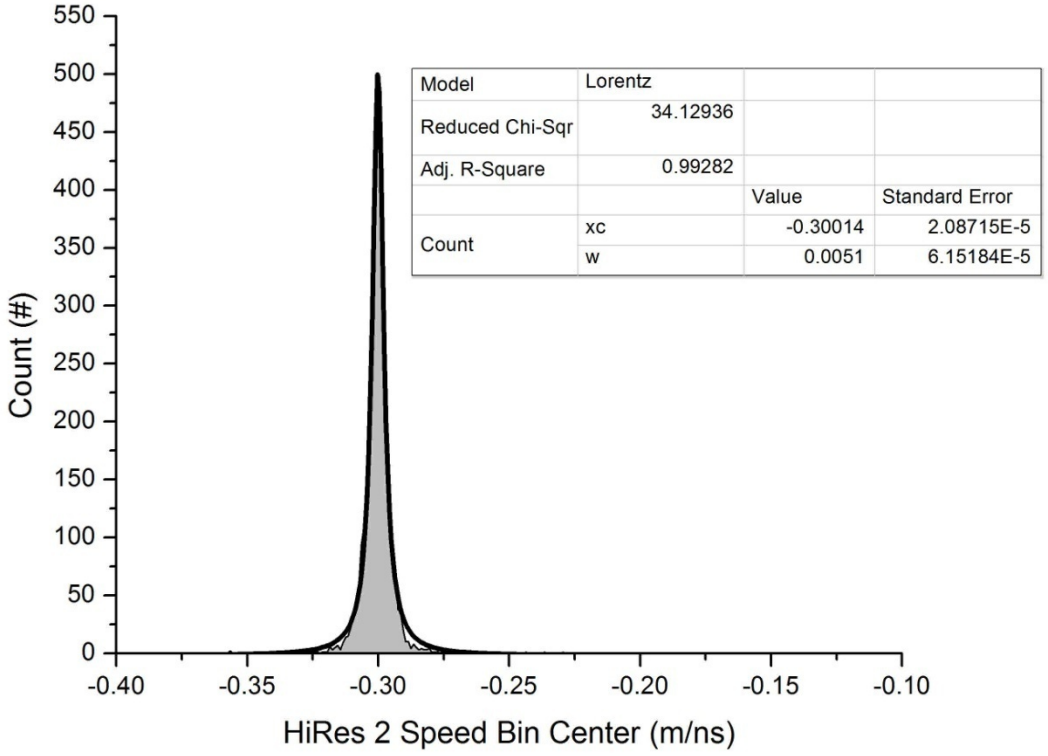

Figure 49: Histogram of HiRes 2 speeds (m/ns) fit to Lorentzian

As with the Monte Carlo simulations, both distributions have tails. Figure 50 and Figure 51 show the MC distribution and the real data distribution overlaid on the same graph and normalized to the data in the range shown for comparison.

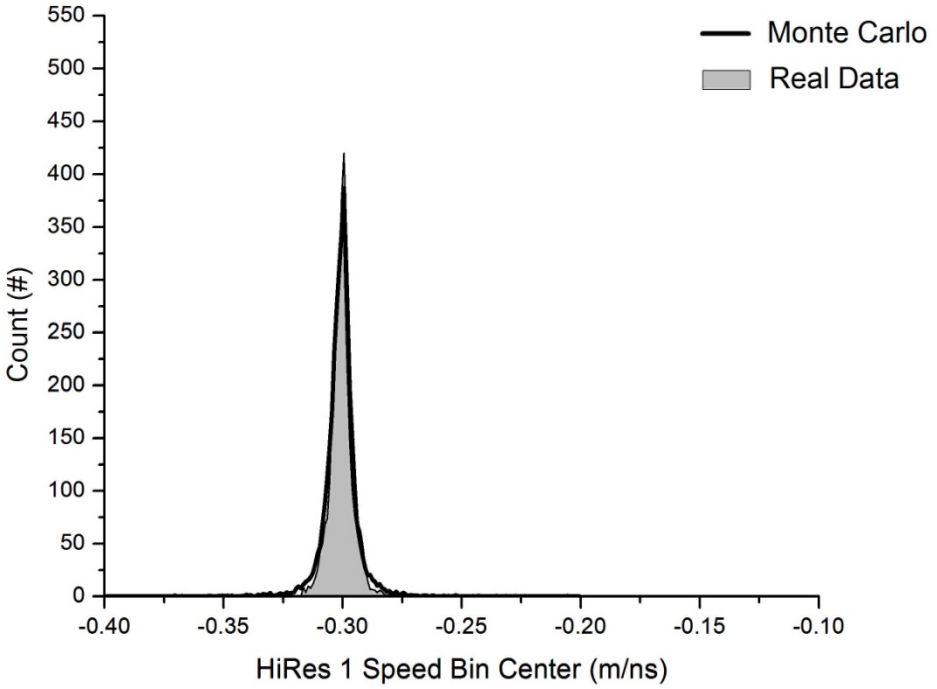

Figure 50: Overlay of HiRes 1 Monte Carlo distribution with real data distribution, both after all cuts had been made.

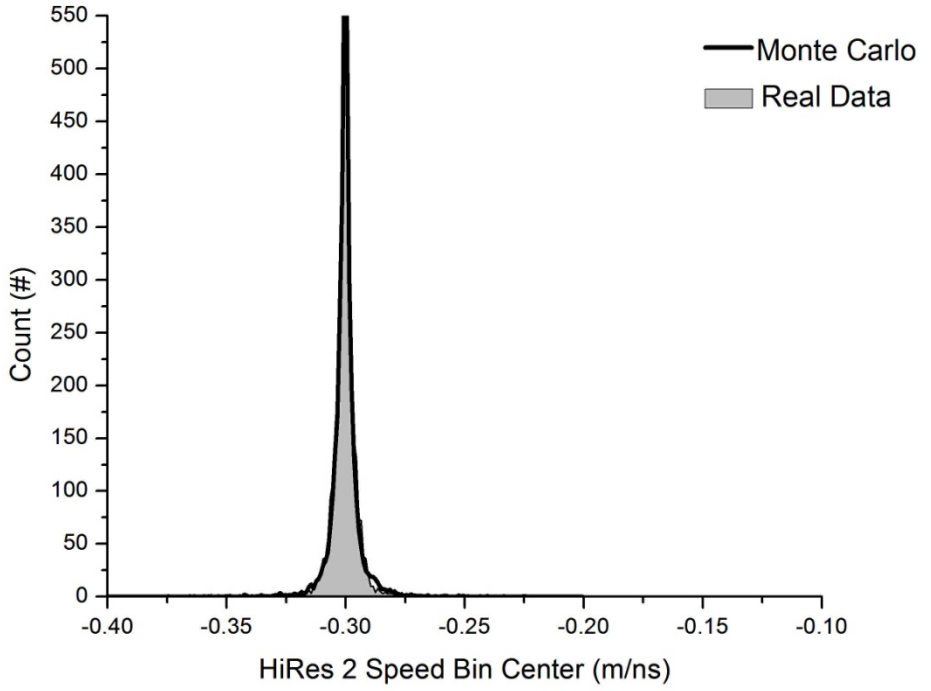

Figure 51: Overlay of HiRes 2 Monte Carlo distributionwith real data distribution, both after all cuts had been made.

CHAPTER X

OUTLIERS

As described in the previous chapter, the search of the full data set resulted in 11 events that had speeds more than 3 standard deviations from the speed of light (as calculated from the MC distributions shown in Chapter VII). These events were then scanned by eye. This scan was focused on identifying two specific types of events with abnormal speeds.

The first type of event is the result of poor reconstruction that leaked through the automated processing but was easily identified by a visual scan. One such event is illustrated by the event displays shown in **Error! Reference source not found.** and Figure 52. In this event, the HiRes 1 plane shown by the dashed line matches with the tubes the event triggered. However, the HiRes 2 plane does not match up with the tubes in the event. In order to remove the subjectivity from this type of cut, the procedure for rotating planes described in Chapter VII was applied to these events. In most cases, the plane once rotated back to the actual shower also brought the speed back to the speed of light.

The second type of event removed in this pass is illustrated in Figure 54 and Figure 55. They are characterized by a very low elevation trigger in one mirror and a large amount of photo-tubes triggering in the other. Most of this type of event were cut using plog described in Chapter VII. Some events like the one shown in and Figure 54

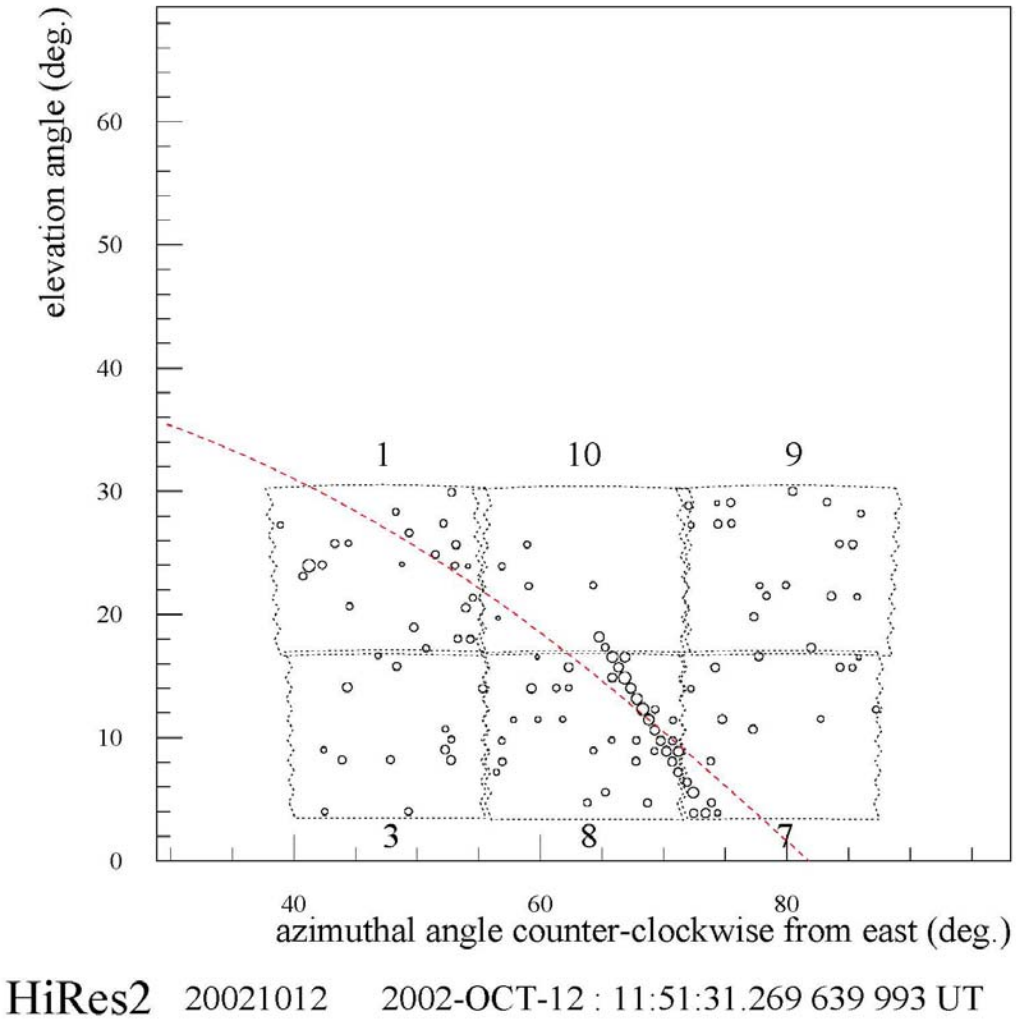

Figure 52: HiRes 2 portion of event display of event with obviously bad plane fit. The shower detector plane for HiRes 2 does not intersect with the triggered tubes.

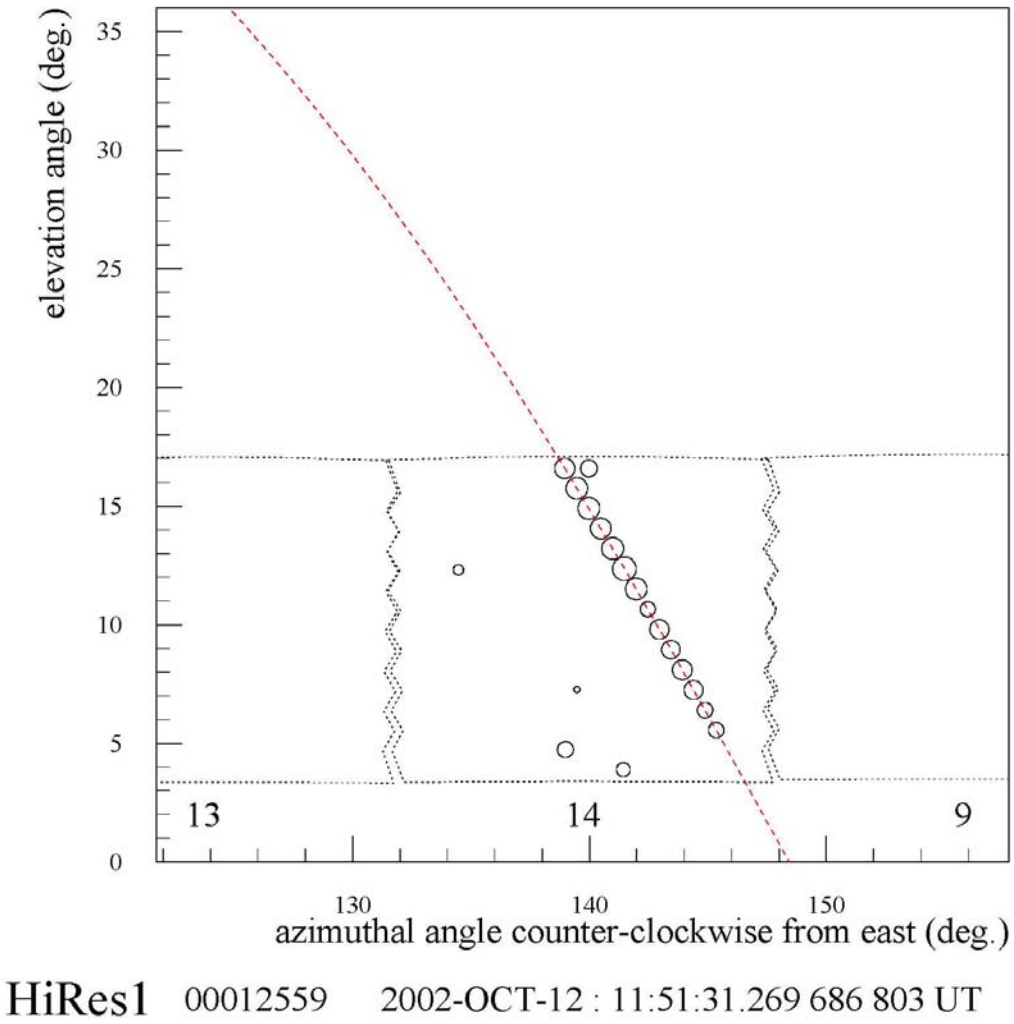

Figure 53: HiRes 2 portion of event display of event with obviously bad plane fit. The shower detector plane for HiRes 2 does not intersect with the triggered tubes.

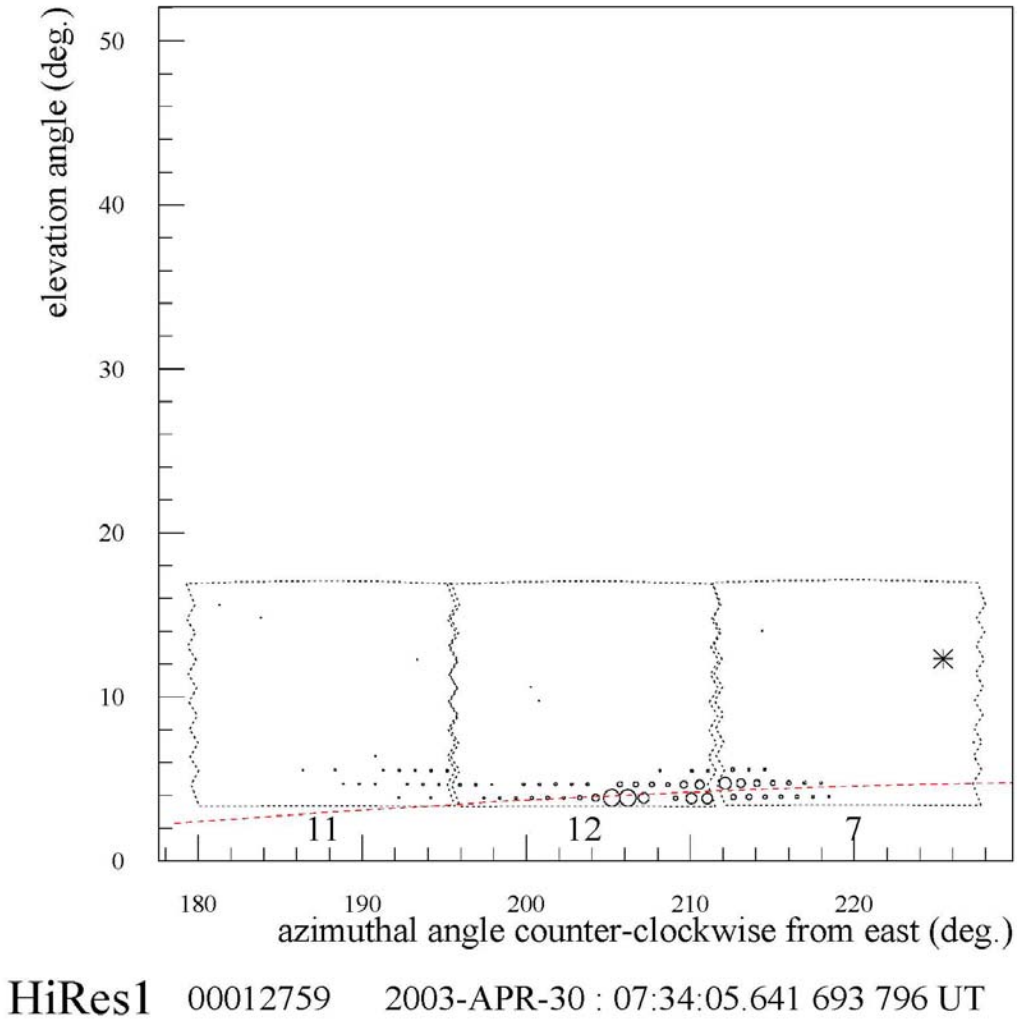

Figure 54: HiRes 1 display of possible noise event

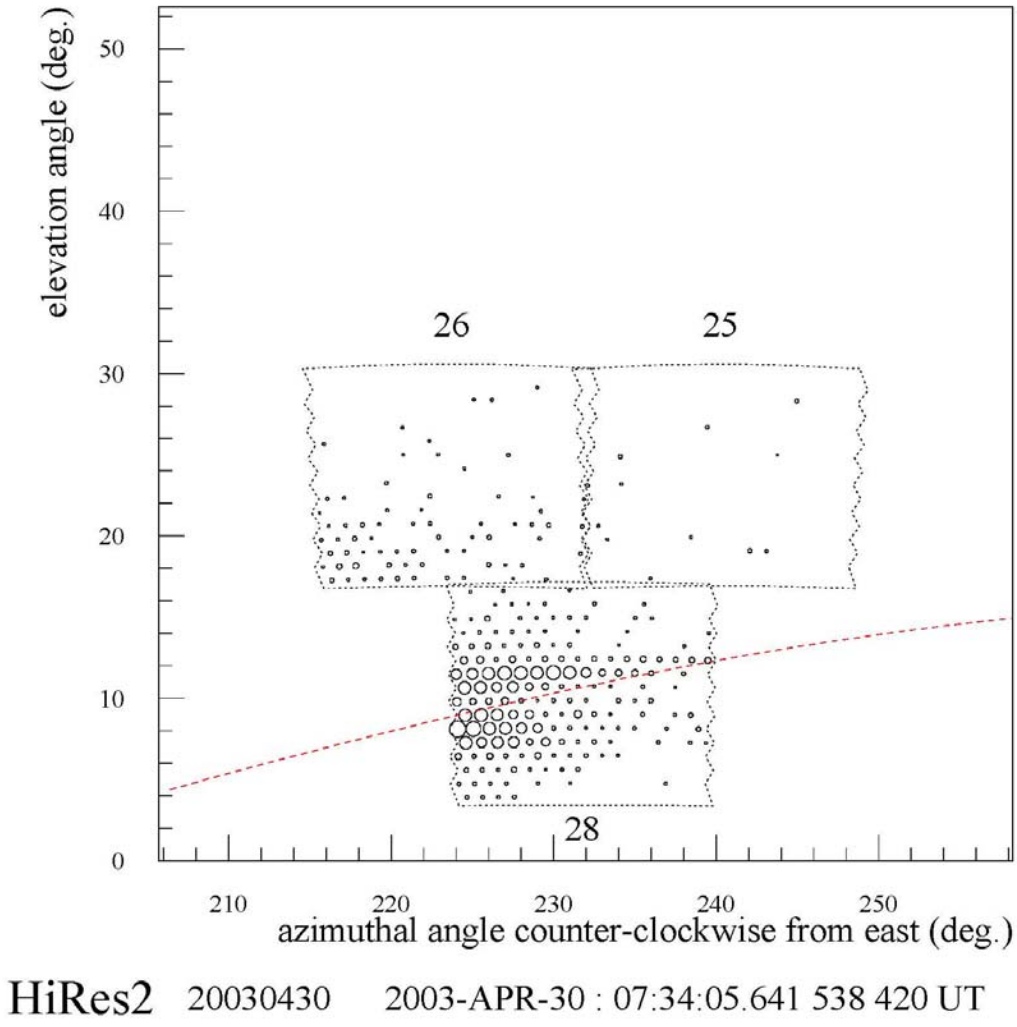

Figure 55: HiRes 2 display of possible noise event

Figure 55 had just enough correlation to survive the plog cut. It is important to note that these could possibly be real events. However, as was discussed when looking at the σ_{boot} cut, very wide events like this have a wide variation in the possible reconstructed speeds. By altering the plane for one or both detectors slightly, the event can be brought back in line with the speed of light. Because the event covers such a wide area, the plane would still pass through triggered tubes.

These factors make it very difficult to make any sort of reliable determination of the speed of the event. As such, these events were removed as possible candidates for exotic particle events. Given enough triggered tubes, the event could be fit to any speed desired. However, any cut performed visually is subject to human bias. For reference, Appendix C contains a listing of the important parameters for all events along with event displays of each.

April 6th, 2003 Event

Each of the events remaining at this point were examined very closely in an effort to understand the cause of their anomalous speeds. The event on April 6th, 2003 was the first event to go through this process and will be used as an example of the work done on each event.

The speed of the April 6th event reconstructed at 0.233 m/ns for HiRes 1 and 0.236 m/ns for HiRes 2. These speeds are just under 80% of the speed of light. The event passed the visual checks mentioned above. The event display is shown in Figure 56. It proved an ideal candidate for a possible exotic event. The first step in determining the validity of this and other events was to review the nightly logs by the operators of

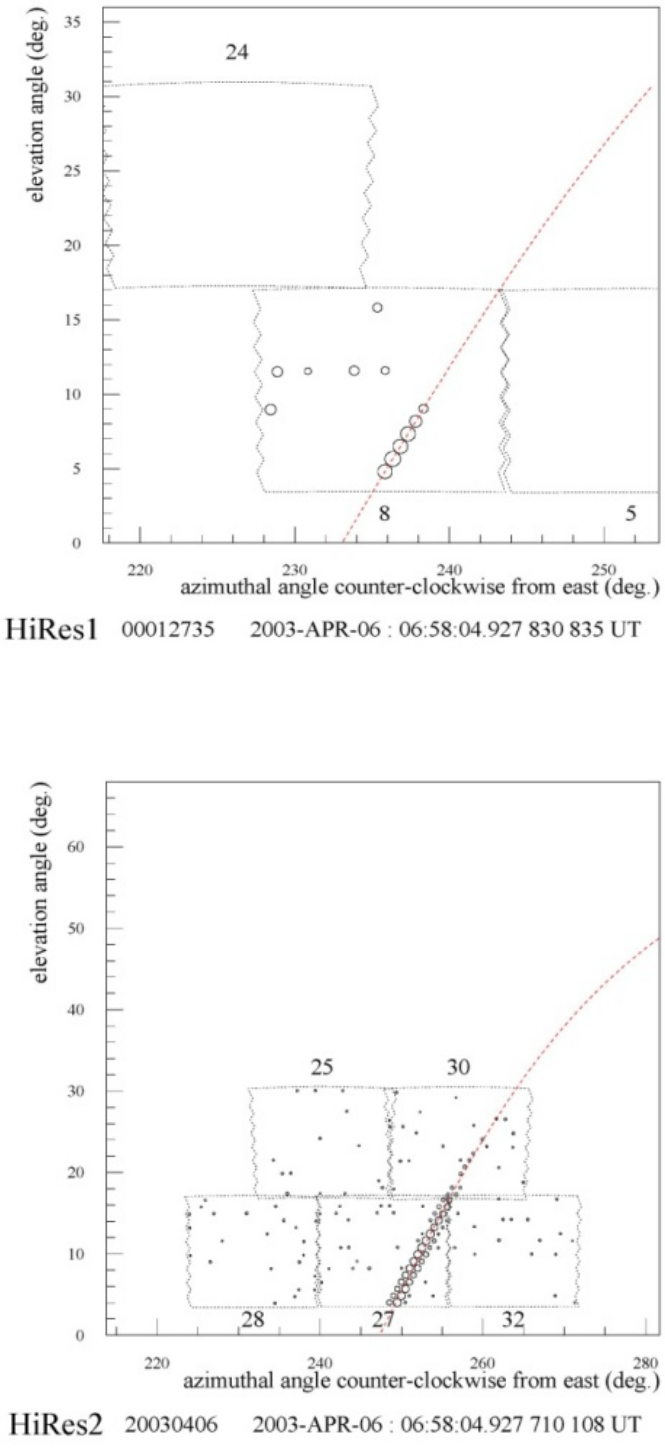

Figure 56: HiRes 1 and HiRes 2 event displays for April 6th, 2003 event

each site. Operators were instructed to make notes on the state of the detector and the weather in the area on a regular basis.

On this night, there was a small discrepancy between the HiRes 1 and HiRes 2 log files regarding the weather. However, the HiRes 2 runners reported clear skies at the recorded time of the event. In order to further ensure no problems existed in the weather, flasher events for the night were examined.

As detailed in Chapter II, flashers at set distances from the detectors fired on a regular basis. When the flasher hit a cloud, a visible blooming occurred in the event display. No such blooming was visible during the time of the April 6th, 2003 event. In addition, if a large amount of haze is present in the atmosphere, the more distant flashers would dim and ultimately fail to trigger the detector. Both haze and clouds can affect the scattering of light from the shower and therefore the reconstructed speed. For this particular event, no evidence of either effect was visible at the time of the event.

After determining there were no problems reported in the logs for the night in question, the event was subjected to a number of different fits to determine the speed of the event. First, a modified routine to calculate the location of the shower plane was implemented. This routine functioned by drawing a line along the viewing direction of each triggered tube. Points were located along each line at given intervals and then inversely weighted according to distance. A least squares fit was then used on the set of points to determine the best possible plane fit. This method is slightly different than that used in the HiRes reconstruction software, so it was used to see if any significant problems in the reconstruction's plane fitting routine could cause the anomalous speed.

Once the new plane was determined, it was inserted into the data and the speed analysis rerun. For this event, this process resulted in a new speed of 0.243 m/ns for HiRes 2. In this case, while the speed shifted slightly, the new speed was still significantly below the canonical speed of light.

In order to further examine possible causes for the abnormal speed of the event, the reconstruction was redone "by hand." Using Mathematica [35] only to ensure the numerical accuracy of individual calculations, the reconstruction was done starting with only the plane information and the timing information from the tubes. This reconstruction followed the basic process outlined in Chapters V and VI. The "by hand" reconstruction allowed for the results of each step of the process to be examined for possible inconsistencies. No major inconsistencies were noted. Once a set of corrected tube times and distances were calculated, two different fits were performed to determine the speed of the shower.

The first fit was a weighted least squared fit. The weights were given based on the number of photo electrons each tube recorded. For this event, it resulted in a speed of 0.241 m/ns. The second fit was an unweighted least squared fit. For this event, it resulted in a speed of 0.266 m/ns.

At this point, each tube was examined individually to see if the time could possibly be reported incorrectly. This was done by examining FADC traces. A few of the FADC traces for the April 6th event are shown in Figure 57. Each of the smaller graphs shows a reconstructed number of photo electrons vs. bin number (roughly equivalent to time from trigger) for a particular tube. The pedestal for each tube is given by the horizontal line in each graph. Two vertical lines bracket the event window that

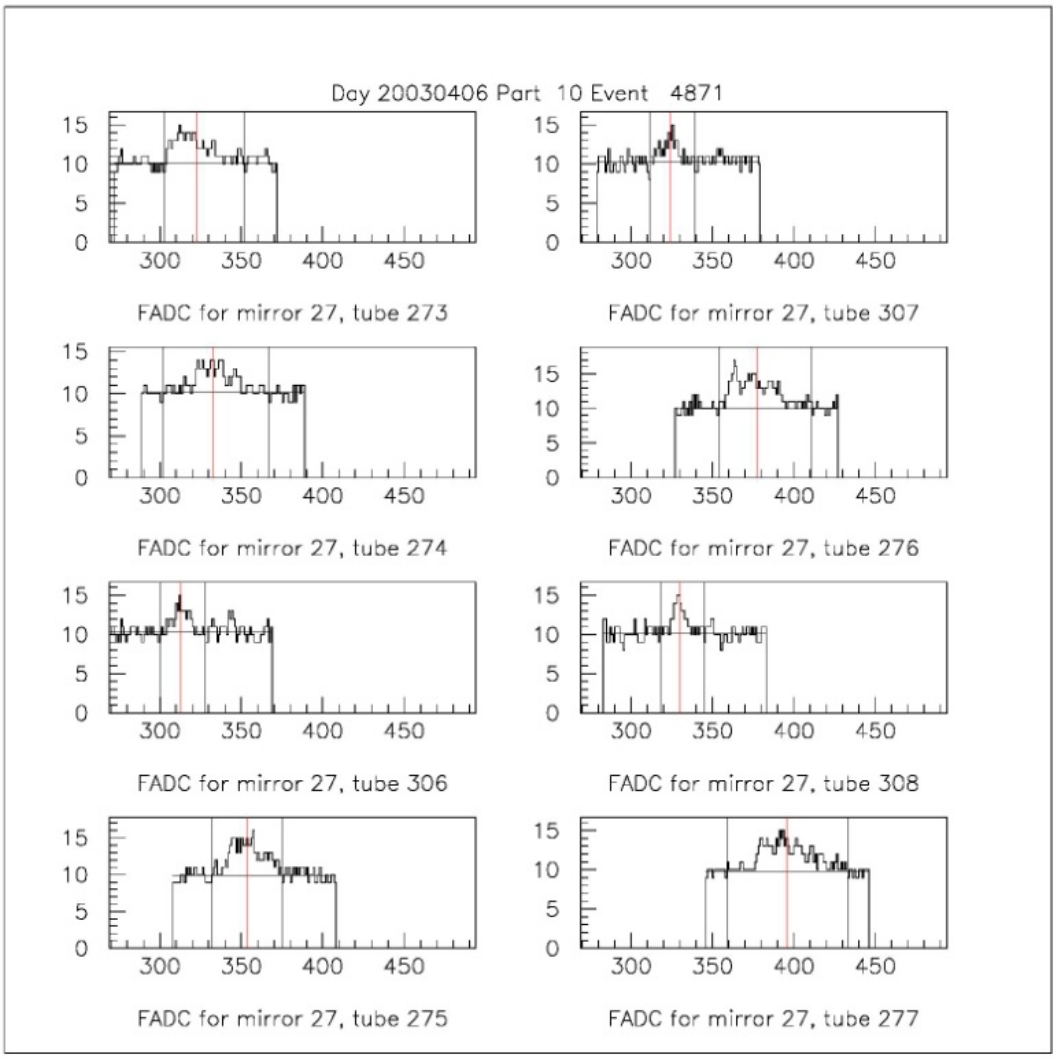

Figure 57: Sample FADC traces for April 6th, 2003 event

was used in determining the time of the event. The third line gives the peak location that was used as the trigger time for the tube.

Visually a bad fit would result in the peak location being shifted in respect to the actual peak of the signal. Figure 57 shows no obvious signs that the tube times were shifted in any systematic way.

The previous steps ruled out the most probable causes for errors in reconstruction. The next step was to examine the event itself for any indication of an abnormal event. Over the course of the experiment, several different reconstructions have been done. Several of these reconstructions were compared to see if any major differences appeared. Specifically, shower profiles were examined from the stereo reconstruction used [33], a monocular HiRes 1 reconstruction [28], and a monocular HiRes 2 reconstruction (publishing pending). In the case of this event, there was no monocular HiRes 1 reconstruction as a minimum of 8 tubes was required.

The HiRes 2 monocular fit assumes the speed of light in order to determine the distance of the shower from the detector. Examining this fit, it was noted that the $\overrightarrow{R_p}$ calculated in monocular reconstruction for HiRes 2 differed from that calculated in stereo reconstruction. As $\overrightarrow{R_p}$ is determined by crossing the two shower detector planes, the next step was to see if a similar $\overrightarrow{R_p}$ could be obtained from stereo reconstruction using small rotations of the detector planes.

Plane Rotation

The geometry of the shower is determined by intersecting two planes which are determined by fitting tubes triggered in an event. Because each tube looks at approximately 1 degree of sky, it is sometimes possible to alter these planes while still

crossing the triggered tubes. The exact amount by which a shower plane can be altered depends on the distance from the detector and the number of tubes crossed so must be calculated separately for each shower.

For this analysis, two different axes of rotation were chosen. Because of notation during derivation, they are referred to here as φ and θ. The φ rotation corresponds to a rotation about the line drawn from the weighted averaged center of all tube pointing directions to the shower by a given angle. When calculating the weighted averaged center, the tubes were weighted according to total signal in each tube. The θ rotation indicates a rotation of the plane about the z axis (in this case, located in the center of each detector).

When rotating the planes, the approach taken was to move the plane in small steps until the shower reconstructed with the correct speed, then output the results so they could be visually inspected.

First, the plane was rotated by a preset amount around the chosen axis. The details of how this rotation was performed are given in Appendix A. The new shower axis and $\overrightarrow{R_p}$ vectors were then calculated. These were fed back into the speed calculation routines. The resulting speed was compared to the original speed. If it was further away from the speed of light than before, the rotation was undone and tried in the opposite direction. If it was closer, the rotations continued in that direction. At any point, if the rotation caused the speed of the shower to "jump" the speed of light, the rotation was undone, the angle of rotation was reduced by a factor of 10, and the rotation tried again. This cycle was continued until either the program was able to match the speed of light or

the angle of rotation was small enough that further rotations would not significantly change the speed.

In total, four different rotations were performed: two on each of the detector planes. Each plane was rotated until the speed of the event reconstructed at near the speed of light. The resulting planes were then output for inspection. The post-rotation inspection was to determine if the new plane was consistent with the tubes triggered on the event display.

In the case of the April 6th event, it was possible to rotate the plane in a manner that allowed the speed to be near that of the speed of light while still being a reasonable plane fit. This was accomplished by rotating the HiRes 1 plane around a line between the mirror and the center of the shower. The resulting plane is shown in Figure 58. The resulting shower speed of this rotation was 0.301 m/ns. In the case of this event, it was determined that the event could still have been traveling at near the speed of light with the generated signal.

Attempts were made to determine the resolution of the detector to shower speed under similar rotations of planes. This is difficult to model for a number of reasons. As the number of tubes in a shower increases, the amount a plane can be rotated decreases improving resolution. As distance from the detector increases, small rotations have a larger effect on the geometry, also increasing resolution. Events near the detector tend to trigger a larger number of tubes, decreasing resolution. The exact relation between all of these factors makes it very difficult to model the behavior of shower speed under rotation of the shower detector plane. Instead, it proved more productive to simply analyze each shower individually using this transformation

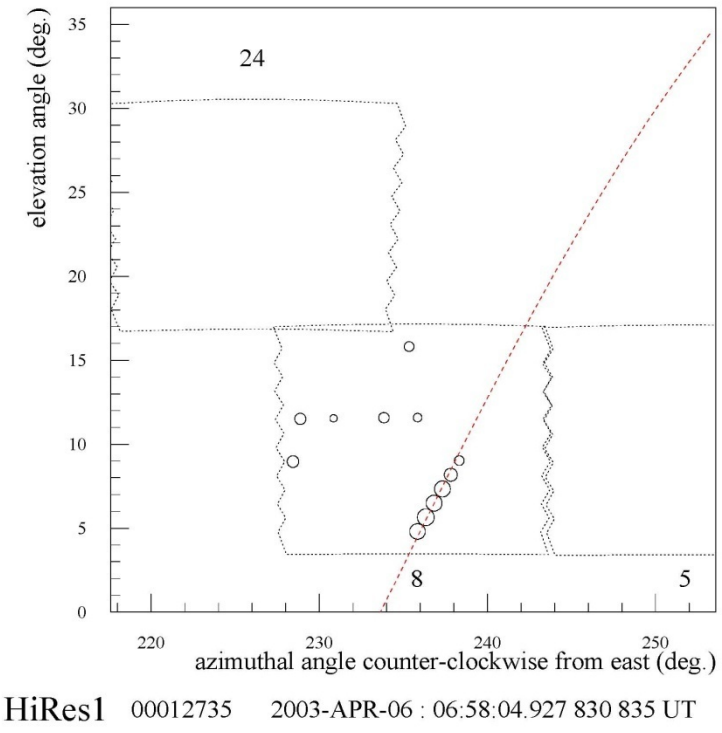

Figure 58: Rotated HiRes 1 plane resulting in shower speed of .301 m/ns

Each of the candidate events were subjected to a process similar to that used on this event. The results are shown in detail in Appendix D.

CHAPTER XI

RESULTS

Anomalous Events

All anomalous events found could be explained through one of the checks described in Chapter X. A list of each event, the calculated speed, and the explanation for this speed is provided in Appendix D.

We are therefore left with no real anomalous candidates. The absence of candidate anomalous events in the HiRes data set allows for an upper limit for such events in the cosmic ray flux to be calculated given some basic physical assumptions. Keys among these assumptions are that the shower develops in a fashion similar enough to a hadronic shower that the HiRes detector can observe them and that candidate events have speeds that differ sufficiently from the speed of normal showers to allow detection.

Using Poisson statistics, the probability of exactly k occurrences during an interval where λ events were expected can be calculated using Equation 49 [36].

$$f(k;\lambda) = \frac{\lambda^{k} e^{-\lambda}}{k!} \tag{49}$$

In this case, there were 0 occurrences. Substituting this in as k and solving for λ gives the number of expected events for any given probability. For example, assuming a

95% chance of having recorded zero events during a set period, the number of expected events is 3. Table 11 summarizes the number of events from some common confidence limits. This number of events can then be used to calculate the flux. Before this can be done, the sensitivity of the detector to these events must be calculated.

Aperture Calculations

As described above, there are several assumptions that must be made when performing this type of search. First, the method of interaction with the atmosphere would need to result in secondary showers that produced measurable fluorescence light. All results from this thesis must be interpreted with this assumption in mind. The null result can be used to limit the types of interaction models that can be used if a large flux of these particles is present.

The second assumption is that the candidate events need to have velocities that differ enough from the speed of a normal event to be distinguishable. The Monte Carlo work described in Chapter VIII was used to determine the resolution of the detector. For this work, a separation of 3 RMS from the speed of light was used as the minimum separation for a possible candidate. Assuming a roughly Gaussian distribution, this corresponds to a 99.5% confidence level.

To set an upper limit to the possible flux, it is necessary to calculate the aperture

Table 11: Number of expected events for various confidence percentages with 0 recorded events assuming Poisson statistics

Confidence Percentage	Events
90	2.3
95	3.0
99	4.6

of the detector given these assumptions. This calculation can be represented by Equation 50[33].

$$\left\langle A\Omega\left(s,E_i\right)\right\rangle = \int dAd\Omega\,\eta(s,E_i,\theta,\phi) = \left\langle \eta(s,E_i)\right\rangle \int_0^{2\pi} d\varphi \int_0^{R_p\max} rdr \int_0^{2\pi} d\phi \int_0^{\pi/2} \sin\theta d\theta \tag{50}$$

Here, $dA$is the area over which the cosmic ray flux is measured, $d\Omega$ the solid angle, and $\eta(s,E_i,\theta,\phi)$ a function describing the rate of acceptance of events at given energies, speeds, and angles. This density is dependent on both azimuthal and zenith angles as well as the speed of the shower and energy of the event. This integral is evaluated using the standard Monte Carlo method described below.

First, the average $\left\langle \eta(s,E_i)\right\rangle$ was calculated using Monte Carlo. As this is just the average rate of acceptance at a given energy, it can be found by taking the ratio of the number of accepted events to the number of thrown events. This process is akin to using a sampling method to do the actual integral. The result is shown in Equation 51.

$$\left\langle \eta(s,E_i)\right\rangle = \frac{N_{reconstructed}(s,E_i)}{N_{thrown}(s,E_i)} \tag{51}$$

As noted in the equation, the number of reconstructed events is dependent on both the speed and the Energy of the events.

To calculate the aperture then requires a "sufficient" amount of Monte Carlo thrown at different energies and different speeds. "Sufficient" in this case is a result of two considerations. The first consideration is statistical significance. The process of

sampling by counting refers to drawing n elements from a population and accepting only those with a given characteristic. In this case, this process accepts only events that meet the criteria of the cuts explained in Chapter VIII. This method of sampling corresponds to sampling from a binomial distribution.

To estimate the error for this type of sampling, one starts with the maximum likelihood estimator given by Equation 52.

$$S(p) = \frac{k}{n} \tag{52}$$

Here, *k* refers to the number of accepted events while *n* refers to the number thrown. The variance of the distribution is then given by Equation 53.

$$\sigma^2(S(p)) = \frac{p(1-p)}{n} \tag{53}$$

The error is then defined as the square root of $S(np)$. Combining Equations 52 and 53 and taking the square root results with this definition results in a measure for the error given by Equation 54.

$$\partial k = \sqrt{k\left(1-\frac{k}{n}\right)} \tag{54}$$

The second consideration was the amount of time required to generate the Monte Carlo. As can be seen from the formula above, in the limit k << n, the error roughly follows $\sqrt{k}$. The result of this is that to reduce the error by a factor of 10 requires an increase in the number accepted by a factor of 100. In other words, the processing time for samples increased rapidly based on desired accuracy.

After a number of trials, it was determined that approximately 30,000 events thrown led to an acceptable error with acceptable processing time.[2] These samples of 30,000 events per speed and energy bin were used in the Monte Carlo portion of the integration. In total, ~1,680,000 events were generated for this purpose.

By integrating the latter part of the integral shown in Equation 45 over 360° of azimuth and 90° zenith, the integral can be fully evaluated. This also requires integrating over the maximum radial distance of a shower. This distance $R_{p\max}$ is dependent on both the speed of the shower and the energy. The result is shown in Equation 55.

$$\left\langle A\Omega\left(s, E_i\right)\right\rangle = \left\langle \eta(s, E_i)\right\rangle 2\pi^2 {R_{p\max}}^2 \tag{55}$$

This equation is used to calculate the aperture of the detector for a given speed and energy.

The HiRes detector starts to trigger on events at energies greater than approximately $10^{17.5}$ eV. Because of this, the energy bins were chosen in half decade energies starting at $10^{18.5}$ eV and continuing up to 10^{20} eV. At each energy range, a set of Monte Carlo was

[2] As an example, for this number of events a single speed at 10^{20} eV took just over 3 days to run while producing ~1000 accepted events. As 7 speeds for 2 different types of particles were run, this resulted in ~1.4 months processing time for just this energy decade with a ∂k of ~31 events or 3.1%.

generated at speeds of 0.050 m/ns, 0.100 m/ns, 0.150 m/ns, 0.200 m/ns, 0.299 m/ns, 0.400 m/ns, and 0.600 m/ns. Each set of Monte Carlo consisted of approximately 30,000 thrown events with R_p allowed to vary between 0 and 40 km.

The ratio of reconstructed to thrown events was then calculated for each set of Monte Carlo. This was used with Equation 55 to calculate the aperture at various speeds and energies. The results of these calculations are shown in plots Figure 59, Figure 60, Figure 61, and Figure 62. These plots show the aperture of proton and iron Monte Carlo events (respectively) plotted against the energy with which they were thrown. On each plot, apertures are included for the range of speeds tested.

There are a couple of features worth noting. First, out of the ~30,000 events thrown in each set, no events with energies of $10^{18.5}$ eV passed through both the reconstruction and all of the cuts. For proton events, a small number did make it through the process for speeds of 0.200 m/ns, 0.299 m/ns, and 0.400 m/ns. Second, with no exception, the maximum aperture is found for events with speeds of 0.299 m/ns. This corresponds with the canonical speed of light. The aperture then decreases as events move away from this speed.

Flux Limit

Once the aperture is calculated, the expected number of particles per time viewed by the HiRes detector can then be calculated. This calculation is given by Equation 56.

$$J_{ul} = \frac{N}{t \cdot \left\langle A\Omega\left(s, E_i\right)\right\rangle} \tag{56}$$

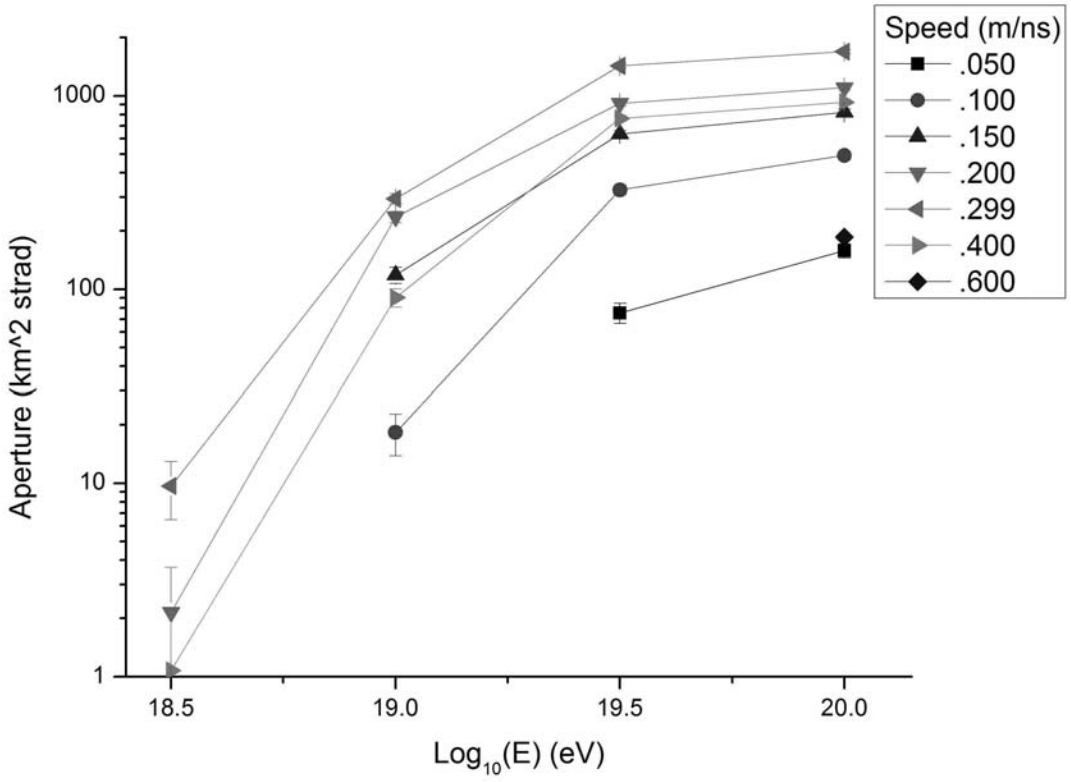

Figure 59: Aperture calculated for Proton events thrown at various speeds plotted against energy of thrown events.

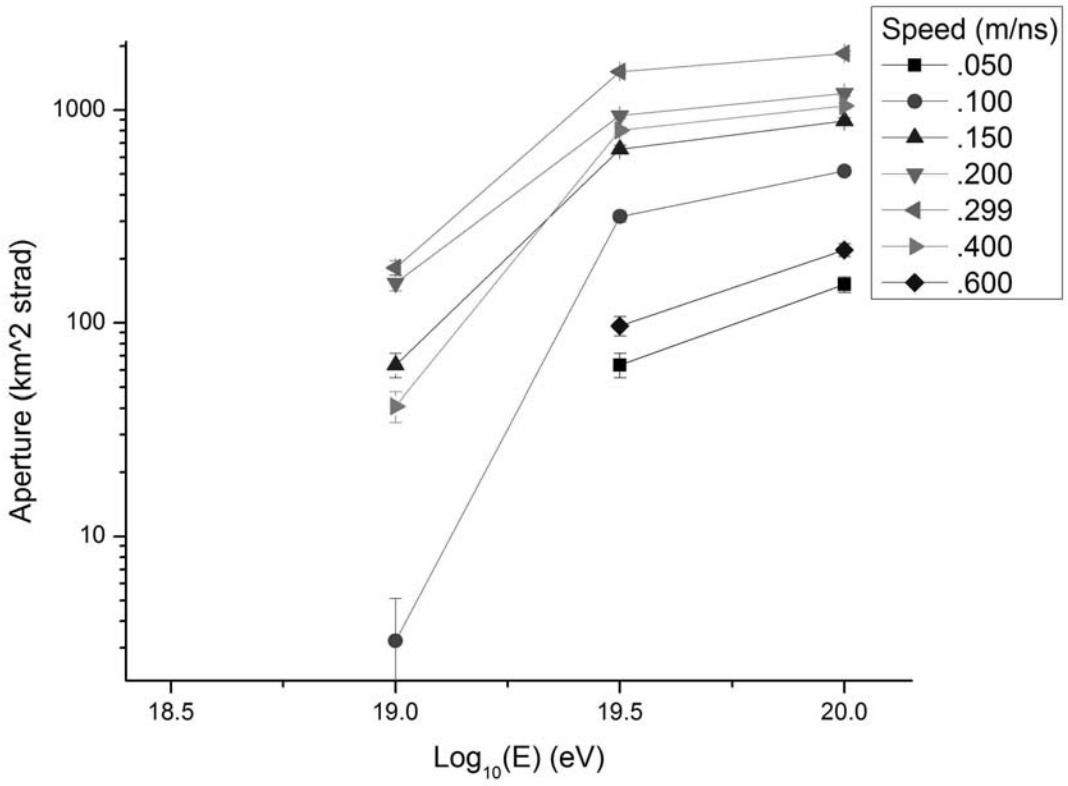

Figure 60: Aperture calculated for Iron events thrown at various speeds plotted against energy of thrown events.

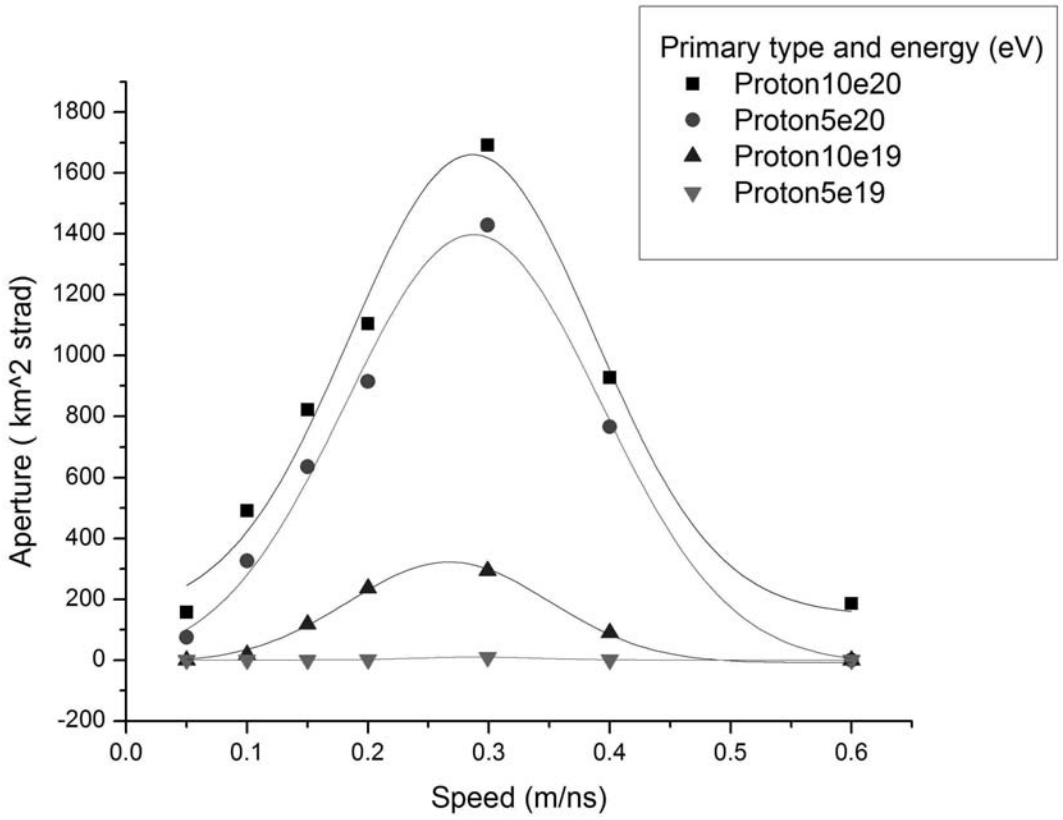

Figure 61 : Aperture vs. Speed for Proton events thrown at different energies

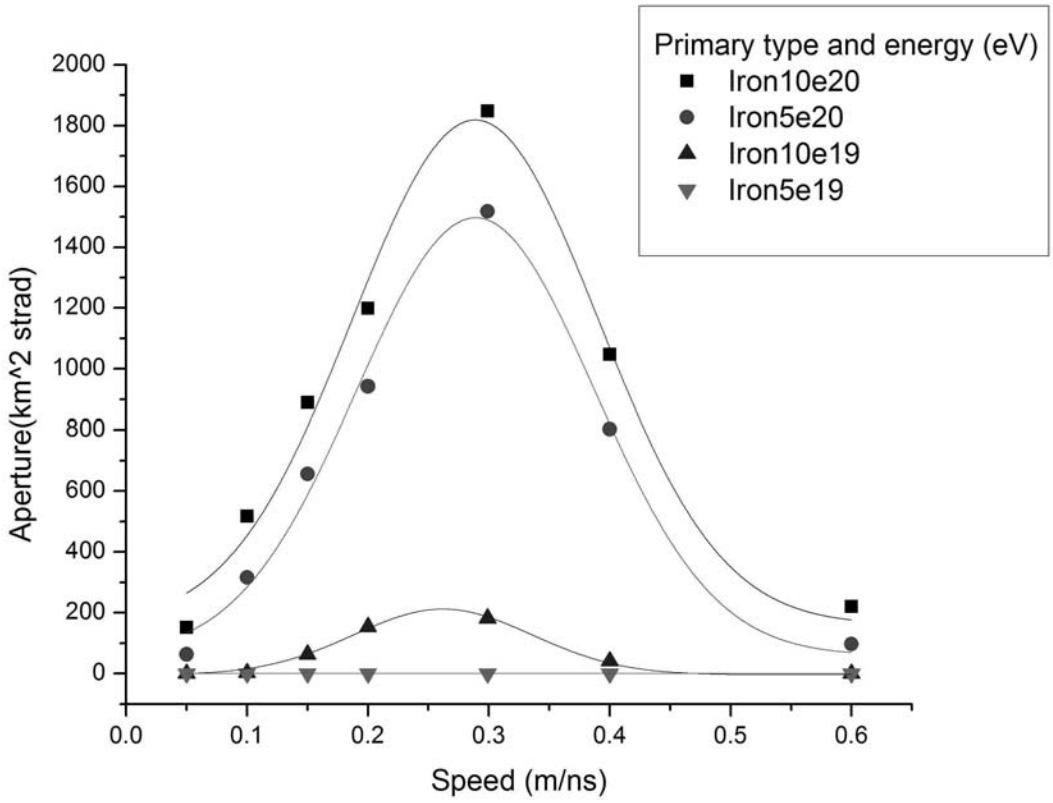

Figure 62 : Aperture vs. Speed for Iron events thrown at different energies.

This provides an upper limit to the possible flux given the assumptions mentioned earlier. In this formula, N is the upper limit on expected particles given 0 seen calculated using Poisson statistics, $\langle A\Omega(s, E_i)\rangle$ is the calculated aperture, and t is the amount of time the detector was operational. As mentioned several times previously, this only includes the months between December of 1999 and November of 2005. While the HiRes detector operated into 2006, calibration data was not present at the time this work was done. The total time the detector ran (ontime) for this period was calculated to be 3460.1 hours. This time was used to determine the flux.

Conclusions

No events which could not be explained through standard means were found in the HiRes data set. Preliminary upper limits to the flux were calculated. A summary is given in Table 12. Plots of the upper limits are shown in Figure 63 and Figure 64.

Table 12: Summary of upper limits calculated for Flux assuming 95% confidence of a 0 event result.

Log(E)	18.5		19		19.5		20	
eV	Proton $m^{-2}sr^{-1}s^{-1}$	Iron $m^{-2}sr^{-1}s^{-1}$	Proton $m^{-2}sr^{-1}s^{-1}$	Iron $m^{-2}sr^{-1}s^{-1}$	Proton $m^{-2}sr^{-1}s^{-1}$	Iron $m^{-2}sr^{-1}s^{-1}$	Proton $m^{-2}sr^{-1}s^{-1}$	Iron $m^{-2}sr^{-1}s^{-1}$
Speed (m/ns)								
.050	--	--	--	--	3.20E-15	3.79E-15	1.52E-15	1.59E-15
.100	--	--	1.32E-14	7.46E-14	7.39E-16	7.61E-16	4.90E-16	4.65E-16
.150	--	--	2.03E-15	3.79E-15	3.79E-16	3.67E-16	2.93E-16	2.71E-16
.200	1.12E-13	--	1.02E-15	1.57E-15	2.63E-16	2.56E-16	2.18E-16	2.01E-16
.299	2.49E-14	--	8.20E-16	1.32E-15	1.69E-16	1.59E-16	1.42E-16	1.30E-16
.400	2.24E-13	--	2.66E-15	5.89E-15	3.15E-16	3.00E-16	2.60E-16	2.30E-16
.600	--	--	--	--	--	2.49E-15	1.52E-15	1.09E-15

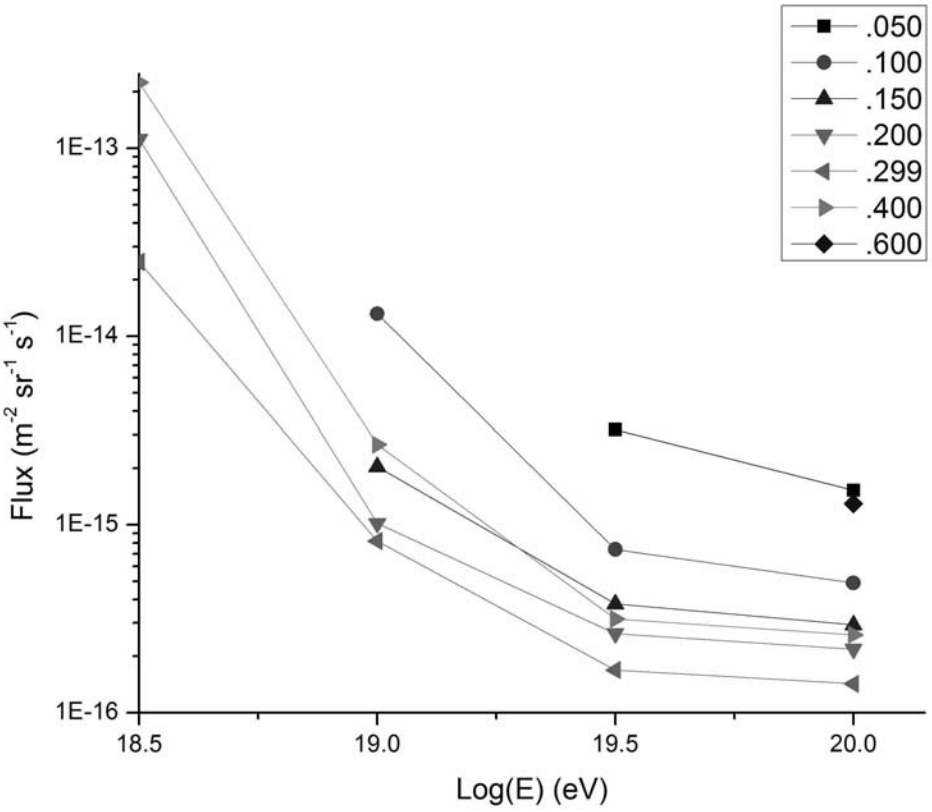

Figure 63 : Calculated flux for apertures shown in Figure 59 for Proton events assuming 95% confidence.

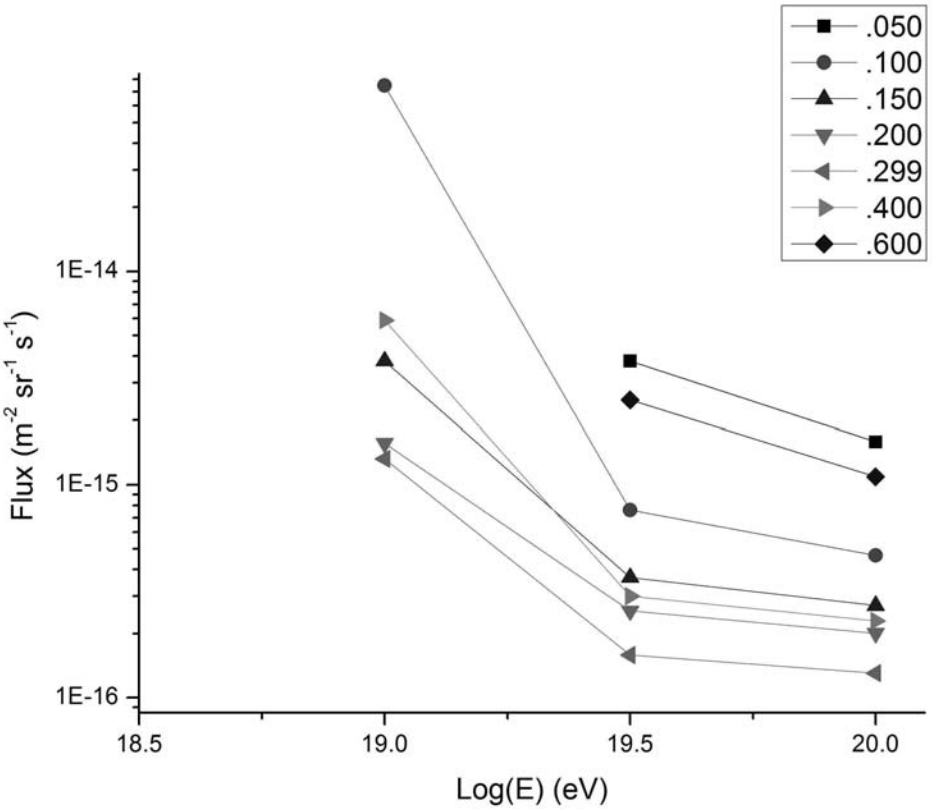

Figure 64: Calculated flux for apertures shown in Figure 60 for Iron events assuming 95% confidence.

APPENDIX A

GENERALIZED ROTATION MATRIX

A plane can be completely described by a unit normal vector and a point on the plane. For work with HiRes, the shower-detector (SD) plane was fit assuming it passed through the center of the detector site. Using this as the pivot point reduces the problem of rotating SD planes to a transformation around an arbitrary axis. This transformation is applied in two parts. The first is a translation of the axis to a coordinate axis. The second is a rotation about that axis.

To perform the rotational part of the transformation, the familiar Euler rotation matrices can be used. These can be expressed as shown in Equations 57, 58, and 59.

$$R_z(\alpha) = \begin{pmatrix} \cos\alpha & \sin\alpha & 0 \\ -\sin\alpha & \cos\alpha & 0 \\ 0 & 0 & 1 \end{pmatrix} \tag{57}$$

$$R_y(\beta) = \begin{pmatrix} \cos\beta & 0 & -\sin\beta \\ 0 & 1 & 0 \\ \sin\beta & 0 & \cos\beta \end{pmatrix} \tag{58}$$

$$R_z(\gamma) = \begin{pmatrix} \cos\gamma & \sin\gamma & 0 \\ -\sin\gamma & \cos\gamma & 0 \\ 0 & 0 & 1 \end{pmatrix} \tag{59}$$

An arbitrary rotation is then be given by Equation 60 [37].

$$A(\alpha,\beta,\gamma) = R_z(\gamma)R_y(\beta)R_z(\alpha) =$$

$$\begin{pmatrix} \cos\gamma\cos\beta\cos\alpha - \sin\gamma\sin\alpha & \cos\gamma\cos\beta\cos\alpha + \sin\gamma\cos\alpha & -\cos\gamma\sin\beta \\ -\sin\gamma\cos\beta\cos\alpha - \cos\gamma\sin\alpha & -\sin\gamma\cos\beta\cos\alpha + \cos\gamma\cos\alpha & \sin\gamma\sin\beta \\ \sin\beta\cos\alpha & \sin\beta\sin\alpha & \cos\beta \end{pmatrix} \tag{60}$$

For this work, the translation is done using homogeneous coordinates. Homogeneous coordinates allow for affine transformations to be represented as a distinct matrix [38]. They are frequently used in computer graphics to allow translations to be written in matrix form. This allows for modern computer graphics cards optimized for vector processing to quickly rotate and translate objects for rendering by allowing a single matrix calculation to include both the translation and the rotation. For this work, a number of different transformations needed to be tried for each event. Borrowing this method from computer graphics allowed for the large number of transformations needed for each event to be done very quickly. More complete explanations of homogeneous coordinates can be found in other sources [38, 39]; a brief explanation of how they relate to this transformation is included below.

Homogeneous coordinates allow the translation of a point $P = (a, b, c)$ to the origin to be written as Equation 61.

$$T_o = \begin{pmatrix} 1 & 0 & 0 & -a \\ 0 & 1 & 0 & -b \\ 0 & 0 & 1 & -c \\ 0 & 0 & 0 & 1 \end{pmatrix} \tag{61}$$

At this point, by representing Equation 60 in homogeneous coordinates and multiplying the correct rotation and translation matrices, a rotation around any arbitrary axis can be specified. To make the result representative of what would be found in computer text books, it is first necessary to write down the rotation of the vector $\vec{v} = \{u, v, w\}$ first into the xz plane. One way of visualizing this rotation is rotating a 3d object such that it lay in the 2D plane of a computer screen. The vector is then rotated onto the z axis. These two rotations are given by Equations 62 and 63.

$$R_{xz} = \begin{pmatrix} u/\sqrt{u^2+v^2} & v/\sqrt{u^2+v^2} & 0 & 0 \\ -v/\sqrt{u^2+v^2} & u/\sqrt{u^2+v^2} & 0 & 0 \\ 0 & 0 & 1 & 0 \\ 0 & 0 & 0 & 1 \end{pmatrix} \tag{62}$$

$$R_{xz2z} = \begin{pmatrix} w/\sqrt{u^2+v^2+w^2} & 0 & -\sqrt{u^2+v^2}/\sqrt{u^2+v^2+w^2} & 0 \\ 0 & 1 & 0 & 0 \\ \sqrt{u^2+v^2}/\sqrt{u^2+v^2+w^2} & 0 & w/\sqrt{u^2+v^2+w^2} & 0 \\ 0 & 0 & 0 & 1 \end{pmatrix} \tag{63}$$

With these matrices defined, it is possible to perform a rotation about an arbitrary axis as follows. First, a transformation of the axis to the origin is specified. Assuming the axis can be specified by two points $P_1 = (a, b, c)$ and $P_2 = (d, e, f)$ then the axis of rotation can be defined as $\vec{v} = \{u, v, w\} = P_2 - P_1$. A rotation of angle θ about this line can then by done by translating the point to be rotated to P_1, rotating the resultant vector to the xz plane and then to the z axis. This is followed by a rotation through angle θ about the z axis, and finally the inversion of the rotations and the translation. This is

shown in Equation 64 along with the matrix representing the rotation. The substitution $l = \sqrt{u^2 + v^2 + w^2}$ was used to simplify the representation of this matrix.

$$RT(\theta) = T_0^{-1}R_{xz}^{-1}R_{xz2z}^{-1}R_z(\theta)R_{xz2z}R_{xz}T_0 =$$

$$\begin{pmatrix} \frac{u^2 + (v^2 + w^2)\cos\theta}{u^2 + v^2 + w^2} & \frac{uv(1 - \cos\theta) - wl\sin\theta}{u^2 + v^2 + w^2} & \frac{uw(1 - \cos\theta) - vl\sin\theta}{u^2 + v^2 + w^2} \\ \frac{uv(1 - \cos\theta) + wl\sin\theta}{u^2 + v^2 + w^2} & \frac{v^2 + (u^2 + w^2)\cos\theta}{u^2 + v^2 + w^2} & \frac{uw(1 - \cos\theta) - ul\sin\theta}{u^2 + v^2 + w^2} \\ \frac{uw(1 - \cos\theta) - vl\sin\theta}{u^2 + v^2 + w^2} & \frac{vw(1 - \cos\theta) + ul\sin\theta}{u^2 + v^2 + w^2} & \frac{w^2 + (u^2 + v^2)\cos\theta}{u^2 + v^2 + w^2} \\ 0 & 0 & 0 \end{pmatrix} \tag{64}$$

$$\begin{pmatrix} \frac{a(v^2 + w^2) - u(bv + cw) + (u(bv + cw) - a(v^2 + w^2)\cos(\theta) + (bw - cv)lsin(\theta)}{u^2 + v^2 + w^2} \\ \frac{b(u^2 + w^2) - v(au + cw) + \big(v(au + cw) - b(u^2 + w^2)\big)\cos(\theta) + (cu - aw)lsin(\theta)}{u^2 + v^2 + w^2} \\ \frac{c(u^2 + v^2) - w(au + bv) + \big(w(au + bv) - c(u^2 + v^2)\big)\cos(\theta) + (av - bu)lsin(\theta)}{u^2 + v^2 + w^2} \\ 1 \end{pmatrix}$$

Visually, the process can be illustrated by rotating the plane with normal vector $\vec{n} = (0,1,1)$ through an angle of -45° about the x axis. By quick inspection, such a rotation should map this normal vector onto the z axis. This is shown graphically in Figure 64. Figure 64 (a) shows the plane before any transformations are applied. To define the axis of rotation (i.e., the x axis), the points $P_1 = (1,0,0)$ and $P_2 = (0,0,0)$ are chosen. The axis of rotation is then represented by $\vec{v} = \{1,0,0\}$. The translation matrix given in 56 is then given as shown in Equation 65.

$$T_o = \begin{pmatrix} 1 & 0 & 0 & -1 \\ 0 & 1 & 0 & 0 \\ 0 & 0 & 1 & 0 \\ 0 & 0 & 0 & 1 \end{pmatrix} \tag{65}$$

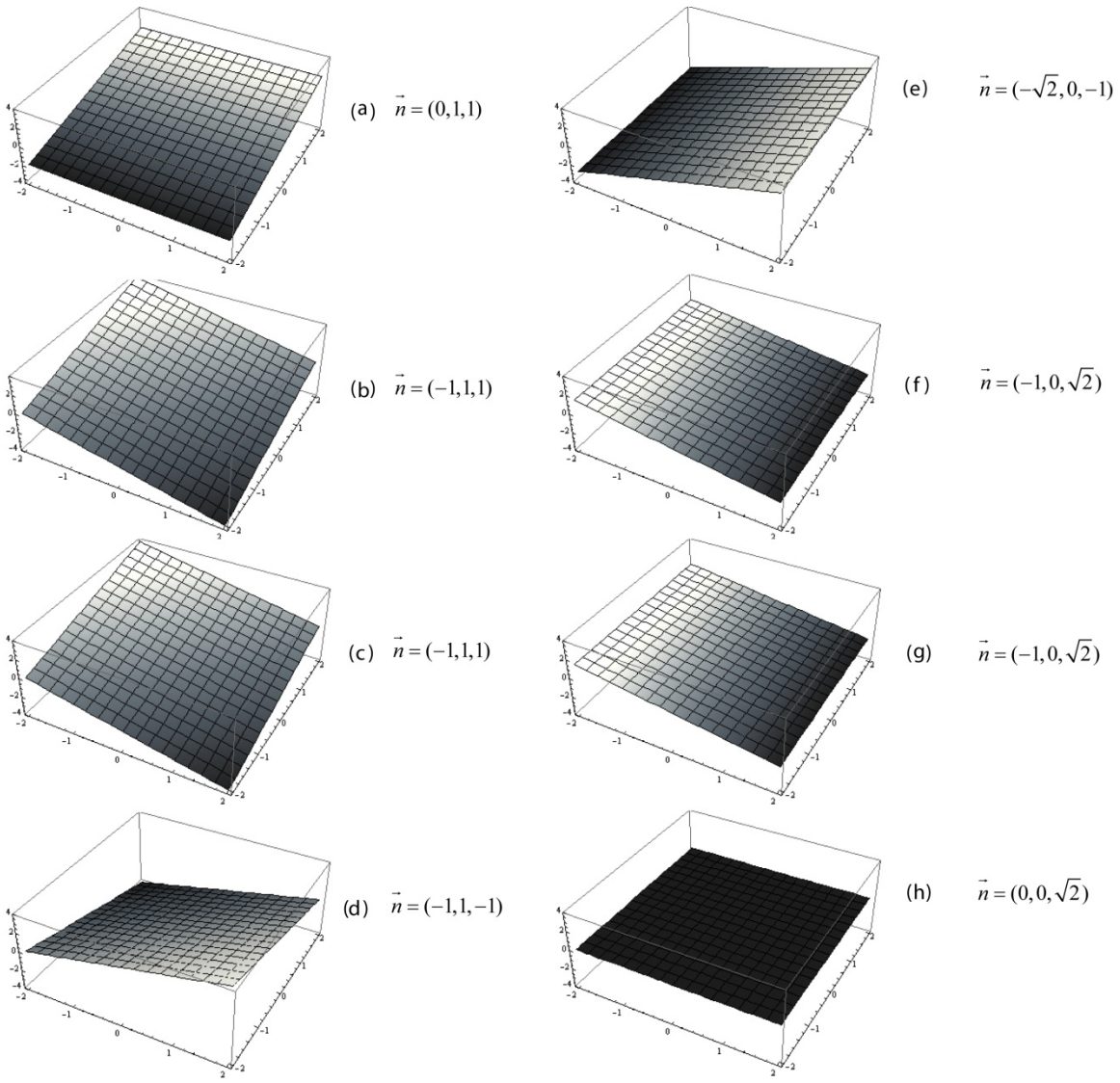

Figure 64: Rotation steps for plane defined by $\vec{n} = (0,1,1)$ by -45° about the x axis. Plot a represents the plane before `any transformations are applied. Plot b after the translation T_0 is applied. Plot c after rotation R_{xz}, Plot d after rotation R_{xz2z}, Plot e after rotation $R_z(\theta)$, Plot f after rotation R_{xz2z}^{-1}, Plot g after rotation R_{xz}^{-1}, and Plot h after translation T_0^{-1}.

The result of this transformation is shown in Figure 64 (b). The next step in the transformation corresponds to a shift into the xz plane. In this case, Equation 62 shows that the corresponding transformation matrix to be just the identity operator. Figure 64(c) confirms that there is no change to $\vec{n}$.

At this point, it is useful to pause the discussion of the example to note an important computational detail. Examining Equation 59, a rotation about the z axis would have resulted in division by 0 instead of the identity matrix. It should be noted that Equation 64 does not share this problem. The avoidance of such artificial coordinate singularities is the primary use for the use of homogeneous coordinates in this thesis.

The next rotation R_{xz2z} is given in Equation 66 for this example.

$$R_{xz2z} = \begin{pmatrix} 0 & 0 & -1 & 0 \\ 0 & 1 & 0 & 0 \\ 1 & 0 & 0 & 0 \\ 0 & 0 & 0 & 1 \end{pmatrix} \tag{66}$$

The result of applying this rotation can be seen in Figure 64 (d). Using the angle of rotation and 60 in homogeneous coordinates gives Equation 67.

$$R_z(\theta) = \begin{pmatrix} \frac{1}{\sqrt{2}} & -\frac{1}{\sqrt{2}} & 0 & 0 \\ \frac{1}{\sqrt{2}} & \frac{1}{\sqrt{2}} & 0 & 0 \\ 0 & 0 & 1 & 0 \\ 0 & 0 & 0 & 1 \end{pmatrix} \tag{67}$$

Applying $R_z(\theta)$ to the plane results in Figure 64 (e). Figure 64 (f) shows the result of the inverse rotation R_{xz2z}^{-1}. Figure 67 (g) shows the result of the inverse rotation R_{xz}^{-1},

and Figure 64 (h) shows the result of the inverse translation T_0^{-1}. The result is the plane rotated so that the normal vector $\vec{n}$ is along the z axis. The normalization is preserved in the rotation.

The same result can be achieved in one step using Equation 60. Inserting the appropriate numbers into Equation 60 results in Equation 68.

$$RT(-45^{\circ}) = \begin{pmatrix} 1 & 0 & 0 & 0 \\ 0 & \frac{1}{\sqrt{2}} & -\frac{1}{\sqrt{2}} & 0 \\ 0 & \frac{1}{\sqrt{2}} & \frac{1}{\sqrt{2}} & 0 \\ 0 & 0 & 0 & 1 \end{pmatrix} \tag{68}$$

Using the homogeneous form of the original plane normal vector $\overrightarrow{n_h} = (0,1,1,1)$, it can be quickly verified that $RT(-45^{\circ}).\overrightarrow{n_h} = (0,0,\sqrt{2},1)$. Extracting the rotated normal vector back into 3D space gives the same result as the string of rotations. This reduces a series of seven individual transformations to a single matrix multiplication. While this example was chosen for its simplicity, the process works for any arbitrary axis of rotation. This allows for the axis of rotation to be chosen at run time, and Equation 59 is computed in a straight forward numeric fashion and is used for all rotations.

APPENDIX B

DERIVATION OF DISTANCE OF POINT FROM A LINE (EQUATION 39)

Assume a line given by Equation 69 and a point given by Equation 70.

$$s = s_0 + m * t \tag{69}$$

$$(t_0, b_0) \tag{70}$$

From geometry, the shortest distance between a point and a line is the length of a line segment drawn from the point to the line such that the line segment and the line are perpendicular. Using point-slope form, the line perpendicular to Equation 69 is written as shown in Equation 71.

$$y = -\frac{1}{m} * (t - t_0) + b_0 \tag{71}$$

The point of intersection between these two lines is found by setting them equal and solving for t and y. The result is given in Equation 72.

$$t = \frac{t_0 + mb_0 - ms_0}{m^2 + 1} \tag{72a}$$

$$y = \frac{mt_0 + m^2 b_0 + b}{m^2 + 1} \tag{72b}$$

Once the point of intersection is known, the distance is found using Equation 73.

$$\delta = \sqrt{(t - t_0)^2 + (y - b_0)^2} = \sqrt{(\frac{t_0 + mb_0 - ms_0}{m^2 + 1} - t_0)^2 + (\frac{mt_0 + m^2 b_0 + s_0}{m^2 + 1} - b_0)^2} \tag{73}$$

Expanding both the squared terms and simplifying results in Equation 74.

$$\delta = \sqrt{\frac{(s_0 + mt_0 - b_0)^2}{1 + m^2}} \tag{74}$$

APPENDIX C

CUTS STUDIED BUT NOT USED FOR THIS ANALYSIS

Each figure will receive just a brief explanation. Figure 65 shows the speed of the shower vs. the maximum number of tubes in any one mirror. Because wide events were problematic to fit, this test was to see if a cut could be made on the tubes in one mirror. There is no pattern as evidenced by the slope of the linear fit, also included in the graph.

Figure 66 shows the speed of the shower vs. the number of good tubes found after a fit. As the reconstruction gets more good tubes to fit, the shower detector plane and hence overall geometry should be more accurate. While the effect is seen to a small amount, the amount is negligible over 4 tubes. Four tubes is the minimum number used to accept a good event in the data set, hence there is no meaningful cut that can be made on the number of good tubes.

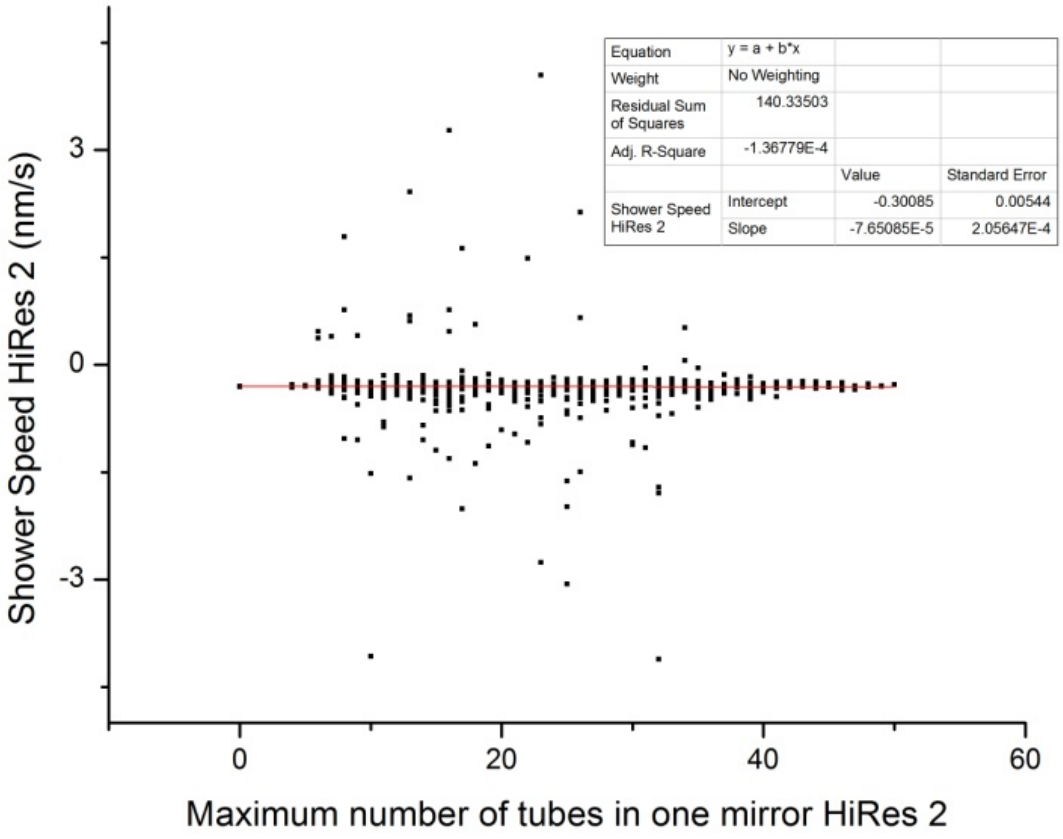

Figure 65: Shower Speed vs. Max Number of Tubes in HiRes 2 Mirror

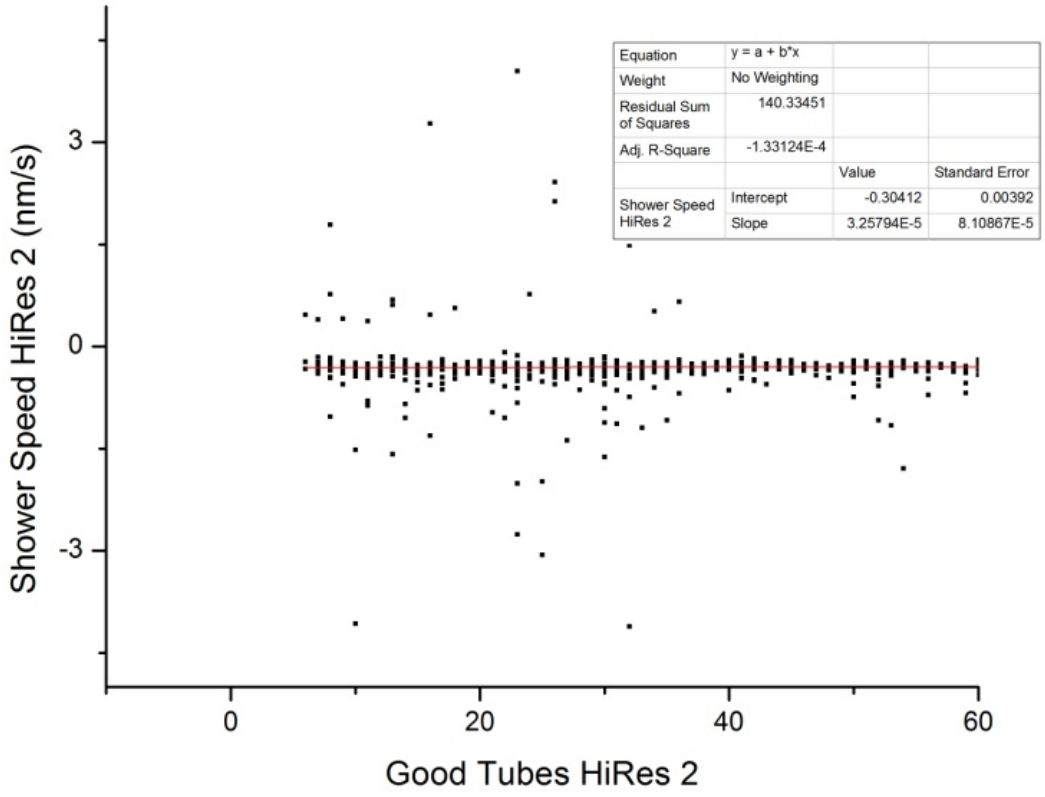

Figure 66: Shower Speed vs. Good Tubes at HiRes 2

Figure 67 shows the shower speed vs. the mean distance from the line determined by the fit. The scale of the graph at first suggests there may be a bunching at low distances. However, the effect is small enough that no good cut can be made.

Figure 68 shows the shower speed vs. the duration of the shower in ns. Short, fast showers can be the result of showers seen at very high angles or few tubes firing. The minimum number of tubes allowed by the reconstruction takes care of any large effect. While there is a trend, that trend is small as illustrated by the slope of the line fit to this data. Given the nature of the trend, a good cut could not be made on duration of the shower.

Figure 69 shows the shower speed vs. the standard deviation of the distance from the line of each point. The calculation was shown in the section discussing methods. As with the mean distance from the line, showers with large standard deviations should be wide showers. As wide showers are harder to fit, the expected trend would be that as the standard deviation grows larger, so does the error in the speed. However, a fit with a straight line shows that this effect is not noticeable in the actual data.

Figure 70 shows the shower speed vs. the track length of HiRes 2 in radians. Each tube in HiRes 2 subtends approximately a 1 degree cone of the sky. The shorter the track length in radians, the less the likelyhood of reconstructing a good shower detector plane. The line fit to the data shows a negligable slope. The slope of the line is also in the wrong direction for this effect. Any cut made on track length in radians large enough to remove points that did not reconstruct well also removed a large amount of data.

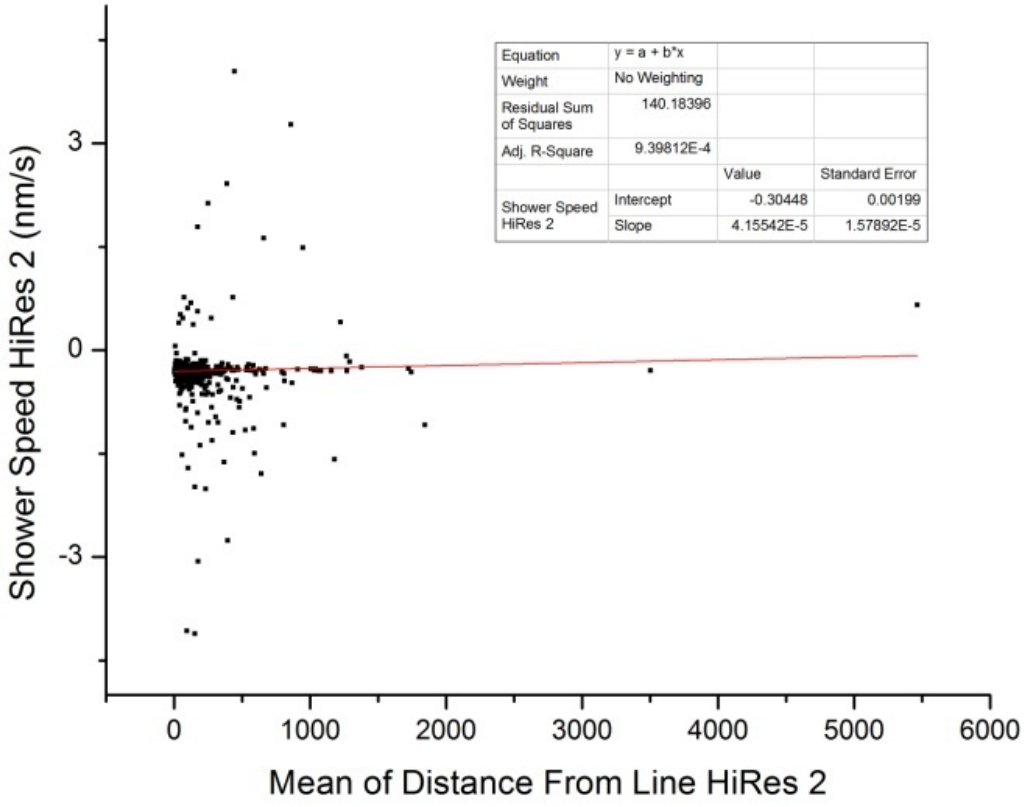

Figure 67: Shower Speed vs. Mean Distance from Calculated Fit for HiRes 2

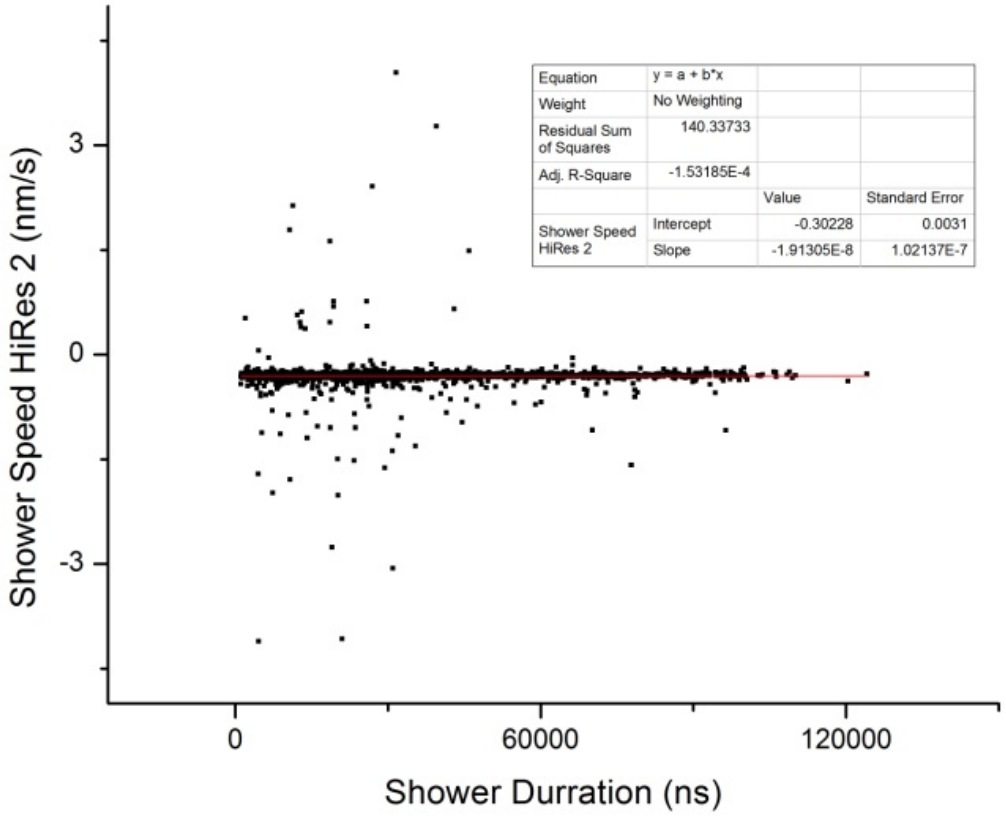

Figure 68: Shower Speed vs. Shower Duration in ns

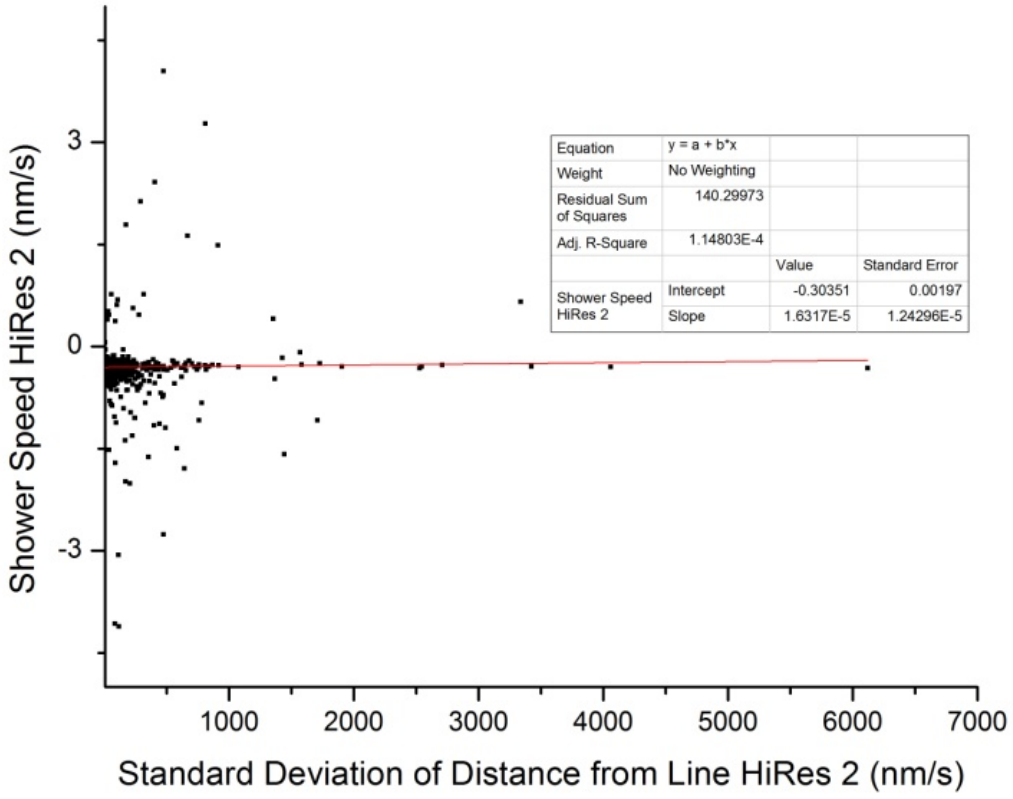

Figure 69: Shower Speed vs. Standard Deviation from fit for HiRes 2

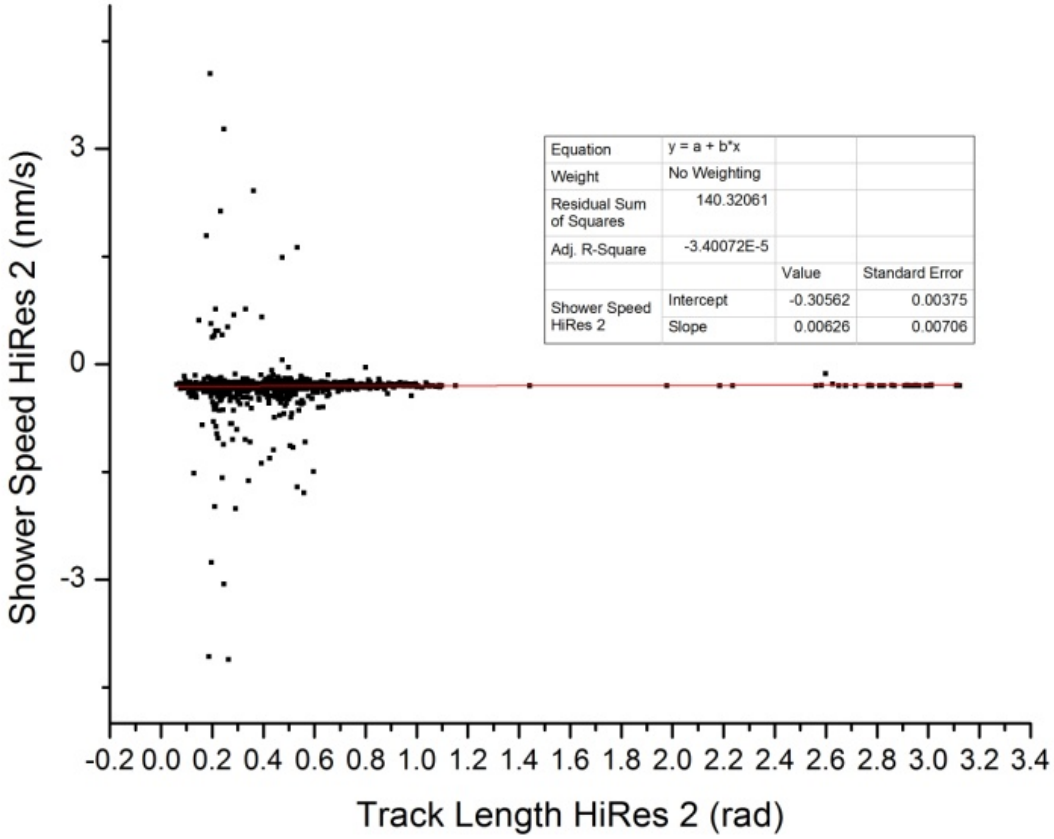

Figure 70: Shower Speed vs. Track Length for HiRes 2

APPENDIX D

SUMMARY OF ABNORMAL EVENTS

Events Removed by Visual Inspection

In total, 4 events were removed from consideration for the reasons specified at the start of Chapter X. These events are shown in Figures 71 through 73. The event shown in Figure 75 was removed as it did not have a definite shape on which to base a speed result.

The events shown in Figures 72 – 74 were all removed because of shower detector plane fitting issues. In the case of the events shown in Figures 72 and 74, it was possible to adjust the planes back onto the shower and recalculate the speed. The resulting shower detector plane fits are shown in each figure. For both of these events, once the shower detector planes were adjusted, the events reconstructed within one RMS of the speed of light. The event shown in Figure 77 did not pass the plane rotation procedure due to its location between the detectors.

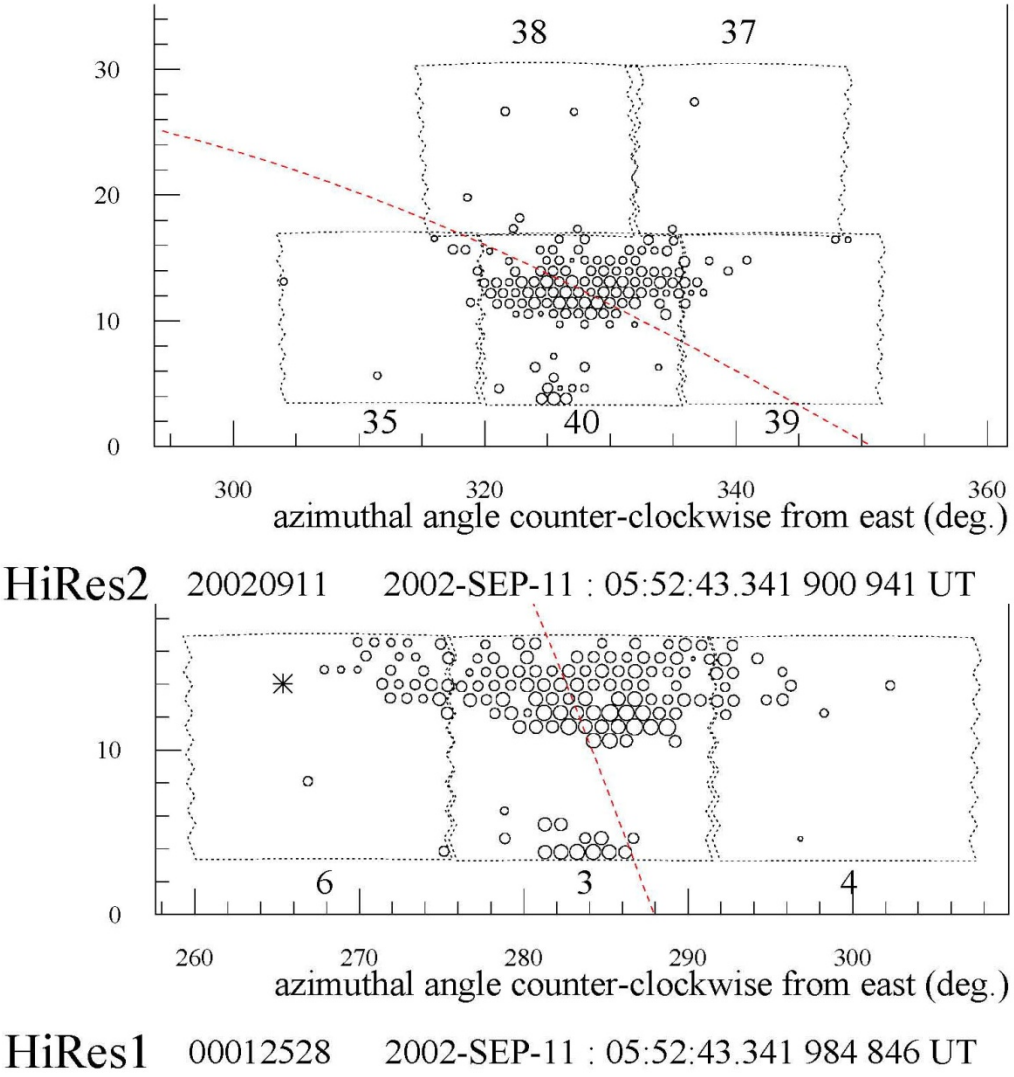

Figure 71: Event Removed by Eye Cut for lack of clear structure

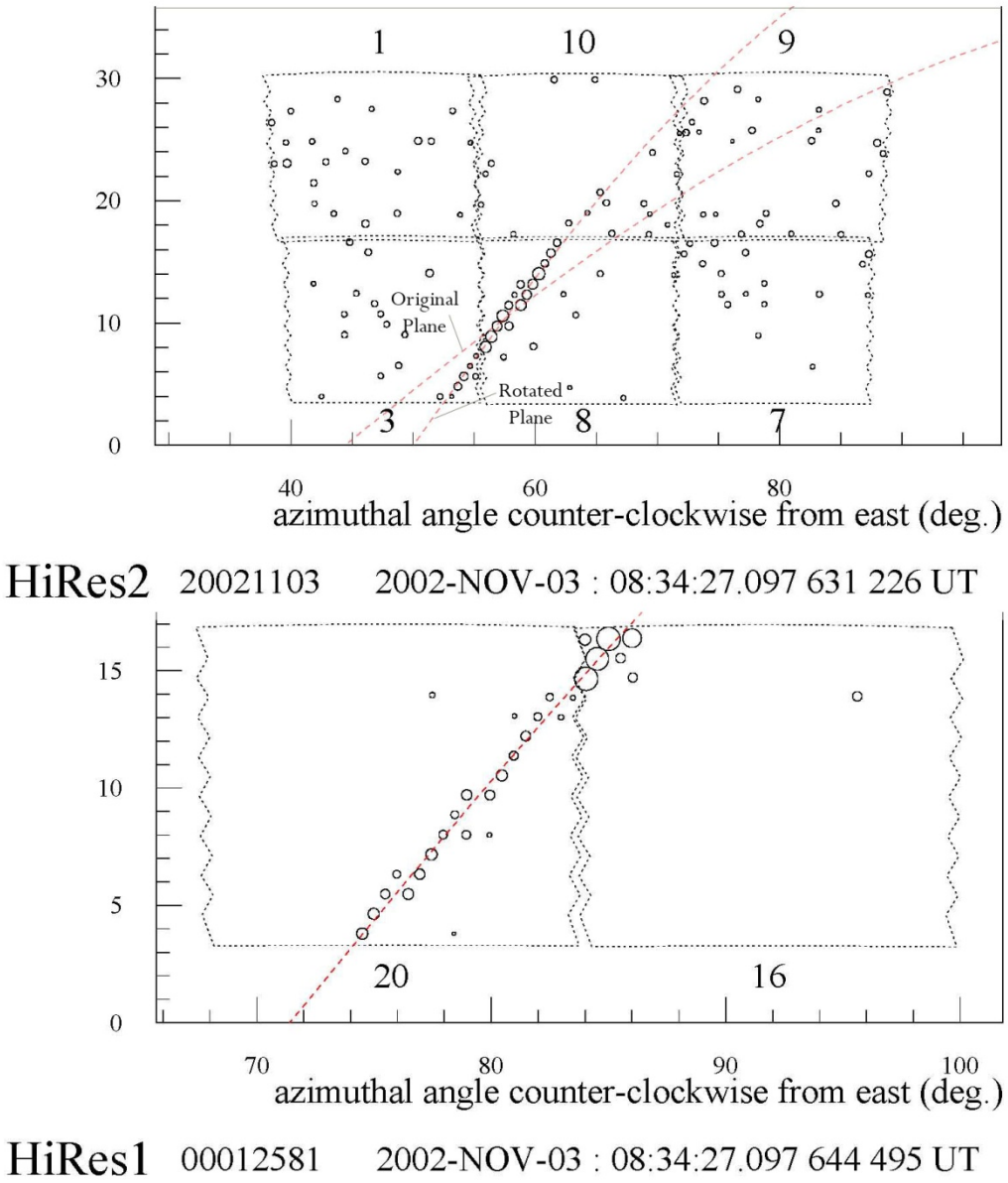

Figure 72: Event Removed by Eye Cut for poor plane fit. Rotated plane is shown for HiRes 2. This resulted in speeds of 0.291 m/ns for HiRes 1 and 0.300 m/ns for HiRes 2.

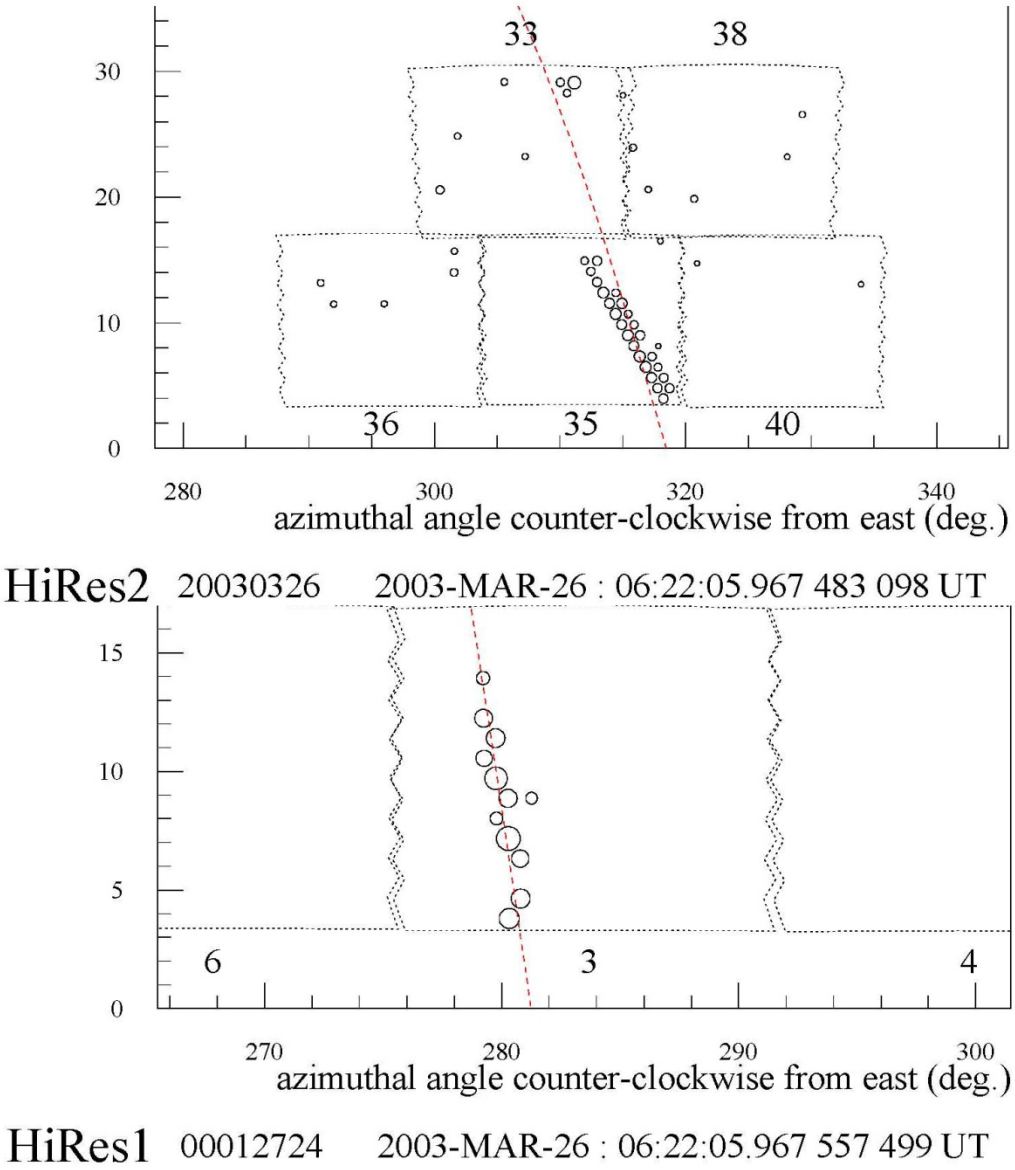

Figure 73: Event Removed by Eye Cut for poor plane fit. Event failed plane rotation due to location between detectors.

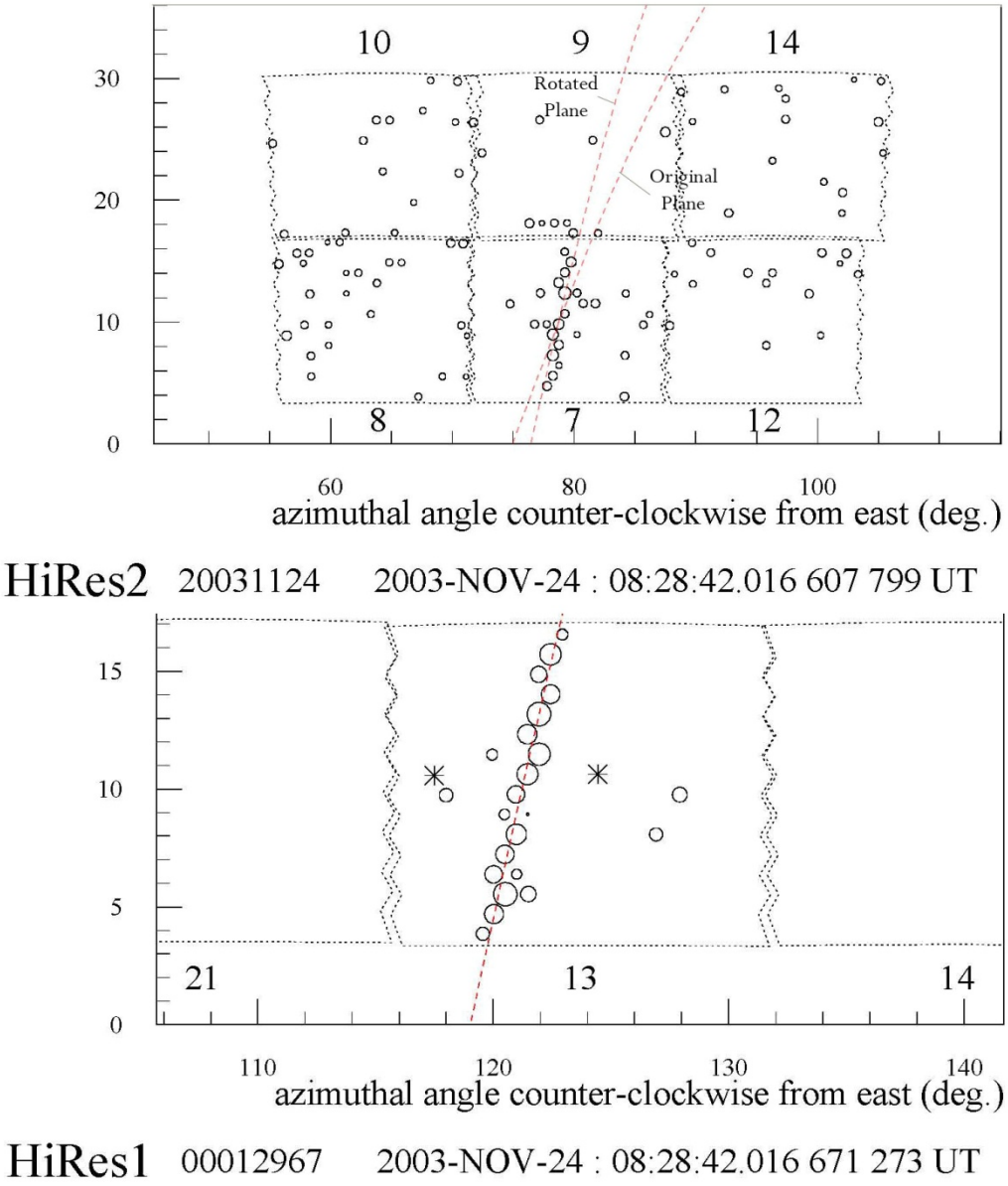

Figure 74: Event Removed by Eye Cut for poor plane fit. Rotated plane is shown for HiRes 2. This resulted in speeds of 0.284 m/ns for HiRes 1 and 0.293 m/ns for HiRes 2.

Events Removed by Plane Rotation

In addition to the events removed for obvious defects in plane fitting, there were six additional events whose speed could be explained by rotating their respective shower detector planes until a speed match was found with the speed of light. These events are summarized in Table 13. The rotated planes that resulted in the speeds shown in the fourth and fifth column of Table 13 are shown in Figures 75 through 80. The table notes the corresponding figures for each day.

Table 13 : Summary of events matched by plane rotation

Event Day	Hr1 Speed pre-rotation	Hr2 Speed pre-rotation	Hr1 Speed post-rotation	Hr1 Speed post-rotation	Figures
Jun 6th, 2002	-0.270 m/ns	-0.264 m/ns	-0.293 m/ns	-0.277 m/ns	75
Jan 5th, 2003	-0.324 m/ns	-0.330 m/ns	-0.295 m/ns	-0.288 m/ns	76
Feb 3rd, 2003	-0.337 m/ns	-0.333 m/ns	-0.297 m/ns	-0.304 m/ns	77
Apr 6th, 2003	-0.231 m/ns	-0.237 m/ns	-0.302 m/ns	-0.296 m/ns	78
Nov 28th, 2003	-0.246 m/ns	-0.244 m/ns	-0.305 m/ns	-0.297 m/ns	79
Dec 17th, 2003	-0.353 m/ns	-0.356 m/ns	-0.287 m/ns	-0.290 m/ns	80

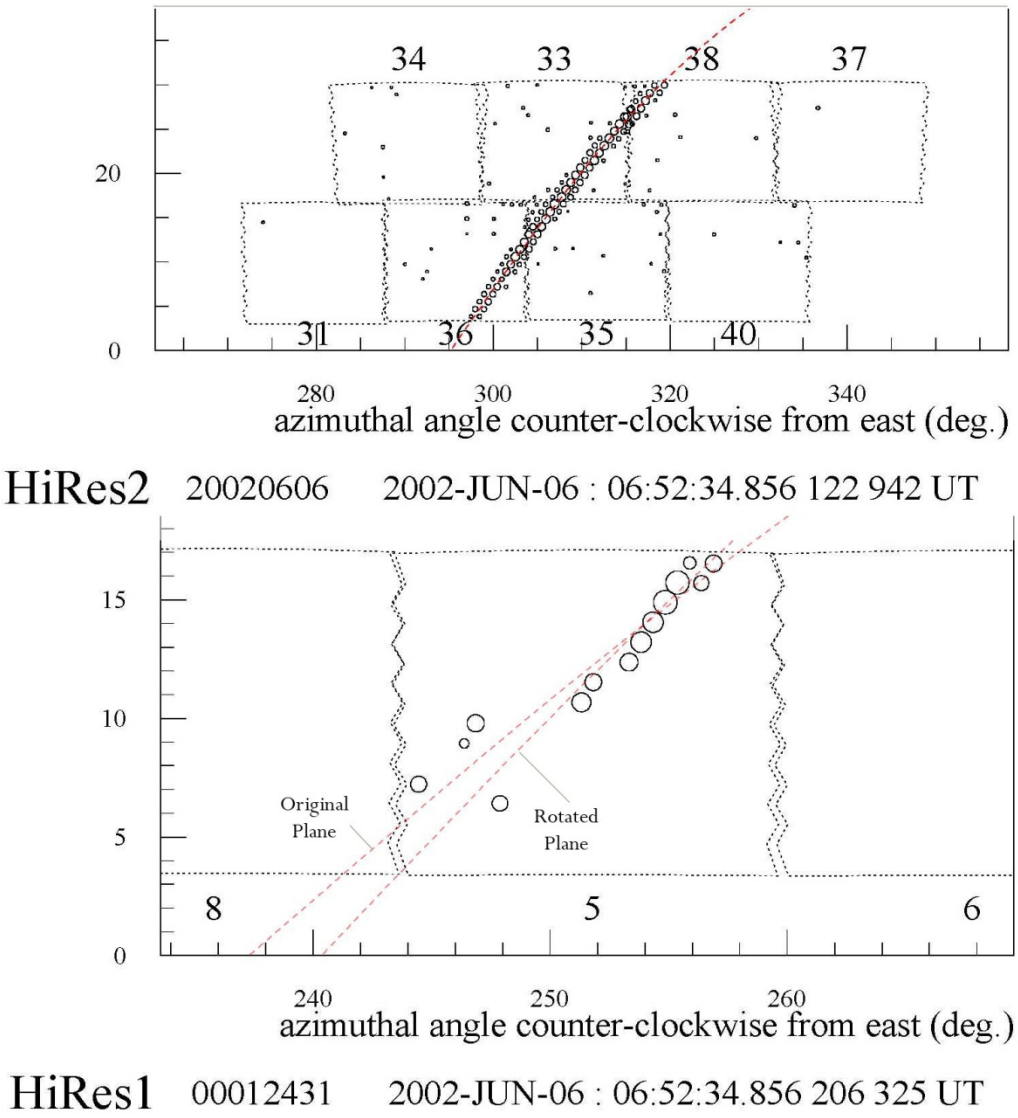

Figure 75: Event Display for event removed by plane rotation. See Table 13.

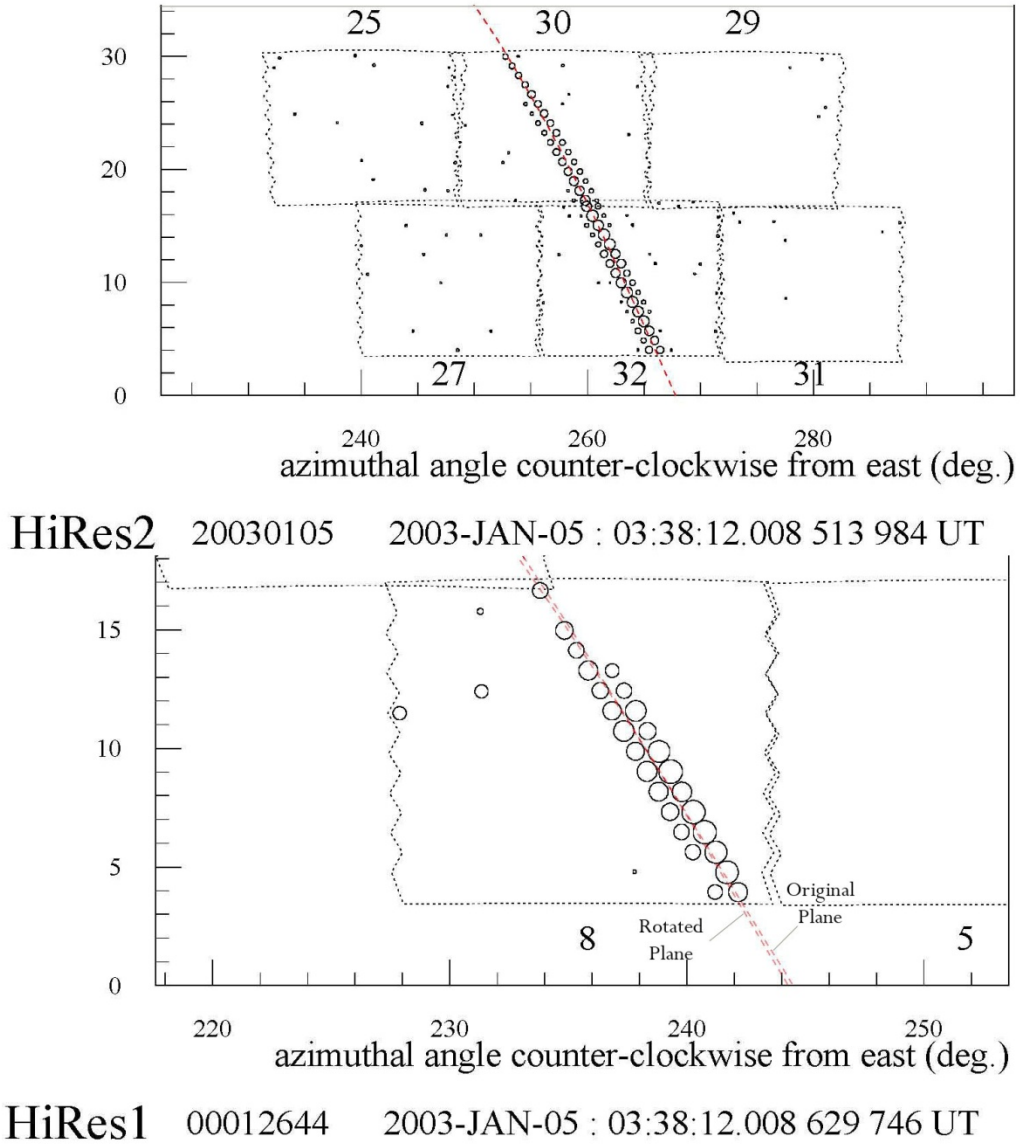

Figure 76: Event Display for event removed by plane rotation. See Table 13.

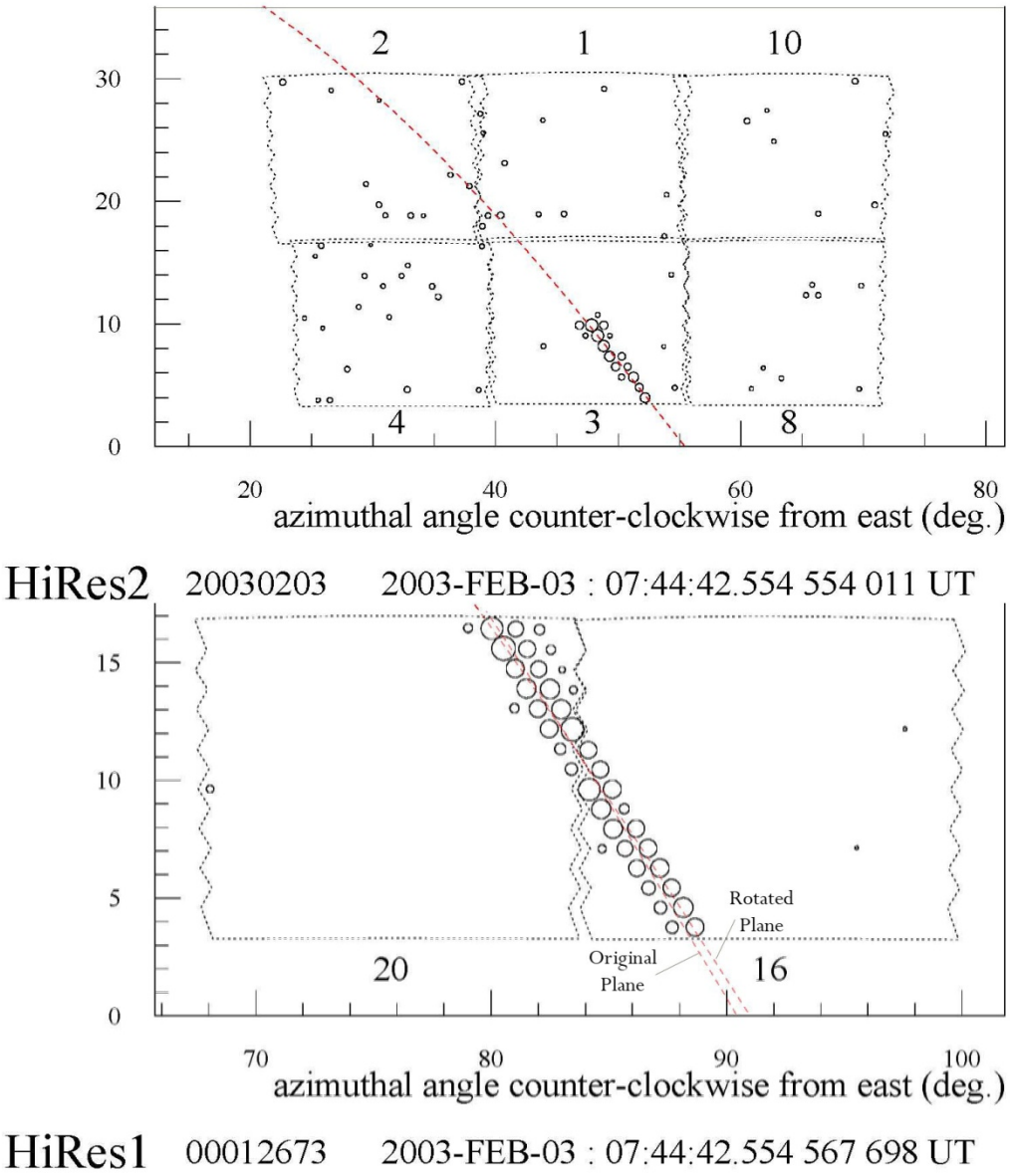

Figure 77: Event Display for event removed by plane rotation. See Table 13.

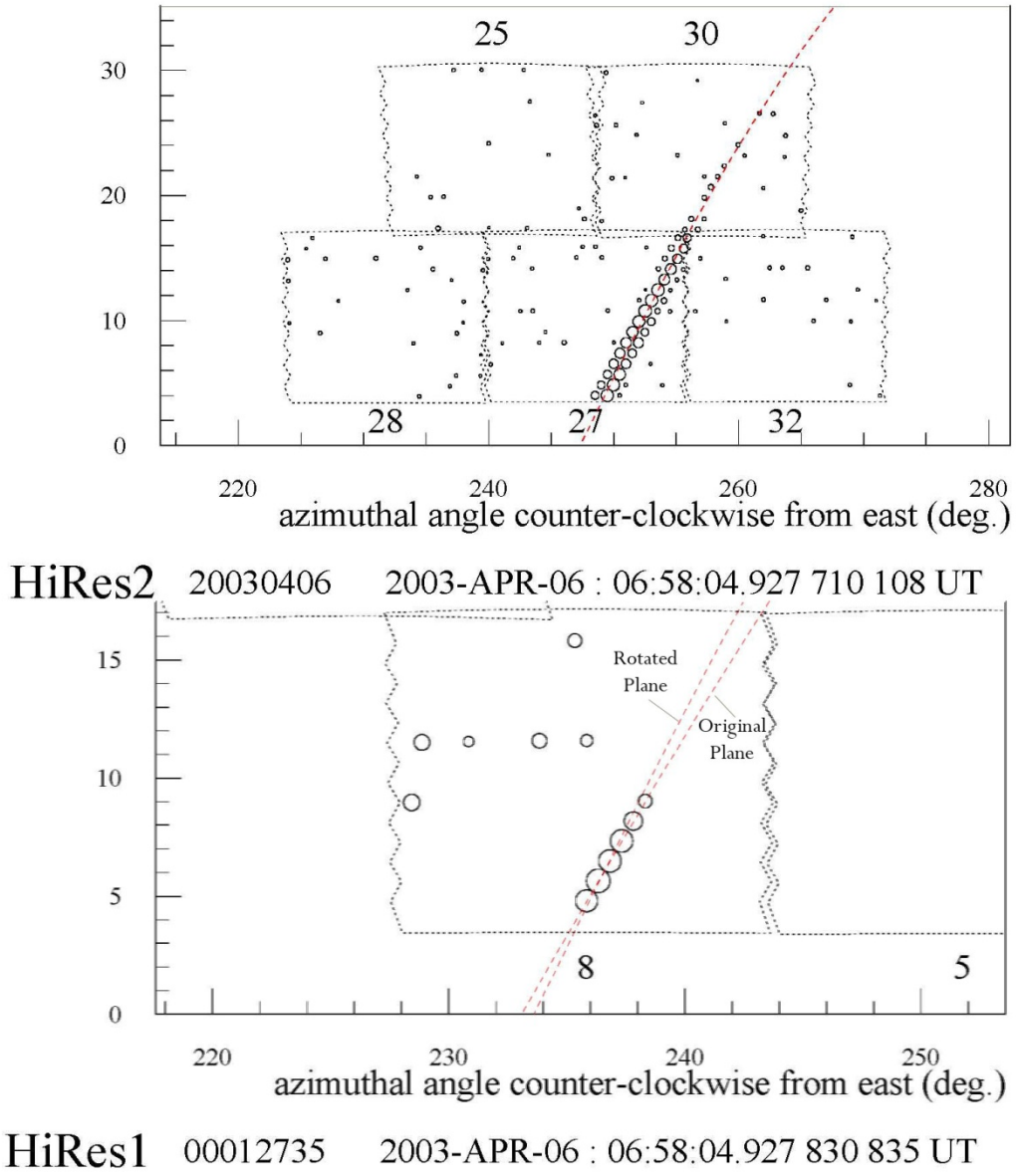

Figure 78: Event Display for event removed by plane rotation. See Table 13.

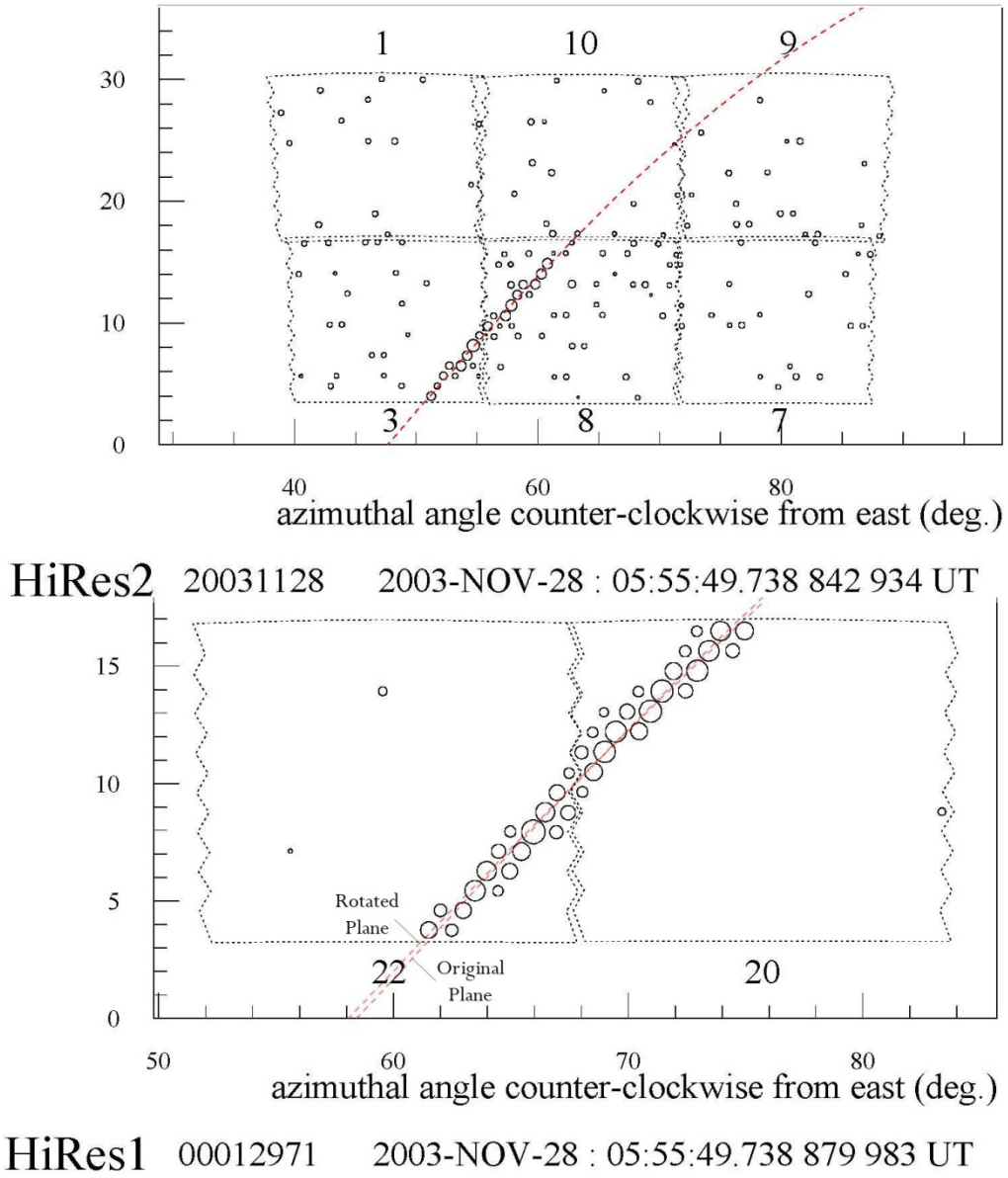

Figure 79: Event Display for event removed by plane rotation. See Table 13.

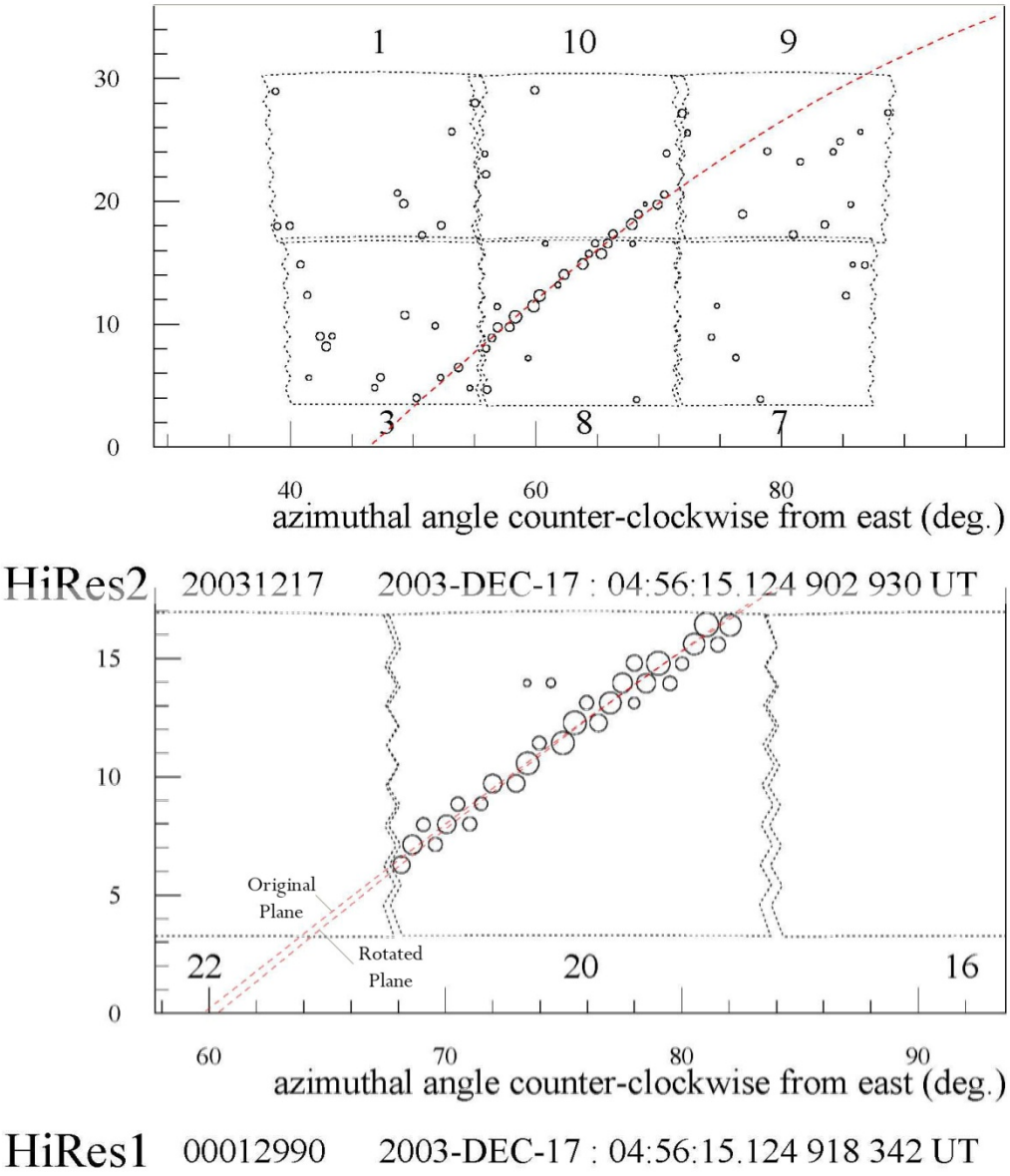

Figure 80: Event Display for event removed by plane rotation. See Table 13.

REFERENCES

[1] C. D. Anderson, Physical Review 43, 491 (1933).

[2] S. H. Neddermeyer, and C. D. Anderson, Physical Review 51, 884 (1937).

[3] V. V. Ezhela *et al.*, *Particle Physics: One Hundred Years of Discoveries* (AIP Press, Woodbury, New York, USA, 1996).

[4] P. Auger *et al.*, Reviews of Modern Physics, 288 (1939).

[5] V. A. K. G.T. Zatsepin, SJETP 4 (1966).

[6] K. Greisen, Physical Review Letters 16, 748 (1966).

[7] D. J. Bird *et al.*, Physical Review Letters 71, 3401 (1993).

[8] T. K. G. J. Cronin, and S.P. Swordy, Sci. American v276, p44 (1997).

[9] M. S. Longair, *High Energy Astrophysics* (Cambridge University Press, Cambridge, 1994), Vol. 2.

[10] A. R. Bell, Royal Astronomical Society, Monthly Notices 182, 147 (1978).

[11] R. U. Abbasi *et al.*, Physical Review Letters 100, 101101 (2008).

[12] R. U. Abbasi *et al.*, The Astrophysical Journal 622, 910 (2005).

[13] J. Han, Journal of Physics: Conference Series 47, 120 (2006).

[14] W. Deng, (Dept. of Physics, University of Utah, 2007., 2007), pp. xiii.

[15] K. Kim, (Dept. of Physics, University of Utah, 2002., 2002), pp. xii.

[16] C. M. G. L. *e. a.* Brazil-Japan Collaboration, in 13th International Cosmic Ray ConferenceUniversity of Denver, Co, 1973), p. 2227.

[17] J. a. B. E. C. Groups, in 13th Internationaf Cosmic Rays ConferenceDenver, 1973), p. 2219.

[18] V. Kopenkin, and Y. Fujimoto, Physical Review D (Particles, Fields, Gravitation, and Cosmology) 73, 082001 (2006).

[19] V. Kopenkin, Y. Fujimoto, and T. Sinzi, PhRvD 68, 052007 (2003).

[20] A. Ohsawa, E. H. Shibuya, and M. Tamada, PhRvD 70, 074028 (2004).

[21] E. Witten, Physical Review D (Particles and Fields) 30, 272 (1984).

[22] E. Farhi, and R. L. Jaffe, PhRvD 30, 2379 (1984).

[23] J. Madsen, Physical Review Letters 92, 119002 (2004).

[24] J. M. L. Jes Madsen, Physics Review Letters 90 (2003).

[25] E. Finch, Journal of Physics G: Nuclear and Particle Physics 32, S251 (2006).

[26] J. Madsen, Physical Review D (Particles and Fields) 71, 014026 (2005).

[27] F. Wu, R.-X. Xu, and B.-Q. Ma, Journal of Physics G: Nuclear and Particle Physics 34, 597 (2007).

[28] T. Z. AbuZayyad, in *Department of Physics* (Utah, Salt Lake City, 2000), p. 134.

[29] A. M. H. T. Gaisser, in 15th ICRCPlovidiv, Bulgaria, 1977), p. 353.

[30] C. L. Pryke, APh 14, 319 (2001).

[31] K. Riel, in *physics* (University of Utah, Salt Lake City, 2002), p. 194.

[32] F. Kakimoto *et al.*, Nuclear Instruments and Methods in Physics Research Section A: Accelerators, Spectrometers, Detectors and Associated Equipment 372, 527 (1996).

[33] W. F. Hanlon, in *physics* (University of Utah, Salt Lake City, 2008), p. 333.

[34] Y. Fedorova, in *Collaboration Meeting*University of Utah, 2005).

[35] I. Wolfram Research, *Mathematica* (Wolfram Research, Inc., Chapaign, Illinois.

[36] S. Brandt, *Data Analysis: Statistical and Computational Methods for Scientists and Engieneers* (Springer-Verlag, New York, 1999).

[37] G. B. W. Arfken, Hans J., *Mathematical Methods for Physicists* (Academic Press, San Diego, 2001), p. 1112.

[38] W. M. a. S. Newman, R.F., *Principles of Interactive Computer Graphics* (McGraw-Hill, New York, 1979).

[39] R. F. Riesenfeld, IEEE Comput. Graph. Appl. 1, 50 (1981).